ON THE USE OF IMPACT-INDUCED NONLINEARITIES IN LIMIT SWITCH DESIGN

BY

BRYAN RANDALL WILCOX

DISSERTATION

Submitted in partial fulfillment of the requirements
for the degree of Doctor of Philosophy in Mechanical Engineering
in the Graduate College of the
University of Illinois at Urbana-Champaign, 2011

Urbana, Illinois

Doctoral Committee:

Associate Professor Harry Dankowicz, Chair
Professor Lawrence A. Bergman
Professor Alexander F. Vakakis
Professor Andreas A. Polycarpou
Professor Arif Masud

Abstract

This dissertation explores the use of grazing bifurcations in impacting mechanical systems as a useful means of creating fast-acting limit switches. Using analytical, numerical, and experimental techniques, the transient and asymptotic responses of several example vibro-impacting systems undergoing the onset of low-relative-velocity contact are investigated. It is argued that the rapid transients and distinct asymptotic dynamics distinguishing pre- and post-grazing attractors provides an advantageous mechanism on which to base a limit switch design. Further, it is shown that these changes, which originate due to the mechanical interactions, can be detected in coupled electrical systems through both electromagnetic and electrostatic coupling mechanisms. The dissertation concludes with a realization in a prototype microelectromechanical systems (MEMS) design in which a grazing bifurcation may trigger snap-through in a parallel plate capacitive actuator. The results of these studies indicate that a switch based on the proposed nonsmooth fold scenario would outperform one that relies on a smooth bifurcation, such as the cyclic-fold bifurcation, in terms of switching speed and sensitivity.

To my wife and family for their steadfast love and support

Acknowledgments

As I reflect on the incredible experiences that made up the non-technical aspects of my Ph.D., my most fond recollections revolve around those who have helped to make this such a successful and rewarding endeavor. I would like to take this space to thank those who have contributed to making the last four years the best so far.

I would first like to express my gratitude to my advisor, Harry Dankowicz, for his patient guidance and support. Through our collaborations, I have grown tremendously in my abilities to model and solve difficult technical problems. I would also like to acknowledge his support for international travel. The experiences I had while abroad have given me perspectives and friendships that I will carry with me the rest of my life. v Many thanks to Bruce Flachsbart for the numerous hours we spent together discussing various topics and for all of his advice on microfabrication. I would also like to acknowledge Mike Hanson and Glennys Mensing for their help in making my MEMS work a success. Thanks also to Andreas Polycarpou for use of his laser sensor for the MEMS experiments. I also want to recognize Keith Parrish, Kyle Cheek, and Pete Hetman from the MechSE machine shop for advice on design and fabrication of test equipment.

Special thanks to Larry Bergman for the many hours of conversation. Story-telling is a fine art and Larry is one of the best. I would also like to recognize Larry Bergman and Alex Vakakis for the use of their laboratory space and equipment on the larger scale experiments. Thanks to Steve Platt for the conversations we shared about electronics, education, and the bigger picture. Steve also contributed the use of his equipment and helped with troubleshooting the communications interface.

Thanks to Walter Lacarbonara for graciously hosting my visit to Rome in the fall of 2008 and to Annika Stensson, Jenny Jerrelind, and Fredrik Svahn at KTH in Stockholm for help on the experiments performed there in 2007. I also want to extend my appreciation to Wonmo Kang and Phani Thota for our collaborations. Thanks also to Michael McFarland for the long discussions on Linux, computing, and fine writing instruments and materials.

Many thanks to Fredrik Svahn for his friendship and collaboration. We had some great adventures in Stockholm, Vienna, Mahomet, and Rome and I am still looking forward to that sailing trip in the archipelago.

Most importantly, I want to thank my wife and family, on both sides of the Atlantic. My gratitude to Mercedes for putting up with the long hours and stressful days cannot be put into words. I want to thank my parents, Randy and Jan, for always pushing me to follow my heart and dreams and instilling in me a belief that anything is possible with sufficient thought and effort. And thanks to my sisters, Angie and Katie, for reflecting our parent's values and pushing me to work and achieve, despite some of the frustrations along the way. Thanks to Grandpa Wilcox for his support, the summers on the farm, and teaching me to always plan ahead. On the other side of the family, I want to thank Grandma and Grandpa Sharkey for always being there and for teaching me to observe and recognize the incredible things which surround us. I am grateful for my parents-in-law, Mirjana and Rustem, who I want to thank for their love, support, and hospitality on many enjoyable visits. I also want to express appreciation to George and Jill for adopting me as family.

Finally, I would like to recognize the National Science Foundation which supported this work under Grant nos. 0237370, 0635469, and 0855787. I also want to recognize the financial support of the Swedish Science Council under Grant Nos. 2003-3699 and 2004-6342 for the experimental work done at KTH in Stockholm.

Table of Contents

List of Tables

List of Figures

Chapter 1

Introduction

1.1 Application and framework of prior art

The work contained in this dissertation is part of an effort to develop a novel class of ultrafast limit switch sensors. The performance benefit over existing designs is derived from fundamental insights into the behavior of the underlying nonlinear systems which describe the dynamics of these sensors. Emphasis is focused on sudden and possibly dramatic changes in system transient and steady-state response following the onset of low-relative-velocity, grazing mechanical contact. Specifically, the effort explores the practical use of such changes as signatures of the change of a system parameter across a predetermined threshold value in limit-switch design.

Limit switches constitute a class of input-output devices that change operating state in reaction to the crossing of a threshold value of their input [56]. They can be used as indicators, control devices, or commonly both, and provide signal transduction from the energy domain being sensed to the energy domain of observation. As indicators, limit switches provide logic outputs (true or false) depending on the level of their input [9]. These are used to monitor critical values of physical quantities, such as temperature, voltage, and pressure, in both consumer and industrial settings [11, 26, 27, 40]. As control devices, limit switches provide the simplest form of feedback: discrete on/off states in response to input. The switch might be permanent, such as when a fuse burns out, or capable of being reset, such as with a circuit breaker. Resettable limit switches often include hysteresis to prevent hunting near the threshold. Their use enables the safe, reliable operation of many everyday household items, such as coffee makers, electric circuit breakers, and water heaters.

Of particular interest in the present context are limit switches whose function relies on a snap-like action [9, 46]. Limit-switch sensors based on this phenomenology are examples of so-called bifurcation amplifiers [70, 71]. Here, the internal state of the switch transitions abruptly between two dissimilar steady-state behaviors as a result of a small change in the value of a system parameter [49]. Specifically, as the parameter exceeds the critical value, there is an associated loss of stability or disappearance of the original steady-state

behavior. This leaves the switch no choice but to evolve to a different steady-state attractor. Examples of such bifurcations include fold and subcritical pitchfork bifurcations of equilibria and are exploited in previously documented limit-switch devices (e.g., [27, 79]).

In many of these cases, parameter hysteresis results from the persistence of the target steady-state behavior even as the system parameter is reduced below the original threshold value. The speed of the transients following the bifurcation and the nature of the input dynamics determine the reaction of the switch to excursions past the threshold. As an example, a slow-blow fuse is designed to pass overload currents for a short amount of time to allow for start-up transients in electrical machinery. A lag in switching speed is thus critical to the successful operation of the slow-blow. In contrast, in the case of protection for a circuit board containing delicate components, a similar lag in switching speed would be disastrous.

In a larger context, this work is part of a nascent effort in nonlinear dynamics that will transform the field from a tool for modeling and analysis of observed behavior to a tool of intentional synthesis of engineered systems (e.g., [67]). In the past, the field of nonlinear dynamics has primarily focused on documenting and predicting phenomena in existing systems and devices. There is now a growing interest from the applied technology community to seek ways of exploiting system nonlinearities for improved performance rather than to constrain operation to parameter regions in which such phenomenology can be avoided. Examples of other such efforts are micro-oscillator mass sensors [79] designed to exhibit hardening parametric resonance curves and to trigger near smooth fold bifurcations; broadband, dissipative mechanisms [33] realized experimentally in macroscopic devices through the purposeful introduction of so-called essential nonlinearities; switching controllers [3] that rely on corner-collision bifurcations in piecewise-smooth systems for nonlinear stabilization of limit cycles in smooth systems; and radio-frequency microresonators [41] that rely on high-velocity impacts for a sustained broadband response.

1.2 Modeling contact

As suggested above, the sudden and possibly dramatic changes in system transient and steady-state response following the onset of low-relative-velocity, grazing mechanical contact is a possible operating principle for a novel class of limit switches. By definition, a grazing occurs when a periodic solution trajectory of a dynamical system tangentially intersects a discontinuity surface in the state space of the system. Systems with discontinuities in the time evolution of the state vector or vector field are typicall modeled as having continuous-in-time dynamics interrupted by discrete-in-time events. These models are formally known as hybrid dynamical systems, and in the context of mechanical systems, such models are commonly used, for

example, in the description of gear trains, oilwell drill strings, and impact actuators [15, 29, 31, 39, 83].

The continuous-in-time dynamics, or smooth time evolution, of hybrid systems is typically described by ordinary differential equations whose variables represent the system state. These equations are usually cast as collections of first-order differential equations, which lend themselves to many readily available numerical integration schemes. For mechanical systems described using lumped-parameter approximations, these ordinary differential equations follow directly from the physical modeling. For physical systems described using partial differential equations, a weak form must first be obtained using some discretization scheme before the dynamics can be represented approximately as a system of ordinary differential equations.

The discrete-in-time events which interrupt the smooth dynamics of the system are coarsened models of dynamical features whose timescales are much shorter than the characteristic timescale of the overall dynamics. In electrical systems, the change in position of a switch might be modeled as a discrete-in-time event, i.e. the time required for the switch to change state is very small compared to dominant natural periods or time constants present in the system.

In later chapters, the onset of contact in a mechanical system is considered as a discrete-in-time event. A typical scenario involves the evolution of the position of two bodies in relative motion such that contact occurs between the two at some time. At the onset of contact, the system is modeled as changing discretely in time to account for the interaction between the bodies. Depending on how the contact is modeled, the discrete change might be described as a change in state or as a change in the governing vector field.

In the case of non-compliant contact models, the contact is assumed to be instantaneous and the entirety of the interaction between the contacting bodies is captured by a discrete change in the state of the system. A simple and popular example of this type of model is the kinematic coefficient of restitution impact law. This model describes the post-impact relative velocities of the system as proportional to the pre-impact relative velocities. The proportionality constant may vary between 0 and 1, where 0 indicates a complete loss of kinetic energy in the system (a perfectly plastic impact), and 1 represents perfect conservation of kinetic energy (a perfectly elastic impact).

Contact mechanics and finite element methods exist which can be used to calculate estimates for the coefficient of restitution based on problem-specific parameters. These methods demonstrate dependence on material properties, impact velocities, and geometry at the contact interface. A recent paper by Katta et al [32] also discusses additional considerations when dealing with oblique collisions. For a fascinating and more complete discussion of contact models, the book by Stronge [62], also provides a good reference.

The kinematic coefficient of restitution is used in this dissertation to describe the interaction between rigid bodies undergoing collinear contact. In this work, the values for the coefficient of restitution used in

numerics are obtained directly from its empirical definition using experimental data for pre- and post-impact relative velocities. As shown in Chapters 4 and 5, the agreement between numerical and experimental results shows that this contact law provides a reasonable approximation for the parameter regions considered here.

Compliant contact models are used to describe contact in systems where the duration of contact is relatively long, or where the mechanical system requires a continuum description. Some popular compliant contact models include a simple conservative spring as well as the Kelvin-Voight and Maxwell element models [62].

A Kelvin-Voight element consists of a linear spring and damper placed in parallel. This model allows for complete restitution of the contact element, but for non-zero initial relative velocities between the contacting bodies, it generates a non-zero, finite force at the onset of contact. For systems being modeled as continua, this discontinuous forcing function could be argued as violating the basic continuum modeling assumption. The Maxwell element, which consists of a linear spring and damper in series, overcomes the discontinuous forcing issue present in the Kelvin-Voight model, but does not allow for full restitution of the element.

The conservative spring model makes up for the shortcomings of both the Kelvin-Voight and the Maxwell elements, but provides no mechanism for additional dissipation of energy during the contact phase. This spring element is used in Chapter 3 of this dissertation to describe the interaction between a continuous beam and an obstacle. The purpose of that study is to explore the effects of contact stiffness on the number of mechanical modes required to capture the changes in system behavior due to the onset of contact.

1.3 Content of remaining chapters

To evaluate the potential of the grazing bifurcation for use in ultrafast limit switches, an integrated approach is adopted which makes use of theoretical, numerical, and experimental techniques. This approach is applied to a set of mechanical and electromechanical systems to explore the behavior of the grazing bifurcation and draw conclusions about its viability for use as a limit switch operational phenomenology. These results are then combined with observations of the dependence on length scale of governing parameter to argue for miniaturization of such systems for further performance improvements.

Through the use of examples, the first two chapters discuss techniques used to analyze hybrid dynamical systems. In particular, Chapter 2 presents a study of a microimpact actuator built by Mita et al [48]. This example demonstrates a formalism for dealing with hybrid system trajectories and presents a bifurcation analysis utilizing the computational toolbox TC-HAT ($\widehat{\text{TC}}$). Significant portions of this chapter are taken from the paper *Bifurcation analysis of a microactuator using a new toolbox for continuation of hybrid system*

trajectories by Kang, Thota, Wilcox, and Dankowicz [30]. Dr. Phanikrishna Thota wrote the computational toolbox with guidance from Prof. Harry Dankowicz. Bryan Wilcox collaborated with Wonmo Kang in performing the numerics. The paper was written jointly.

Chapter 3 goes on to study a microscale Euler-Bernoulli beam which may contact a flexible barrier at a point along its span. The partial differential equation which describes its behavior is discretized and a series of reduced order models are examined. Some observations on the modeling of contact are included. These elucidate the choice of contact law and inform discussion in later chapters. The content of this chapter was published in the 2009 ASME International Design Engineering and Technical Conference paper *Response of Electrostatically Actuated Flexible MEMS Structures to the Onset of Low-velocity Contact* by Wilcox, Dankowicz, and Lacarbonara [75]. Bryan Wilcox performed the analysis and numerics with guidance from Prof. Dankowicz and Prof. Lacarbonara. Bryan Wilcox presented the paper at the conference. The paper was written jointly.

In Chapter 4, a simple example of a grazing bifurcation is considered, where increases in the amplitude of a periodically oscillating shaker head result in the onset of low-relative-velocity contact between the head and a suspended mass. When the contact is modeled using a kinematic coefficient of restitution impact law, the discontinuity mapping technique pioneered by Nordmark predicts a square-root growth term in the map describing the local evolution of the solution trajectory [52]. Under certain, computable conditions, this results in a rapid, discontinuous transition to a post-grazing behavior that is very distinct from the pre-grazing response. This theoretical result is demonstrated, then subsequently confirmed both numerically and experimentally. The content of this chapter was published in the paper titled *Transient growth rates of near-grazing impact velocities: Theory and experiments* by Wilcox, Svahn, Dankowicz, and Jerrelind [76]. Fredrik Svahn and Bryan Wilcox planned and performed the experiments jointly with feedback and guidance from Prof. Harry Dankowicz and Prof. Jenny Jerrelind. Fredrik Svahn and Harry Dankowicz performed the theoretical analysis. Bryan Wilcox wrote and ran the numerical routines which simulated the system and processed the experimental data. The paper was written jointly.

A coupled electromechanical system is considered in Chapter 5 to explore the possibility of detecting the grazing bifurcation by observing only the coupled electrical signal [73, 74]. In this system, a ferromagnetic mass is suspended relative to an electromagnet, which is excited by a periodic voltage input. The system is interrogated via current, velocity, and position sensors to collect data about the evolution of the state of the system. Through a series of experimental and numerical studies, it is shown that jumps to post-grazing attractors which have distinct amplitude and frequency content from the pre-grazing trajectories can indeed be detected by observing only the coupled electrical signal, which in this case is the current in the electrical

circuit. This work will appear as an invited paper titled *An experimental testbed for investigating nonsmooth bifurcations in an electromechanical system* by Wilcox and Dankowicz, published as part of a special issue on Experiments in Dynamics and Control in the Journal of Vibration and Control [74]. Bryan Wilcox was solely responsible for this work, which was overseen by Prof. Harry Dankowicz. The paper was written jointly.

Considering these behaviors in the context of limit switches, the rapid transitions between distinct pre- and post-grazing states could be very advantageous for an application requiring extremely fast switching response. However, we must now distinguish between absolute and relative speed. It is shown in Chapter 4 that the rapid transients of a system undergoing a grazing bifurcation are of the same order as the period of oscillation of the pre-grazing trajectory. If the period of oscillation is very long, it follows that the absolute transition time would be quite long. However, if the period of oscillation can be made very short, the absolute response time of a sensor based on this mechanism would be very fast.

Due to scaling characteristics relating mass and stiffness in mechanical systems, as devices are made smaller their natural frequencies increase. This suggests that to make an ultrafast limit switch based on a mechanical system undergoing a grazing bifurcation, one should make the physical size of the mechanism as small as possible. This miniaturization provides other benefits as well having to do with power consumption, packaging, and space requirements, among others. This reasoning leads to the material in Chapter 6, which presents a microelectromechanical systems (MEMS) implementation of a grazing-bifurcation-enabled limit switch. This limit switch is a MEMS-based version of a crowbar, circuit-protection device which might be used to short-circuit dangerous currents around the components being protected [28, 73]. The portions of this chapter pertaining to modeling work were presented at the 2009 ASME International Design Engineering and Technical Conference in a paper titled *Design of Limit-Switch Sensors Based on Discontinuity-Induced Nonlinearities* by Wilcox and Dankowicz [72]. This paper received first prize in the IDETC-VIB student paper contest and has appeared as a full journal article titled *Limit-switch sensor functionality based on discontinuity-induced nonlinearities* in the Journal of Computational and Nonlinear Dynamics. Bryan Wilcox was solely responsible for the work with oversight and feedback given by Prof. Harry Dankowicz. The paper was written jointly. Dr. Bruce Flachsbart provided feedback and suggestions on processing, fabrication, and design of the MEMS device.

Chapter 2

Numerical Analysis of an Example MEMS Impact Actuator

2.1 Introduction

Hybrid dynamical systems, which are characterized as having continuous-in-time dynamics interrupted by discrete-in-time events, serve as mathematical models of many real-world phenomena, for example, in the description of gear trains, oilwell drill strings, and impact actuators [13, 15, 29, 31, 39, 83]. Since the work presented in this dissertation is concerns the behavior of oscillatory mechanical systems near the onset of low-velocity contact, hybrid systems theory is a suitable framework.

The complexity of hybrid dynamical systems necessitates the use of numerical techniques for quantitative insight into system dynamics. As in the study of smooth dynamical systems, methods based on forward time integration are time consuming and primarily restricted to the study of transient dynamics and steady-state attractors. They fail to provide information about unstable recurrent behaviors or bifurcation sequences involving such unstable recurrent motions. Techniques that rely on a combination of iterative solvers for nonlinear algebraic equations and numerical shooting provide a useful alternative, at least in the study of periodic solutions. Indeed, such methods easily handle unstable motions as well as characteristic bifurcations involving periodic solutions.

The software application TC-HAT ($\widehat{\text{TC}}$), developed by Dr. Phanikrishna Thota and Prof. Dankowicz, is a general purpose toolbox for the study and continuation of periodic trajectories of hybrid dynamical systems and their bifurcations. It leverages the advantages of the Boundary-Value-Problem approach implemented in AUTO 97 [17] for pseudo-arclength-based continuation of periodic trajectories (AUTO 97 is a popular program used to perform bifurcation analysis of smooth dynamical systems and is capable of performing parameter continuation of periodic trajectories and their associated bifurcations). In particular, it implements this boundary-value-problem formulation for one-parameter continuation of periodic trajectories including multiple distinct solution segments and two-parameter continuation of saddle-node, period-doubling, and grazing bifurcation points corresponding to such trajectories. Further detail on the formulation of the corresponding boundary-value problems and their implementation in $\widehat{\text{TC}}$ may be found in [63].

The numerical bifurcation analysis of an impact microactuator presented here extends similar analyses reported in the literature (cf. Zhao *et al.* [82, 83, 81] and Dankowicz *et al.* [15]), and performed using problem-specific continuation algorithms, to previously unexplored regions of parameter space. This enables a more comprehensive analysis of the actuator dynamics that might aid in the design of an optimized operating regime for the actuator in a particular application. The analysis also reveals suggestive patterns of self-similarity in its dynamic behavior across the parameter space, particularly in the organization of bifurcation curves for trajectories with different number of segments.

The next section of this chapter discusses the mathematical modeling of hybrid dynamical systems, introduces a formalism for handling the different segments making up hybrid trajectories, and describes how these features are translated into $\widehat{\text{TC}}$. Section 2.3 introduces the sample microactuator and the mathematical model which describes its behavior. A bifurcation analysis is performed which illustrates the use of $\widehat{\text{TC}}$ to explore the behavior in the parameter space of the microactuator. The chapter concludes in Sec. 2.4 with a discussion of some interesting features present in the bifurcation diagrams and suggests the possible use of these features in application.

2.2 Mathematical Preliminaries

2.2.1 Hybrid Dynamical Systems

Here, a *hybrid dynamical system* assumes the existence of an n-dimensional state space $\mathbb{X}$ and an associated vector-valued function $\mathbf{f}_{\mathbf{I}} : \mathbb{X} \to \mathbb{X}$ known as the *vector field*, parameterized by an *index vector* $\mathbf{I}$ in some set $\mathbb{F}$. To each value of the index vector $\mathbf{I}$ associate a smooth *event function* $h_{\mathbf{I}} : \mathbb{X} \to \mathbb{R}$ and a smooth *state jump function* $\mathbf{g}_{\mathbf{I}} : \mathbb{X} \to \mathbb{X}$. Then, a *solution trajectory* to the hybrid dynamical system is a sequence $\{\mathbf{x}_j : [t_{j-1}, t_j] \to \mathbb{X}\}_{j=1}^{m}$ of m smooth curve segments and an associated sequence of index vectors $\{\mathbf{I}_j\}_{j=1}^{m}$, such that

$$\mathbf{I}(t) = \mathbf{I}_j, t \in (t_{j-1}, t_j] \tag{2.1}$$

and

1. The corresponding tangent vector at $\mathbf{x}_j(t)$ equals $\mathbf{f}_{\mathbf{I}_j}(\mathbf{x}_j(t))$, i.e., in the case of $\mathbb{X} = \mathbb{R}^n$

$$\frac{d}{dt}\mathbf{x}_j(t) = \mathbf{f}_{\mathbf{I}_j}(\mathbf{x}_j(t)) \tag{2.2}$$

2. The j-th segment terminates at an intersection with the *event surface*

$$\left\{\mathbf{x} \mid h_{\mathbf{I}_j}(\mathbf{x}) = 0, h_{\mathbf{I}_j,\mathbf{x}}(\mathbf{x}) \cdot \mathbf{f}_{\mathbf{I}_j}(\mathbf{x}) \leq 0\right\} \tag{2.3}$$

such that

$$h_{\mathbf{I}_j}(\mathbf{x}_j(t_j)) = 0 \tag{2.4}$$

3. The *connectivity* between the j-th and $j+1$-th segments is given by the function $\mathbf{g}_{\mathbf{I}_j}$, i.e.,

$$\mathbf{g}_{\mathbf{I}_j}(\mathbf{x}_j(t_j)) = \mathbf{x}_{j+1}(t_j) \tag{2.5}$$

The sequence $\Sigma = \{\mathbf{I}_j\}_{j=1}^{m}$ of values of the index vector is called the solution's *signature* (cf. [44]). Here, we allow for the possibility of infinite solution sequences and the replacement of m by ∞.

A *periodic solution* of a hybrid dynamical system is a solution with a periodic signature of base length m, such that

$$\mathbf{x}_1(t_0) = \mathbf{g}_{\mathbf{I}_m}(\mathbf{x}_m(t_m)) \tag{2.6}$$

The *period* of the solution then equals

$$T = \sum_{j=1}^{m}(t_j - t_{j-1}) = t_m - t_0 \tag{2.7}$$

The terminal point $\mathbf{x}_j(t_j)$ on the j-th solution segment is a *transversal event* if

$$h_{\mathbf{I}_j,\mathbf{x}}(\mathbf{x}_j(t_j)) \cdot \mathbf{f}_{\mathbf{I}_j}(\mathbf{x}_j(t_j)) < 0 \tag{2.8}$$

and a *grazing event* otherwise. Grazing events may also occur at non-terminal points along a solution segment. In this case, there exists a time $t \in (t_{j-1}, t_j]$, such that

$$h_{\mathbf{J},\mathbf{x}}(\mathbf{x}_j(t)) \cdot \mathbf{f}_{\mathbf{I}_j}(\mathbf{x}_j(t)) = 0 \tag{2.9}$$

for some index vector $\mathbf{J}$. The occurrence of grazing events is characteristic of *grazing bifurcations* in hybrid dynamical systems.

2.2.2 TC-HAT ($\widehat{\text{TC}}$)

The study of dynamical systems with discontinuities is mostly confined to numerical investigations involving direct numerical integration of the corresponding differential equations, or the maps that model them. This approach is used extensively in later chapters to investigate transient behaviors. Such numerical schemes, based on the time evolution or forward iterates of a system, can only locate stable orbits and fail to give any information about the unstable orbits or associated bifurcations. There is thus a need for novel continuation methods, similar to those used in the bifurcation analysis of smooth dynamical systems, to enable a rigorous study of the bifurcations in hybrid dynamical systems.

TC-HAT ($\widehat{\text{TC}}$)–Toolbox for Continuation of Hybrid Trajectories–is a Fortran-based software application that partially automates bifurcation analysis of periodic solution trajectories in the general class of hybrid dynamical systems described above, e.g., vibro-impact oscillators with or without friction. $\widehat{\text{TC}}$ functions as a *driver* to a modified version of AUTO 97 [17], a Fortran-based software application for the bifurcation analysis of smooth dynamical systems. In particular, $\widehat{\text{TC}}$ exploits AUTO 97's Boundary-Value-Problem formulation to locate and continue periodic trajectories of hybrid dynamical systems and a subset of associated co-dimension-one bifurcation points under variations in system parameters. In particular, $\widehat{\text{TC}}$ can detect co-dimension-one bifurcations associated with the crossing of one or several eigenvalues across the unit circle, including saddle-node, period-doubling bifurcations, and Neimark-Sacker bifurcations.

The modifications to AUTO 97 further enable $\widehat{\text{TC}}$ to continue, in two free parameters, saddle-node and period-doubling bifurcation curves through the simultaneous solution of the associated first variational equations for an eigenvector of the monodromy matrix corresponding to an eigenvalue equal to 1 and -1, respectively. In addition, continuation in two free parameters is also possible of solution trajectories that achieve grazing contact or that cross an intersection of two event surfaces at the terminal point of the first solution segment. For further detail regarding the boundary-value formulations associated with these two-parameter continuation problems, see [63] and [65].

The discussion below highlights those features of the use of $\widehat{\text{TC}}$ that distinguish it from AUTO 97. Specifically, in order to perform bifurcation analysis using $\widehat{\text{TC}}$, three text files are provided to the program. The $\widehat{\text{TC}}$ *function* file contains the system vector fields, the system event functions, and the system state jump functions and the connectivity information that associates values of the index vector with combinations of vector field, event function, and state jump function. As with AUTO 97, the $\widehat{\text{TC}}$ *constants* file contains numerical values for a variety of parameters governing the continuation algorithm, such as initial, maximum, and minimum values for the pseudo-arclength continuation parameter. More importantly, the constants file includes the desired signature of the periodic trajectory to be continued as well as information about

additional event surfaces with which grazing events should be detected during continuation. Finally, in the case of initializing continuation from a solution obtained by other means (e.g., forward-time simulation), a *data* file is provided that contains the values of the state vector sampled at discrete moments in time along the solution trajectory. Each time interval $[t_{j-1}, t_j]$ is discretized by a segment-independent partition of the interval $[0, 1]$ (contained in the first column of the data file) scaled to the length of the segment. The time history of the i-th state variable along the j-th segment is then contained in the $1 + n\,(j-1) + i$-th column, where n is the state-space dimension of the hybrid dynamical system.

As with AUTO 97, the initial solution for single-parameter continuation of a periodic trajectory may be obtained from a data file, as described above, or from a periodic trajectory obtained through a previous one- or two-parameter continuation run. Similarly, continuation of saddle-node or period-doubling bifurcations requires restarting the continuation from the output data obtained during a one-parameter continuation. In contrast, in the case of continuation of trajectories with grazing events, the initial data may be derived directly from the output data of a previous one-parameter continuation or by providing a data file containing a resegmented version of previously obtained output data ensuring that the grazing event terminates the first solution segment.

The methodology described here enables a wide exploration of parameter space initialized at the outset with a single initial solution guess. In particular, the continuation process is able to handle multisegment solution trajectories with relatively large values of m limited only by the memory needs of the AUTO implementation.

2.3 The Impact Microactuator

2.3.1 Mechanical Model

The actuating mechanism under consideration is adapted from a design originally published by Mita *et al.* [48]. The actuator consists of two inertial masses capable of relative motion, one suspended within the other as shown in Fig. 2.1. The outer mass, termed the *frame*, rests on or is held against a substrate. The second mass, termed the *impactor*, is suspended within the frame. Its motion relative to the frame is excited by a parallel-plate capacitive drive. Clearances between the frame and impactor are such that collisions between the two may occur with sufficient displacement of the impactor relative to the frame. The actuator is said to be in *stick* if the frame is stationary relative to the substrate and in *slip* otherwise. Specifically, the actuator is in *positive slip* when the motion of the frame would result in an increased capacitor gap in the case that the impactor was kept stationary, and in *negative slip* otherwise.

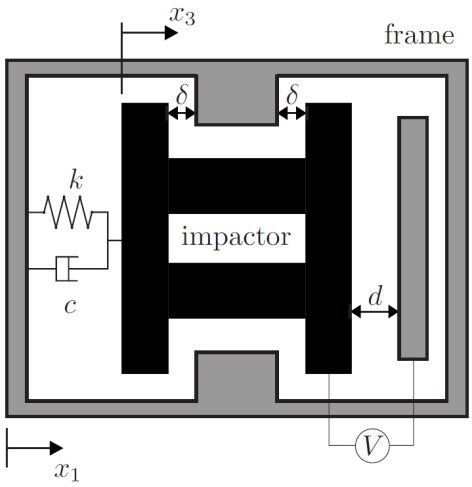

Figure 2.1: A schematic of the impact microactuator, in which the impactor is shown in its equilibrium position in the absence of excitation and the electrostatic excitation is represented by the voltage amplitude V. Figure modified from [82] and reproduced with permission from the publisher.

The effects of the contact between the frame and the substrate on the motion of the frame is assumed to be captured by dry friction and modeled by Amonton's law in stick and Coulomb friction in slip. In addition to the electrostatic excitation, interactions between the frame and impactor transmitted through the suspension are modeled with a combination of a linear elastic and a linear dissipative element. Finally, collisions between the frame and the impactor are modeled as instantaneous impacts that, through the imposition of conservation of momentum and Newton's law of restitution, result in discontinuous-in-time changes in the velocities of the frame and impactor.

Transitions from stick to slip are triggered by two distinct types of events. In the first case, the net force on the frame from its interactions with the impactor exceeds the maximum available frictional force between the frame and the substrate. Here, the velocity of the frame relative to the substrate is continuous across the transition from stick to slip. Additionally, slip may also result from a collision between the impactor and the frame resulting in a nonzero momentum of the frame relative to the substrate subsequent to the collision.

Transitions from slip to stick may also be triggered by two distinct types of events. In both cases, subsequent to the frame reaching zero velocity relative to the substrate, the friction force adjusts instantaneously to completely cancel the effects of the other forces applied to the frame. In the first case, the zero relative velocity between the frame and the substrate occurs as a result of the dissipative nature of the friction force. Here, again, the velocity of the frame relative to the substrate is continuous across the transition. In contrast, for non-generic pre-transition velocities, zero-relative velocity may also result from a collision between the impactor and the frame resulting in a zero momentum of the frame relative to the substrate

subsequent to the collision. In this case, the velocity is clearly a discontinuous function of time across the transition.

Repeated transitions from stick to slip and back again result in a stepwise motion of the microactuator along the substrate. By controlling the nature and timing of transitions between stick and slip a versatile, precise position actuator may be realized. Large gross displacements of the actuator can be attained through the composition of many small, stepwise displacements. These characteristics of high driving power, small precise displacements, and long driving distances make the impact microactuator an interesting candidate for a variety of technical applications [25].

2.3.2 Mathematical Model

Following [15, 66, 82, 83, 81], the dynamics of the impact microactuator may be formulated as a hybrid dynamical system in the following way. Denote the state vector by $\mathbf{x}$, where x_1 is the displacement of the frame of mass m_1 relative to the substrate, x_2 is the velocity of the frame relative to the substrate, x_3 is the displacement of the impactor of mass m_2 relative to the undeformed length of the linear spring, x_4 is the velocity of the impactor relative to the frame, and x_5 is the instantaneous phase of the excitation. In particular, the actuator is in positive slip when $x_2 > 0$, in stick when $x_2 = 0$, and in negative slip otherwise. Three distinct vector fields are required to describe the rate of change of the state vector with respect to time during stick, positive slip, and negative slip, respectively, namely

$$\mathbf{f}_{\text{stick}}(\mathbf{x}) = \begin{pmatrix} 0 \\ 0 \\ x_4 \\ \frac{F}{m_2} \\ \omega \end{pmatrix} \tag{2.10}$$

$$\mathbf{f}_{\text{slip}\pm}(\mathbf{x}) = \begin{pmatrix} x_2 \\ -\frac{F \pm \mu_d N}{m_1} \\ x_4 \\ \frac{F}{m_2} + \frac{F \pm \mu_d N}{m_1} \\ \omega \end{pmatrix} \tag{2.11}$$

where

$$F = \frac{\alpha V^2 \sin^2 x_5}{(d - x_3)^2} - c x_4 - k x_3 \tag{2.12}$$

α is related to the permittivity of free space, d is the zero-voltage gap between the electrodes (such that $d - x_3$ equals the capacitor gap), k is the spring constant, c is the damping coefficient, V is the amplitude of the sinusoidally varying voltage applied between the electrodes, μ_d is the coefficient of dynamic friction, N is the normal reaction experienced by the frame from the ground (here taken to equal $(m_1 + m_2)\, g$, where g is the acceleration of gravity), and ω is the frequency of excitation. Here, the upper sign corresponds to positive slip and the lower sign corresponds to negative slip in Eqn. (11).

Transitions between distinct phases of motion are governed by the six event functions

$$h_{\text{front}}(\mathbf{x}) = \delta - x_3 \tag{2.13}$$

$$h_{\text{back}}(\mathbf{x}) = \delta + x_3 \tag{2.14}$$

$$h_{\text{stick}\pm}(\mathbf{x}) = \pm F + \mu_s N \tag{2.15}$$

$$h_{\text{slip}\pm}(\mathbf{x}) = \pm x_2 \tag{2.16}$$

where μ_s is the coefficient of static friction, δ is the equilibrium clearance between the frame and the impactor; and the two state jump functions

$$\mathbf{g}_{\text{impact}}(\mathbf{x}) = \begin{pmatrix} x_1 \\ x_2 + m_2 \frac{(1+e)}{m_1+m_2} x_4 \\ x_3 \\ -e x_4 \\ x_5 \end{pmatrix} \tag{2.17}$$

$$\mathbf{g}_{\text{identity}}(\mathbf{x}) = \mathbf{x} \tag{2.18}$$

where e is the kinematic coefficient of restitution. For purposes of concise data collection, we consider the additional event function

$$h_{\text{Poincaré}}(\mathbf{x}) = x_4 \tag{2.19}$$

such that the corresponding event surface corresponds to points of local maxima in the extension of the spring.

Now let

$$\mathbb{Z}_f = \{\text{stick,slip+,slip-}\} \tag{2.20}$$

$$\mathbb{Z}_h = \left\{ \begin{array}{c} \text{front,back,stick+,stick-,} \\ \text{slip+,slip-,Poincaré} \end{array} \right\} \tag{2.21}$$

$$\mathbb{Z}_g = \{\text{impact,identity}\} \tag{2.22}$$

and suppose that $\mathbb{F}$ is the subset of $\mathbb{Z}_f \times \mathbb{Z}_h \times \mathbb{Z}_g$ corresponding to the connectivity graph in Fig. 2.2 showing the relationship between a given vector field, the event functions that are monitored during forward simulation with the corresponding vector field, and the state jump function associated with a given event function. For example, $\mathbf{I} = (\text{stick,front,impact})$ corresponds to a trajectory segment governed by the vector field $\mathbf{f}_{\text{stick}}$, terminating on the event surface corresponding to h_{front}, and connected to the next trajectory segment by the state jump function $\mathbf{g}_{\text{impact}}$. Each segment of a trajectory of the hybrid dynamical system describing the impact microactuator then corresponds to one of the following index vectors

$$\begin{aligned}
\mathbf{J}_1 &= (\text{stick,front,impact}) \\
\mathbf{J}_2 &= (\text{stick,back,impact}) \\
\mathbf{J}_3 &= (\text{stick,stick+,identity}) \\
\mathbf{J}_4 &= (\text{stick,stick-,identity}) \\
\mathbf{J}_5 &= (\text{stick,Poincaré,identity}) \\
\mathbf{J}_6 &= (\text{slip+,front,impact}) \\
\mathbf{J}_7 &= (\text{slip+,back,impact}) \\
\mathbf{J}_8 &= (\text{slip+,slip+,identity}) \\
\mathbf{J}_9 &= (\text{slip+,Poincaré,identity}) \\
\mathbf{J}_{10} &= (\text{slip-,front,impact}) \\
\mathbf{J}_{11} &= (\text{slip-,back,impact}) \\
\mathbf{J}_{12} &= (\text{slip-,slip-,identity}) \\
\mathbf{J}_{13} &= (\text{slip-,Poincaré,identity})
\end{aligned}$$

In particular, the (cyclic) signature of a periodic trajectory is given by the periodic repetition of a finite sequence $\left\{\mathbf{J}_{k_j}\right\}_{j=1}^{m}$ for some finite sequence $\{k_j\}_{j=1}^{m}$. As an example, a periodic trajectory with base signature

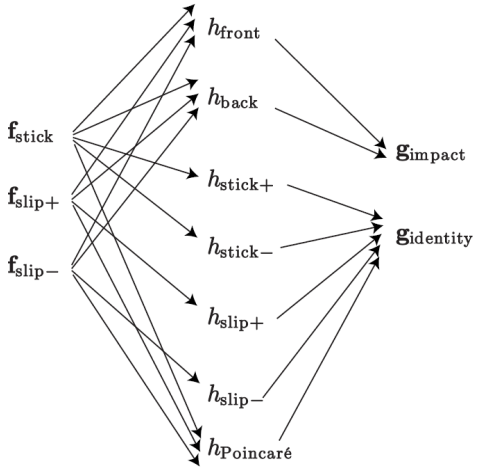

Figure 2.2: The connectivity graph corresponding to the impact microactuator. Each segment of a trajectory of the corresponding hybrid dynamical system is represented by one of the index vectors shown here.

$\{\mathbf{J}_1, \mathbf{J}_8\}$ corresponds to the boundary-value problem

$$\dot{\mathbf{x}}_1(t) = \mathbf{f}_{\text{stick}}(\mathbf{x}_1(t)), t \in [t_0, t_1] \tag{2.23}$$

$$\dot{\mathbf{x}}_2(t) = \mathbf{f}_{\text{slip}+}(\mathbf{x}_2(t)), t \in [t_1, t_2] \tag{2.24}$$

$$h_{\text{front}}(\mathbf{x}_1(t_1)) = 0 \tag{2.25}$$

$$h_{\text{slip}+}(\mathbf{x}_2(t_2)) = 0 \tag{2.26}$$

and

$$\mathbf{x}_2(t_1) = \mathbf{g}_{\text{impact}}(\mathbf{x}_1(t_1)) \tag{2.27}$$

$$\mathbf{x}_1(t_0) = \mathbf{g}_{\text{identity}}(\mathbf{x}_2(t_2)) \tag{2.28}$$

2.3.3 Numerical Results

The numerical bifurcation analysis reported in this section follows a general pattern. First, single-parameter continuation is performed of branches of periodic trajectories of a given signature. During such continuation, changes in linear stability characteristics associated with saddle-node and period-doubling bifurcations as well as the occurrence of grazing events are monitored and detected within the numerical accuracy of the implementation. Two-parameter continuation is then used to trace the corresponding period-doubling,

saddle-node, and grazing bifurcation curves. In particular, it is shown how the grazing bifurcation curve can be continued using alternative signatures and associated trivial changes in segment structure. These reflect the signature and character of the post-grazing family of periodic trajectories emanating from such grazing bifurcation points.

Table 2.1 shows the parameter values used in the numerical results reported here. Specifically, results are presented only for periodic orbits of period $T = \frac{\pi}{\omega}$ corresponding to the fundamental period of the vector fields. In the figures below, SN denotes saddle-node bifurcations, PD denotes period-doubling bifurcations, and G-n denotes grazing bifurcation points of periodic orbits with n impacts per period. Unless stated otherwise, solid and dashed curves represent branches of stable and unstable periodic solution trajectories, respectively.

Parameter	Value
m_1	5
m_2	1
k	1
c	0.04
d	1
δ	0.5
e	0.8
$\mu_{\rm s}$	0.4
$\mu_{\rm d}$	0.27
α	1
N	58.86

Table 2.1: Nondimensionalized parameter values used in the numerical computations presented in this paper. These were obtained from [15] with the additional assumption (consistent with numerical simulations in [15]) that $m_2/kd \approx 1$ m/s^2 in SI units.

A unique, small-amplitude periodic solution (modulo absolute translations of the frame relative to the substrate) with base unit signature $\{\mathbf{J}_5\}$ may be found for $\omega \approx 0.9189$ and $V \approx 0.01$. The result of a single-parameter continuation of the corresponding branch of periodic trajectories under variations in V is shown in the upper panel of Fig. 2.3. The lower panel of Fig. 2.3 shows the grazing periodic trajectory obtained for $V \approx 0.5876$, for which grazing contact is detected with the event surface corresponding to $h_{\rm front}$.

The period-doubling and grazing bifurcation curves through the bifurcation points marked PD and G-1 in the upper panel of Fig. 2.3 are shown in Fig. 2.4. It follows, for example, that the minimum driving voltage corresponding to a grazing periodic solution is attained at $\omega \approx 0.4878$, slightly below the linear resonance frequency due to the softening nonlinearity associated with the electrostatic interaction.

As a starting solution for the two-parameter continuation of the grazing bifurcation curve, it is possible to use the single-segment grazing periodic trajectory with signature $\{\mathbf{J}_5\}$ found in the above single-parameter

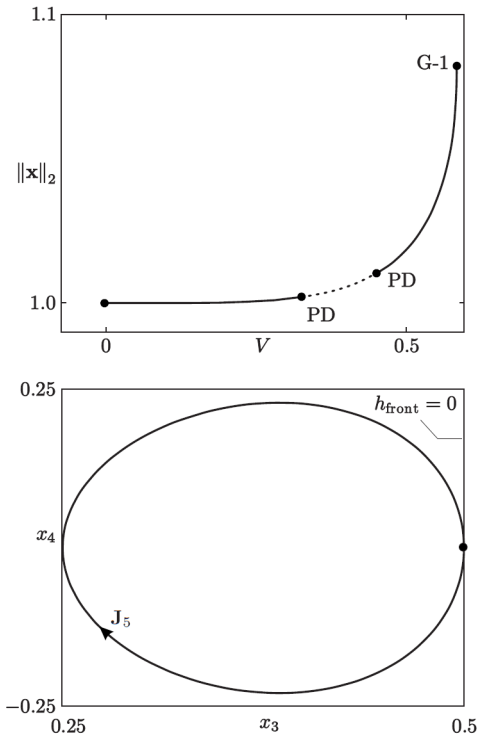

Figure 2.3: (upper panel) A branch of periodic solution trajectories with base unit signature $\{\mathbf{J}_5\}$ obtained from a one-parameter continuation with varying V for $\omega \approx 0.9189$. (lower panel) The grazing periodic trajectory corresponding to G-1 obtained for $V \approx 0.5876$ in the one-parameter continuation. The terminal point of the $\mathbf{J}_5$ segment is given by $\mathbf{x} \approx \begin{pmatrix} \ldots & 0 & 0.5 & 0 & 6.264 \end{pmatrix}^T$. Here, and in the later figures, $\|\mathbf{x}\|_2$ represents a signature-dependent solution norm implemented in AUTO 97.

continuation; the identical single-segment trajectory but with signature $\{\mathbf{J}_1\}$; or a two-segment periodic solution with base signature $\{\mathbf{J}_1, \mathbf{J}_8\}$ obtained by appending to the grazing solution segment an additional zero-time segment coincident with the point of grazing contact. The latter possibility is consistent with the existence of a post-grazing branch of two-segment periodic trajectories with one stick phase terminated through impact and one slip phase per period of excitation shown in the upper panel of Fig. 2.5. Here, the length of the $\mathbf{J}_8$ segment increases from zero as V is changed away from the parameter value corresponding to grazing. The lower panel of Fig. 2.5 shows the grazing periodic solution obtained for $V \approx 0.7305$ that attains a grazing contact with the event surface corresponding to h_{front} along the $\mathbf{J}_1$ segment.

It is clear from this figure that the periodic orbits immediately after grazing are linearly unstable. In fact, as documented in [15], one of the corresponding Floquet multipliers grows in magnitude beyond all bounds as the G-1 point is approached along this branch, but is here found to be bounded on any segment of the branch not containing the G-1 point.

As a starting solution for a two-parameter continuation of the grazing bifurcation curve through the point

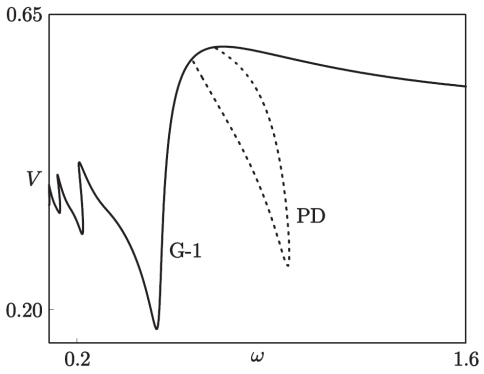

Figure 2.4: Period-doubling (dotted) and grazing bifurcation (solid) curves obtained in a two-parameter continuation with signature $\{\mathbf{J}_5\}$. The initial periodic solutions for these continuations are obtained from the one-parameter continuation shown in the upper panel of Fig. 2.3.

marked G-2 in the upper panel of Fig. 2.5, it is possible to use a three-segment periodic trajectory with signature $\{\mathbf{J}_1, \mathbf{J}_1, \mathbf{J}_8\}$ obtained by splitting the $\mathbf{J}_1$ segment of the grazing periodic trajectory at the point of grazing contact. Alternatively, again reflecting the signature and structure of the post-grazing family of periodic trajectories emanating from the grazing bifurcation, the starting solution may be given by a four-segment periodic solution with base signature $\{\mathbf{J}_1, \mathbf{J}_8, \mathbf{J}_1, \mathbf{J}_8\}$ where an additional zero-time segment coincident with the point of grazing contact has been inserted in between the two $\mathbf{J}_1$ segments.

The corresponding single-parameter branch of four-segment periodic trajectories with signature $\{\mathbf{J}_1, \mathbf{J}_8, \mathbf{J}_1, \mathbf{J}_8\}$, i.e., with two stick phases terminated through impact and two slip phases per period of excitation, is shown in the upper panel of Fig. 2.6. The lower panel of Fig. 2.6 shows the grazing periodic solution for $V \approx 0.8095$ that attains a grazing contact with the event surface corresponding to h_{front} along one of the $\mathbf{J}_1$ segments.

Reference to the upper panels of Fig. 2.5 and Fig. 2.6 show a discontinuity in the tangent direction to the branch of periodic trajectories at the point G-2. This is again consistent with the discontinuity-mapping based analysis in [15, 81].

In a similar fashion, the procedure outlined here can be implemented for the continuation of multisegment periodic solutions of the microactuator hybrid dynamical system with multiple stick and slip phases per period of excitation (cf. upper and lower panels of Fig. 2.7). The results of such an analysis for large variations in V and ω are shown in the bifurcation diagram in Fig. 2.8.

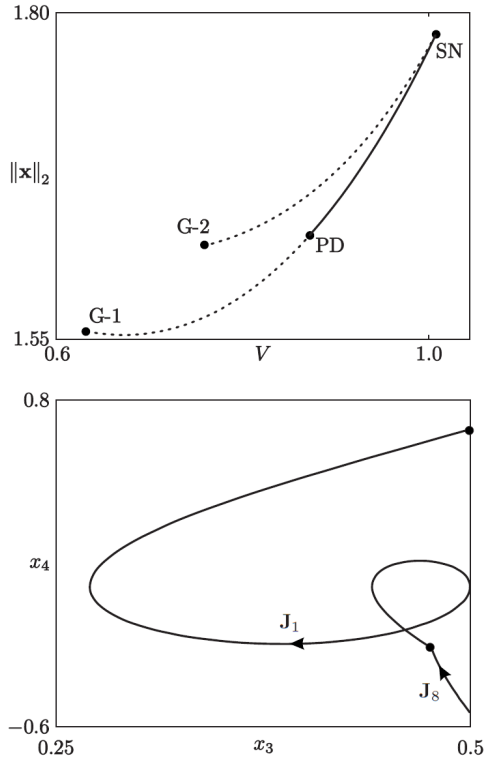

Figure 2.5: (upper panel) A branch of periodic solution trajectories with base unit signature $\{\mathbf{J}_1, \mathbf{J}_8\}$ obtained from a one-parameter continuation in V for $\omega \approx 0.9189$. (lower panel) The grazing periodic trajectory corresponding to G-2 obtained for $V \approx 0.7305$ in the one-parameter continuation. The terminal point of the $\mathbf{J}_1$ segment is given by $\mathbf{x} \approx \begin{pmatrix} \ldots & 0 & 0.5 & 0.674 & 3.846 \end{pmatrix}^T$.

2.4 Discussion

The latter part of this chapter has illustrated the use of a computational toolbox for the continuation of periodic solution trajectories of hybrid dynamical systems by applying it to the bifurcation analysis of an example impact microactuator. In particular, branches of multisegment periodic solution trajectories with several distinct signatures have been continued under variations in a single parameter. Furthermore, bifurcation curves corresponding to the locus of period-doubling, saddle-node, and grazing bifurcation points have been continued under variations in two parameters. The discussion has demonstrated the ease with which the results of one-parameter continuations may be used to seed two-parameter continuations and the alternative descriptions for the continuation of grazing bifurcation curves that reflect the transition between distinct solution signatures.

Grazing bifurcation curves have here been characterized solely in terms of a condition of tangential contact of a solution segment and a subsequent resegmentation for continuation past this condition. The numerical results have demonstrated that transitions across such bifurcation curves are, nevertheless, associated with

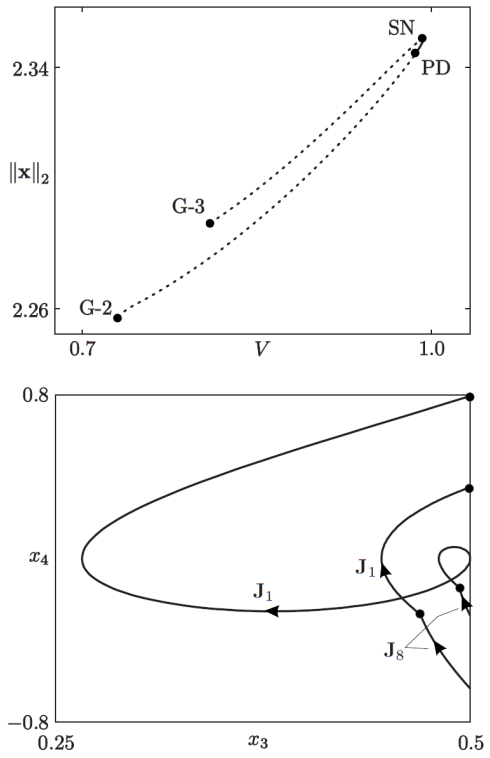

Figure 2.6: (upper panel) A branch of periodic solution trajectories with base unit signature $\{\mathbf{J}_1, \mathbf{J}_8, \mathbf{J}_1, \mathbf{J}_8\}$ obtained from a one-parameter continuation in V for $\omega \approx 0.9189$. (lower panel) The grazing periodic trajectory corresponding to G-3 obtained for $V \approx 0.8095$. The terminal point of the longest $\mathbf{J}_1$ segment is given by $\mathbf{x} \approx \begin{pmatrix} \dots & 0 & 0.5 & 0.794277 & 3.509 \end{pmatrix}^T$.

changes in the linear stability characteristics (cf. branches terminating at points G-1 in Figs. 2.3 and 2.5) as well as the number of periodic solution trajectories of period equal to that of the excitation (cf. branches terminating at points G-2 inf Figs. 2.5 and 2.6). Indeed, in impact oscillators, multiple solution branches of periodic trajectories of period equal to a multiple of that of the excitation may also emanate from such grazing bifurcation points (cf., [55]). These observations justify the use of the terminology grazing bifurcation curves to denote the locus of parameter values corresponding to tangential contact.

The bifurcation behavior documented may provide impetus to the design of the actuator for specific applications. For instance, to achieve a consistent step size with minimum input voltage and a maximum tolerance to deviations in that input, ω can be tuned near resonance ($\omega \approx 0.4878$), where an asymptotically stable behavior exists for a relatively large range of excitation amplitudes. Similar observations regarding the distribution of bifurcation curves in parameter space may be used to tune system parameters so as to achieve a desirable response of the actuator.

The numerical analysis has demonstrated that the period-doubling and saddle-node bifurcation curves terminate on grazing bifurcation curves at *co-dimension-two bifurcation points* in the (ω, V) parameter

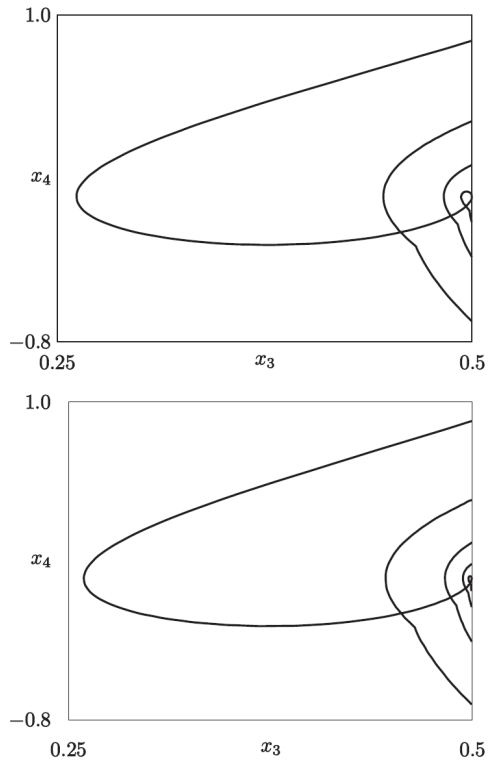

Figure 2.7: (upper panel) The grazing periodic trajectory obtained for $V \approx 0.8559$ in the one-parameter continuation of a six-segment solution with base unit signature $\{\mathbf{J}_1, \mathbf{J}_8, \mathbf{J}_1, \mathbf{J}_8, \mathbf{J}_1, \mathbf{J}_8\}$. (lower panel) The grazing periodic trajectory obtained for $V \approx 0.8819$ in the one-parameter continuation of an eight-segment solution with base unit signature $\{\mathbf{J}_1, \mathbf{J}_8, \mathbf{J}_1, \mathbf{J}_8, \mathbf{J}_1, \mathbf{J}_8, \mathbf{J}_1, \mathbf{J}_8\}$.

space. For example, the saddle-node and period-doubling bifurcation curves corresponding to a two-segment periodic solution intersect at $\omega \approx 0.6136$ and $V \approx 0.5816$, which also corresponds to a grazing bifurcation point. A similar phenomenon can be observed at $\omega \approx 0.4878$ and $V \approx 0.1710$ (see Fig. 2.8). This observation supports the analysis performed on such co-dimension-two bifurcation points in recent work by members of Prof. Dankowicz's group ([15, 66, 81]).

Two distinct limiting behaviors corresponding to $\omega \ll 1$ and $\omega \gg 1$ were observed here. In particular, as seen in Fig. 2.9, for $\omega \ll 1$ all grazing bifurcations curves converge to $V \approx 0.385$. This agrees with the static pull-in voltage for a parallel-plate capacitor given by

$$V_{\text{pull-in}} = \frac{2d}{3}\sqrt{\frac{kd}{3\alpha}} \tag{2.29}$$

(cf. [42]).

For $\omega \gg 1$, the grazing bifurcation curves tend to become horizontal and separated by a frequency-independent distance. To investigate the apparent accumulation of these bifurcation curves, denote by V_i

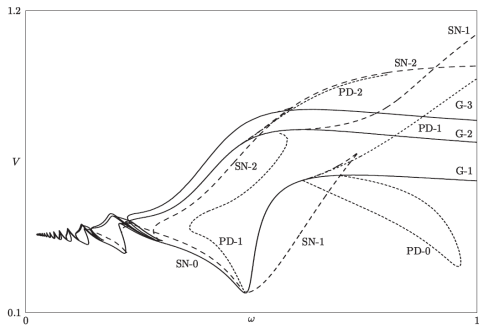

Figure 2.8: Bifurcation diagram showing period-doubling, saddle-node and grazing bifurcation curves corresponding to periodic solutions with one or several segments. Here, PD-n, SN-n, and G-n represent the period-doubling, saddle-node and grazing bifurcation curves corresponding to periodic solutions with n impacts per period. Dotted, dashed and solid curves represent period-doubling, saddle-node, and grazing bifurcation curves, respectively.

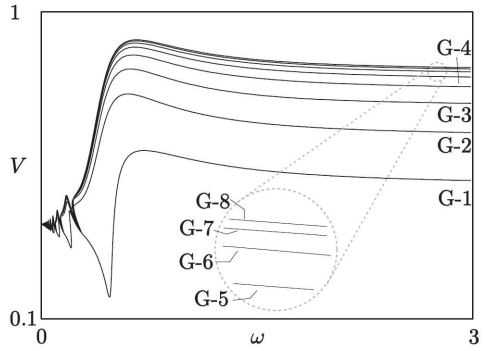

Figure 2.9: Grazing bifurcation curves obtained through two-parameter continuation.

the voltage for which a periodic trajectory with i impacts per period attains grazing contact with the event surface corresponding to h_{front}, and let

$$\lambda_i = \frac{V_{i+2} - V_{i+1}}{V_{i+1} - V_i}$$

For example, for $\omega \approx 2.0056$, we find $V_1 \approx 0.5275$, $V_2 \approx 0.6664$, $V_3 \approx 0.7494$, $V_4 \approx 0.7990$, $V_5 \approx 0.8271$, $V_6 \approx 0.8424$, $V_7 \approx 0.8503$, and $V_8 \approx 0.8543$, and thus $\lambda_1 \approx 0.5978$, $\lambda_2 \approx 0.5968$, $\lambda_3 \approx 0.5686$, $\lambda_4 \approx 0.5417$, $\lambda_5 \approx 0.5191$, and $\lambda_6 \approx 0.5038$. This near-self-similarity observed in the spacing of the grazing bifurcation curves for large ω appears to also be sustained for mid-range values of ω. Indeed, for $\omega \approx 0.9189$, we find $\lambda_1 \approx 0.5528$, $\lambda_2 \approx 0.5873$, and $\lambda_3 \approx 0.5603$. Similarly, [83] reported $\lambda_i \approx 0.5$ for the case when $\omega = 0.5$.

These results argue for the existence of a limiting bifurcation curve corresponding to periodic orbits of infinitely many impacts per period accumulating from the left on the final point of grazing contact, i.e., the onset of chatter. Although the shape of this chatter bifurcation curve would be expected to be sensitive to the introduction of higher modes of natural oscillations of the impactor/suspension structure (the model description presented here is an approximation based on the fundamental mode of vibration of

the impactor/suspension structure), it would be interesting to investigate the rate of convergence toward this curve and its dependence on system parameters. This could be an interesting topic for future work.

We return to the MEMS context in Chapter 6, where a modified version of the Mita device is discussed. A design is proposed which places the stops such that, under suitable driving conditions, a grazing bifurcation triggers snap-through of the parallel-plate drive. This creates a MEMS implementation of a limit-switch sensor which closes a circuit as a result of reaching a critical value of the input signal.

The next chapter goes on to consider grazing contact in the context of an electrostatically actuated microbeam. In this example, the beam is modelled as a continuum that is subsequently descretized using the method of assumed modes. Intermittent contact with a barrier at a point along the span of the beam is modelled as compliant contact with a stiff, conservative spring. A series of reduced order models are then considered which explore responses with different contact stiffnesses and different numbers of retained modes.

Chapter 3

Grazing-Induced Dynamics in a Unilaterally-Constrained Beam

3.1 Introduction

Where the last chapter studied a lumped-parameter model of a mechanical system, this chapter presents a study of an electrostatically-actuated, microscale Euler-Bernoulli beam whose behavior is described by a partial differential equation. This PDE is discretized using the Galerkin method and a sequence of reduced-order models are considered. This example demonstrates numerical simulation techniques used in later chapters and discusses the choice of contact law.

In the next section, an electromechanical model is developed of a simple parallel-plate capacitor design in which a deformable, doubly-clamped, slender beam constitutes one of the electrodes. The model includes leading-order geometric nonlinearities as well as corrections to the leading electrostatic interaction due to the fringe effects from the finite width and thickness of the beam. The model also accounts for a localized mechanical interaction with a low-compliance stop that limits the lateral deflection of the beam at the location of the stop. Section 3.3 reviews the characteristic features of grazing-induced bifurcations in mechanical systems with rigid impact and compliant contact. Section 3.4 presents numerical results from simulations of reduced-order models with different numbers of mechanical modes and demonstrates the changes in system response associated with the onset of low-relative-velocity contact. The chapter concludes with a discussion of the main observations and implications for future study.

3.2 Model Development

Electrostatic interactions between parts of a MEMS device at different electric potentials are a dominant contributor to the mechanical load and provide a useful mechanism for actuation. A common implementation is a simple parallel-plate capacitor in which one of the plates is suspended and capable of motion relative to the other plate. This configuration includes the possibility of snap-through and subsequent sustained contact between the two plates when the voltage excitation exceeds a critical pull-in value.

In Batra *et al.* [6] (see also [10, 36, 35]), the pull-in voltage characteristic of a fold in the equilibrium manifold for electrostatically actuated microbeams is investigated when accounting for geometric nonlinearities in the beam dynamics due to large deflections, large rotations, but small strains, and nontrivial corrections to the effective capacitance due to fringe effects from finite beam width and thickness. Specifically, the equilibrium equations are projected onto a subset of mechanical modes and conditions for criticality are investigated numerically. Here, a similar model is adopted for the study of grazing-induced changes in the beam dynamics following the onset of low-velocity contact with a low-compliance mechanical element. A representation of this model is shown in Fig. 3.1.

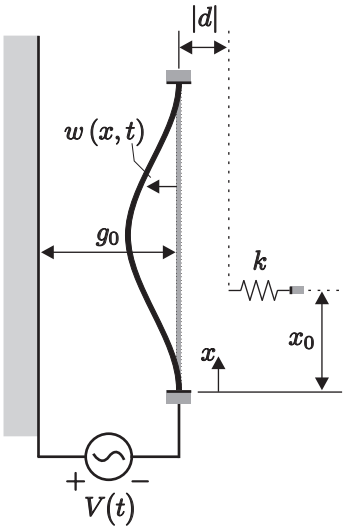

Figure 3.1: Schematic of an electrostatically actuated doubly-clamped microbeam with deflections limited by the presence of a low-compliance mechanical element at $x = x_0$.

3.2.1 Beam Dynamics

Consider a uniform microbeam of length l, width b, and thickness h. Let ρ represent the mass density per unit volume and I the area moment of inertia about the principal inertia axis normal to the assumed plane of flexure. Finally, denote by E the Young's modulus of the beam. Following Batra *et al.* [6] (see also [38]), let $w(x,t)$ denote the lateral deflection of the beam at longitudinal coordinate x and time t (cf. Fig. 3.1). Then, in the absence of axial load in the undeformed configuration, the governing equation of motion is given by

$$\rho bhw_{tt} + EIw_{xxxx} - \frac{Ebh}{2l} w_{xx} \int_0^l w_x^2 dx = F(w), \tag{3.1}$$

where F denotes the distributed force per unit length due to the electrostatic and mechanical interactions. Here, subscripts denote partial derivatives with respect to space and time. Finally, assuming a doubly-clamped beam, the boundary conditions are

$$w, w_x|_{x=0,l} = 0. \tag{3.2}$$

3.2.2 Electrostatic Interactions

Denote by g the pointwise distance separating the deformed beam from a stationary electrode, such that $g \equiv g_0$ in the undeformed configuration. For narrow microbeams with $0.2 \leq h/b \leq 2$ and $0.4 \leq h/g \leq 5$ the electrostatic attraction toward the electrode is approximately given by the expression

$$F_e(w) = \frac{\varepsilon}{2} \frac{bV^2}{(g_0 - w)^2} \mathcal{F}, \tag{3.3}$$

where the nontrivial terms in

$$\mathcal{F} = 1 + \left[0.204 + 0.6 \left(\frac{h}{b}\right)^{0.24}\right] \left(\frac{g_0 - w}{b}\right)^{0.76} \tag{3.4}$$

represent fringe effect corrections due to the finite width and thickness of the beam [5] (see also [4]). Here, ε is the electrical permittivity of the dielectric separating the beam and the electrode and V is the voltage difference between the beam and the electrode.

3.2.3 Mechanical Interactions

With the inclusion of a localized mechanical stop at an interior point $x = x_0$ and displaced laterally relative to the undeformed configuration of the beam by d (see Fig. 3.1, corresponding to a case where $d < 0$), mechanical interactions occur for $\text{signum}(d)\, w|_{x=x_0} \geq |d|$. Here, for simplicity, these are modeled as resulting from a linear restoring force with stiffness k, such that

$$F_c(w) = -k(w - d)\,\delta(x - x_0) \tag{3.5}$$

where δ is the Dirac delta function. This treatment avoids violating the continuum modeling assumptions. A non-compliant contact law which prescribes a change in velocity at a discrete point of contact, as used in the last chapter, is inconsistent for this situation, where a continuous velocity field is assumed to exist. For other studies of microbeam dynamics in the presence of contact see, for example, [2, 69, 68, 77].

3.2.4 Non-Dimensional Representation

The substitution

$$w(x,t) = l\tilde{w}\left(\frac{x}{l}, \sqrt{\frac{EI}{\rho bhl^4}}t\right) \tag{3.6}$$

yields the non-dimensionalized beam equation

$$\tilde{w}_{\tilde{t}\tilde{t}} + \tilde{w}_{\tilde{x}\tilde{x}\tilde{x}\tilde{x}} - \frac{\gamma}{2}\tilde{w}_{\tilde{x}\tilde{x}}\int_0^1 \tilde{w}_{\tilde{x}}^2 d\tilde{x} = \tilde{F}(\tilde{w}) \tag{3.7}$$

and boundary conditions

$$\tilde{w}, \tilde{w}_{\tilde{x}}|_{\tilde{x}=0,1} = 0 \tag{3.8}$$

where

$$\tilde{F}(\tilde{w}) = \frac{l^3}{EI}F(l\tilde{w}) \tag{3.9}$$

and

$$\tilde{x} = \frac{x}{l}, \tilde{t} = \sqrt{\frac{EI}{\rho bhl^4}}t, \gamma = \frac{bhl^2}{I}. \tag{3.10}$$

Here,

$$\frac{l^3}{EI}F_e(l\tilde{w}) = \frac{\tilde{V}^2}{(\tilde{g}_0 - \tilde{w})^2}\tilde{\mathcal{F}} \tag{3.11}$$

where

$$\tilde{\mathcal{F}} = 1 + \left[0.204 + 0.6\left(\frac{\tilde{h}}{\tilde{b}}\right)^{0.24}\right]\left(\frac{\tilde{g}_0 - \tilde{w}}{\tilde{b}}\right)^{0.76} \tag{3.12}$$

and

$$\tilde{g}_0 = \frac{g_0}{l}, \tilde{b} = \frac{b}{l}, \tilde{h} = \frac{h}{l}, \tilde{V}^2 = \frac{\varepsilon V^2 bl}{2EI}. \tag{3.13}$$

Similarly,

$$\frac{l^3}{EI}F_c(l\tilde{w}) = -\tilde{k}\left(\tilde{w} - \tilde{d}\right)\delta_{\tilde{x}_0} \tag{3.14}$$

where

$$\tilde{d} = \frac{d}{l}, \tilde{x}_0 = \frac{x_0}{l}, \tilde{k} = \frac{kl^3}{EI}. \tag{3.15}$$

3.2.5 Projection

For a reduced-order description, we decompose the lateral deflection according to

$$\tilde{w}\left(\tilde{x}, \tilde{t}\right) = q_i\left(\tilde{t}\right)\phi_i(\tilde{x}) \tag{3.16}$$

where a repeated index implies summation from 1 to some integer N and ϕ_i denotes a set of sufficiently smooth trial functions that satisfy the boundary conditions. Substitution into Eqn. (3.1) and integration over x with weight ϕ_m then yields

$$\ddot{q}_i \Lambda_{im} + q_i \Lambda''_{im} + \frac{\gamma}{2} q_i q_j q_k \Lambda'_{im} \Lambda'_{jk} = \int_0^1 \tilde{F}\left(q_i \phi_i\right) \phi_m d\tilde{x} \tag{3.17}$$

using integration by parts and the boundary conditions (3.2), where

$$\Lambda_{ij} = \int_0^1 \phi_i \phi_j dx, \Lambda'_{ij} = \int_0^1 \phi'_i \phi'_j dx, \Lambda''_{ij} = \int_0^1 \phi''_i \phi''_j dx. \tag{3.18}$$

In particular, in a single-mode approximation

$$\ddot{q}\Lambda_{11} + q\Lambda''_{11} + \frac{\gamma}{2} q^3 \Lambda'^2_{11} = \int_0^1 \tilde{F}\left(q\phi\right) \phi d\tilde{x} \tag{3.19}$$

For example, with the trial function

$$\phi\left(x\right) = 16\tilde{g}_0 \tilde{x}^2 \left(\tilde{x} - 1\right)^2 \tag{3.20}$$

found in Batra *et al.* [5] to approximate the static beam shape under small constant voltages it follows that

$$\Lambda_{11} = \frac{128\tilde{g}_0^2}{315}, \Lambda'_{11} = \frac{512\tilde{g}_0^2}{105}, \Lambda''_{11} = \frac{1024\tilde{g}_0^2}{5}. \tag{3.21}$$

Alternatively, in the case that the trial functions are chosen as the first N spatial eigenmodes of the doubly-clamped Euler-Bernoulli beam normalized such that $\Lambda_{ij} = \delta_{ij}$, it follows that $\Lambda''_{ij} = \omega_i^2 \delta_{ij}$ (no sum over i), where ω_i is the i-th modal frequency (see Table 3.1). Moreover, from symmetry $\Lambda'_{ij} = 0$ for i and j of unequal parity. In contrast, for i and j of equal parity, Table 3.1 shows the corresponding values of Λ'_{ij} for $N = 5$. Similarly, symmetry implies that the odd subspace $q_2 \equiv q_4 \equiv \ldots \equiv q_{2\lfloor N/2 \rfloor} \equiv 0$ is invariant in the absence of mechanical contact or when $\tilde{x}_0 = 1/2$.

For the mechanical interaction with the compliant stop,

$$\int_0^1 \tilde{F}_c\left(q_i \phi_i\right) \phi_m d\tilde{x} = -\tilde{k}\left(q_i \left.\phi_i\right|_{\tilde{x}=\tilde{x}_0} - \tilde{d}\right) \left.\phi_m\right|_{\tilde{x}=\tilde{x}_0}. \tag{3.22}$$

The contribution from the electrostatic interaction to the integrand on the right-hand side of Eqn. (3.17), however, is a non-polynomial expression in the modal amplitudes and trial functions. To enable efficient numerical implementation of the projected equations of motion, it becomes necessary to consider suitable

Table 3.1: Values of ω_i and λ'_{ij} rounded off to 3 significant digits for $i \leq j$ and even $i - j$ in the case of the first 9 spatial eigenmodes of the doubly-clamped Euler-Bernoulli beam.

ω_1	22.4	Λ'_{11}	12.3	Λ'_{33}	98.9	Λ'_{59}	-38.0
ω_2	61.7	Λ'_{13}	-9.73	Λ'_{35}	-24.3	Λ'_{66}	376
ω_3	121	Λ'_{15}	-7.62	Λ'_{37}	-23.0	Λ'_{68}	-44.7
ω_4	200	Λ'_{17}	-6.11	Λ'_{39}	-20.9	Λ'_{77}	508
ω_5	299	Λ'_{19}	-5.07	Λ'_{44}	172	Λ'_{79}	-51.2
ω_6	417	Λ'_{22}	46.1	Λ'_{46}	-31.3	Λ'_{88}	660
ω_7	555	Λ'_{24}	-17.1	Λ'_{48}	-30.6	Λ'_{99}	836
ω_8	713	Λ'_{26}	-15.2	Λ'_{55}	264		
ω_9	891	Λ'_{28}	-13.1	Λ'_{57}	-38.0		

approximations that reduce the evaluation of the integral to that of a polynomial approximant or to a fixed-step quadrature approximant. In the first case, the expression for the electrostatic interaction, assuming $\tilde{w} \ll 1$, could be expanded to some desired order. Approximation errors would be due to the order of truncation in the Taylor expansion whereas the integrals for each monomial could be obtained off-line with arbitrary accuracy.

Alternatively, retaining the full nonlinear form of the integrand, but replacing the integral by a linear combination of the integrand evaluated at selected interior points of the integration domain allows for larger values of w. Here, approximation errors would be due to the resolution of the partition of the integration domain. In this initial investigation, we adopt Simpson's rule

$$\int_0^1 \tilde{F}_e\left(q_i\phi_i\right)\phi_m d\tilde{x} = \frac{2}{3n}\left[\begin{array}{c} \sum_{k=1}^{\frac{n}{2}-1} \tilde{F}_e\left(q_i\phi_i\right)\phi_m\Big|_{\tilde{x}=2k/n} \\ +2\sum_{k=1}^{\frac{n}{2}} \tilde{F}_e\left(q_i\phi_i\right)\phi_m\Big|_{\tilde{x}=(2k-1)/n} \end{array}\right], \tag{3.23}$$

for some even integer n.

Finally, in the numerical simulations reported below, viscous modal damping was introduced into the projected equations of motion (3.17) with an identical damping factor of ζ for each mechanical mode.

3.3 Grazing Bifurcations

The mechanical model developed above falls into the general class of piecewise-smooth dynamical systems characterized by the existence of state-space surfaces associated with discontinuities in the governing vector field. Such systems are known to exhibit complex behavior, including the coexistence of steady-state solutions, a variety of bifurcation phenomena, and chaos. Of particular interest in the present context are

bifurcations that occur in the immediate vicinity in parameter space to parameter conditions corresponding to the existence of a periodic steady-state trajectory that achieves tangential contact with the discontinuity surface given by

$$h(q) \stackrel{def}{=} q_i \, \phi_i|_{x=x_0} - \tilde{d} = 0. \tag{3.24}$$

Specifically, the analysis emphasizes so-called *discontinuity-induced bifurcations* that would not have occurred for nearby parameter values in the absence of the discontinuity.

3.3.1 Rigid Impacts

In mechanical systems with rigid impacts, the corresponding discontinuity surfaces are associated with instantaneous jumps in the velocity state of the mechanism. A periodic steady-state trajectory that achieves tangential, grazing contact with such a discontinuity surface then corresponds to an oscillation of the system in which mechanical contact occurs with zero relative velocity at some moment during the oscillation. The local dynamics in the vicinity of the corresponding state-space trajectory are significantly different from those in the absence of the discontinuity (see, e.g., [7, 12, 19, 21, 24, 23, 52, 53, 54]).

In particular, let the zero-level surface of h_{impact} represent the discontinuity surface such that only $h_{\text{impact}} > 0$ is accessible to the system dynamics. Denote by $\mathbf{x}^*$ the point of grazing contact of the steady-state trajectory, such that $h_{\text{impact}}(\mathbf{x}^*) = 0$. Suppose that the grazing trajectory is a member of a family of periodic trajectories of the mechanical system in the absence of impacts, which is parametrized by a parameter μ and denote by $\mathbf{x}(\mu)$ the local extremum in the distance to the discontinuity surface, such that $\mathbf{x}(\mu^*) = \mathbf{x}^*$. Finally, suppose that

$$\frac{d}{d\mu} h_{\text{impact}}(\mathbf{x}(\mu))\Big|_{\mu=\mu^*} < 0, \tag{3.25}$$

corresponding to a transversal crossing of $\mathbf{x}(\mu)$ with $h_{\text{impact}} = 0$. Then, for $\mu > \mu^*$, the local dynamics necessarily include repeated impacts.

In fact, as follows from the discontinuity-mapping methodology originally introduced by Nordmark [52], the local dynamics in the vicinity of the grazing trajectory are governed by a characteristic nonsmooth normal form in the deviation from grazing. In particular, for initial conditions that lead to impact, the normal form is dominated by terms proportional to the square root of the deviation from the grazing trajectory. The destabilizing influence of these terms due to recurrent impact may or may not be compensated for by stabilizing features of the global dynamics away from impact. In the former case, the resultant steady-state response for $\mu > \mu^*$ exhibits a sequence of discontinuity-induced bifurcations that accumulate on the initial grazing bifurcation at $\mu = \mu^*$. This scenario includes the possibility of robust chaos over open intervals of

values of μ, period-adding sequences, and an infinite collection of additional grazing bifurcations.

In contrast, in the case that the global dynamics fails to compensate for the effects of recurrent impacts, the system response necessarily transitions through a rapid sequence of impacts of increasing relative velocity to a distinct steady-state behavior. This corresponds to a loss of the local attractor and a possibly dramatic, and clearly very sudden, change of system response [15, 81]. This particular behavior will be considered in detail in Chapter 4.

3.3.2 Compliant Collisions

The mechanical model developed previously is one in which the contact condition is modeled through an additional mechanical element that yields a zero contribution to the load in the absence of contact and a load that is proportional to the penetration in the presence of contact (cf. [16, 43, 80]. Here, again, a periodic steady-state trajectory that achieves grazing contact with a discontinuity surface corresponds to an oscillation that exhibits zero-relative-velocity mechanical contact at some moment during the oscillation. In this case, however, the effects of the additional contribution to the force field due to the contact stiffness does not immediately dominate the system response as was the case in the presence of rigid impacts. Instead, for finite, but large values of the contact stiffness, it is expected that the pre-grazing branch of periodic trajectories persists over some small, but nonzero interval of μ near μ^*.

To analyze the occurrence of near-grazing, discontinuity-induced bifurcations in a piecewise-smooth dynamical system with continuous, but not continuously differentiable vector fields, denote by $\mathbf{f}(\mathbf{x}^*, \mu^*)$ the vector field at the point of grazing contact when $\mu = \mu^*$. It follows that

$$\partial_{\mathbf{x}} h_{\text{impact}}(\mathbf{x}^*) \cdot \mathbf{f}(\mathbf{x}^*, \mu^*) = 0 \tag{3.26}$$

corresponding to tangential contact of the corresponding state-space trajectory with $h_{\text{impact}} = 0$. Let

$$h_{\text{turning}}(\mathbf{x}, \mu) = \partial_{\mathbf{x}} h_{\text{impact}}(\mathbf{x}) \cdot \mathbf{f}(\mathbf{x}, \mu) \tag{3.27}$$

and assume that

$$\partial_{\mathbf{x}} h_{\text{turning}}(\mathbf{x}^*, \mu^*) \cdot \mathbf{f}(\mathbf{x}^*, \mu^*) > 0 \tag{3.28}$$

such that $\mathbf{x}^*$ is a local minimum in the value of h_{impact} along the corresponding state-space trajectory. Finally, denote by $\delta\mathbf{x}$ the deviation from $\mathbf{x}^*$ of the intersection with $h_{\text{turning}} = 0$ of a near-grazing trajectory segment governed by the non-contact vector field. From [47] it follows that, for large values of the contact

stiffness, near-grazing periodic trajectories with a single intersection with $h_{\text{turning}} = 0$ correspond to negative roots of the cubic polynomial

$$g(\tau) = \alpha\tau^3 + \tau^2 + \beta \tag{3.29}$$

where α is a constant that can be evaluated based on the system characteristcs at the point of grazing contact and along the grazing trajectory, β depends linearly on $\mu - \mu^*$, and τ^2 is linear in $\delta\mathbf{x}$.

Now suppose that $\alpha < 0$. It follows that β is an increasing function of τ along $g(\tau) = 0$, i.e., that there exists one negative root for $\beta < 0$ and no negative roots for $\beta \geq 0$. In contrast, for $\alpha > 0$, β attains the local minimum $\beta_{\text{fold}} = -\frac{4}{27\alpha^2}$ as a function of τ for $\tau_{\text{fold}} = -\frac{2}{3\alpha}$. It follows that there exist no negative roots of g when $\beta < \beta_{\text{fold}}$, a single negative root when $\beta = \beta_{\text{fold}}$ and $\beta \geq 0$ and a pair of coexisting roots for $\beta_{\text{fold}} < \beta < 0$.

The root manifold of g restricted to $\tau < 0$ is shown in Fig. 3.2. It follows from this that, while the family of steady-state periodic trajectories persists on the domain of validity of the corresponding normal form in the case when $\alpha < 0$, this is no longer the case when $\alpha > 0$. Here, instead, the bifurcation branch under variations in μ exhibits a discontinuity-induced fold bifurcation when $\beta = \beta_{\text{fold}}$ and the associated loss of a local attractor. The near-grazing dynamics necessarily transition to a distinct steady-state behavior, much as was the case in the limit of rigid impacts considered in the previous section.

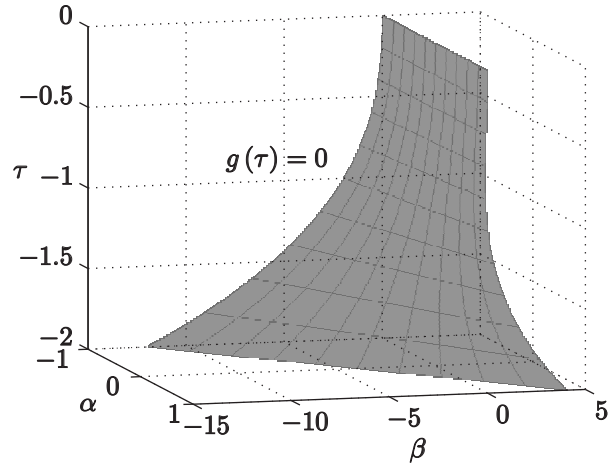

Figure 3.2: Root manifold of the cubic polynomial $g(\tau)$ for $\tau < 0$. here, a single root is found for $\alpha < 0$ and $\beta < 0$. In contrast, for $\alpha > 0$ a fold occurs in the root manifold under variations in β corresponding to a discontinuity-induced loss of a local attractor and a transition to a distinct steady-state behavior.

3.4 Numerical Results

Numerical simulations were performed to investigate the steady-state response of the electrostatically actuated microbeam for excitation voltages given by

$$\tilde{V}\left(\tilde{t}\right) = \begin{cases} \tilde{V}_{amp} & \mod\left(\tilde{t}, \frac{2\pi}{\omega}\right) \in \left[0, \frac{\pi}{\omega}\right) \\ 0 & \mod\left(\tilde{t}, \frac{2\pi}{\omega}\right) \in \left[\frac{\pi}{\omega}, \frac{2\pi}{\omega}\right) \end{cases} \tag{3.30}$$

corresponding to pulse trains of period $2\pi/\omega$ and amplitude $\tilde{V}_{amp}$. Emphasis was placed on changes in the response associated with the onset of low-velocity contact with the mechanical stop at $\tilde{x} = \tilde{x}_0$ for excitation amplitudes in the vicinity of some critical value $\tilde{V}^*_{amp}$. In all cases reported below, $\gamma = 3 \times 10^4$, $\tilde{h} = 0.02$, $\tilde{b} = 0.01$, $\tilde{g}_0 = 0.04$, $\omega = 28$, and $\tilde{x}_0 = 0.5$. While the results shown were obtained with $n = 20$, selected results were validated with $n = 100$.

Suppose that $\tilde{d} = -0.004$. With a single-mode approximation given by the lowest-order fundamental mode shape of the Euler-Bernoulli beam, a grazing periodic steady-state trajectory is found for $\tilde{V}^*_{amp} \approx 0.03$. The corresponding variations in mid-span deflection and velocity are represented by the dotted closed curve in Fig. 3.3. A grazing, periodic steady-state trajectory may similarly be found with the inclusion of additional mechanical modes with an apparent convergence in modal contributions (errors $\sim 10^{-7}$) and critical parameter value already for $N \geq 1$.

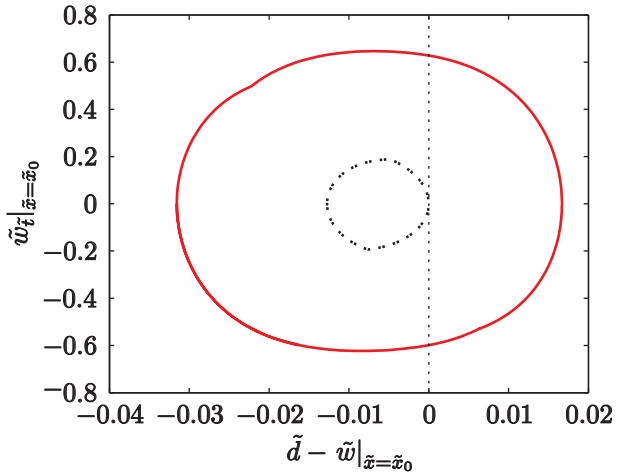

Figure 3.3: A single-mode approximation of the grazing periodic steady-state trajectory (dotted) along a branch of low-penetration oscillations that terminates at a cyclic fold bifurcation for $\tilde{V}_{amp} \approx 0.033$ and the periodic steady-state trajectory (solid) along the coexisting branch of high-penetration oscillations found for $\tilde{V}_{amp} = 0.033$.

Figure 3.4 shows the variations in the *penetration*, $\max\left(\tilde{d} - \tilde{w}|_{\tilde{x}=\tilde{x}_0}\right)$, for the single-mode model under

changes in the excitation voltage near $\tilde{V}^*_{amp}$ in the case that $\tilde{k} = 100$. The bifurcation diagram shows the coexistence, over a range of post-grazing excitation amplitudes, of a branch of asymptotically stable periodic steady-state trajectories with relatively small values of penetration and a branch of asymptotically stable periodic steady-state trajectories with relatively large values of penetration. Indeed, whereas the former branch terminates at a cyclic fold bifurcation at $\tilde{V}_{amp} \approx 0.033$, the latter persists for values of the excitation amplitude below the critical value and terminates at a cyclic fold bifurcation at $\tilde{V}_{amp} \approx 0.023$.

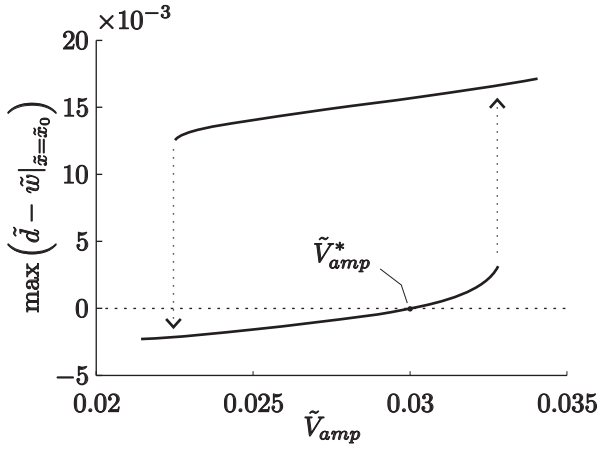

Figure 3.4: Variations in penetration for the single-mode model under changes in the excitation voltage $\tilde{V}_{amp}$ in the case that $\tilde{k} = 100$.

The transition of the steady-state response from the low-penetration to the high-penetration branch is accompanied by a dramatic change in overall oscillation amplitude as well as mid-span velocity at the moment of contact. Figure 3.5 shows the variations in the contact velocity under changes in the excitation voltage near $\tilde{V}^*_{amp}$. Indeed, as further illustrated by the solid closed curve in Fig. 3.3, the contact velocity along the high-penetration branch is similar in magnitude to the maximum mid-span velocity throughout the oscillation.

That the transition from the low-penetration to the high-penetration branch is induced by the onset of low-velocity contact is supported by a bifurcation analysis performed in the case that $\tilde{k} = 0$, corresponding to the absence of the mechanical stop. Here, the low-penetration branch (where penetration is again defined by the above expression) persists for larger changes in $\tilde{V}_{amp}$ and terminates at a cyclic fold bifurcation near $\tilde{V}_{amp} \approx 0.036$. In this case, the transient dynamics appear to result in an unbounded growth in mid-span velocity in the direction of the stationary electrode corresponding to a snap-through transition to an electrostatically singular contact between the electrodes.

The high-amplitude, high-penetration response includes measurable contributions from higher-order mechanical modes that modify the amplitudes of lower-order modes. Specifically, for $N = 9$, the ratios of the

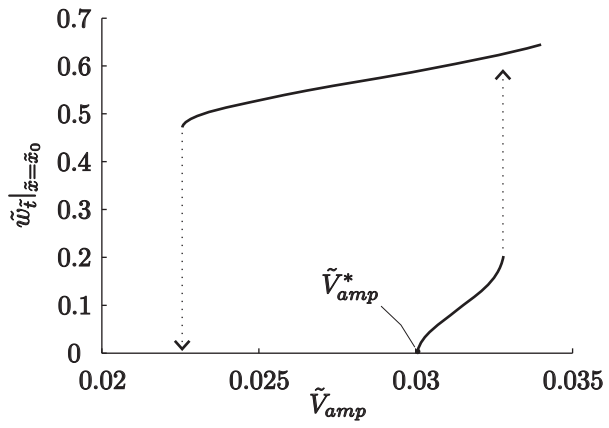

Figure 3.5: Variations in contact velocity for the single-mode model under changes in the excitation voltage $\tilde{V}_{amp}$ in the case that $\tilde{k} = 100$.

maximum magnitude of the amplitude of the higher-order modes to that of the lowest-order mode equal 3% for $i = 3$, .6% for $i = 5$, .1% for $i = 7$, and .05% for $i = 9$. Moreover, the case when $N = 1$ predicts a value of $\max_t q_1(t)$ within 3% of that obtained in the case when $N = 9$. This error is reduced to .1% for $N \geq 5$. Similarly, the relative error in the value of $\max_t q_3(t)$ is 2% in the case when $N = 3$ and less than .5% for $N \geq 5$.

Substantial contributions from higher-order mechanical modes occur in the post-grazing response as k is increased. Figure 3.6 shows the variations in penetration for the single-mode model and the nine-mode model under changes in the excitation voltage near $\tilde{V}^*_{amp}$ in the case that $k = 500$. In this case, the pre-grazing branch of asymptotically stable, periodic, steady-state trajectories appears to terminate in close conjunction to the critical excitation amplitude. Here, again, a branch of high-penetration, high-amplitude oscillatory responses is found over an interval of values of $\tilde{V}_{amp}$ near $\tilde{V}^*_{amp}$. In this case, for $N = 9$, the ratios of the maximum magnitude of the amplitude of the higher-order modes to that of the lowest-order mode equal 5% for $i = 3$, .4% for $i = 5$, .2% for $i = 7$, and .05% for $i = 9$. Moreover, the case when $N = 1$ again predicts a value of $\max_t q_1(t)$ within 3% of that obtained in the case when $N = 9$. This error is reduced to .1% for $N \geq 5$. Similarly, the relative error in the value of $\max_t q_3(t)$ is .2% in the case when $N = 3$ and less than .002% for $N \geq 5$.

The qualitative features of the bifurcation diagram for $k = 500$ persist in the case that $k = 5000$ (cf. Fig. 3.7). In this case, for $N = 9$, the ratios of the maximum magnitude of the amplitude of the higher-order modes to that of the lowest-order mode equal 11% for $i = 3$, 2% for $i = 5$, .5% for $i = 7$, and .2% for $i = 9$. Moreover, the case when $N = 1$ predicts a value of $\max_t q_1(t)$ within 5% of that obtained in the case when $N = 9$. This error is reduced to .1% for $N \geq 7$. Similarly, the relative error in the value of $\max_t q_3(t)$ is 6%

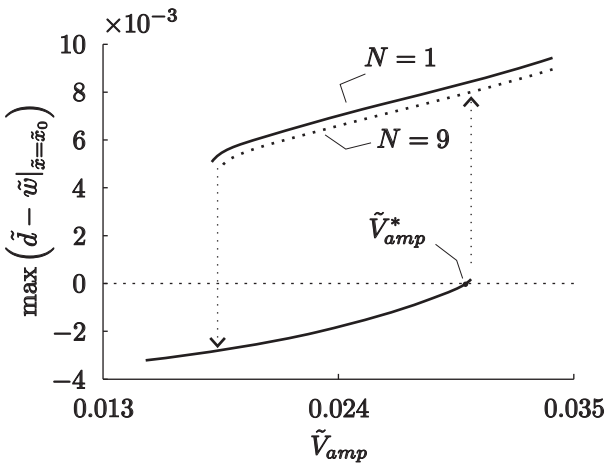

Figure 3.6: Variations in penetration for the single-mode model and the nine-mode model under changes in the excitation voltage $\tilde{V}_{amp}$ in the case that $\tilde{k} = 500$.

in the case when $N = 3$ and less than .2% for $N \geq 7$.

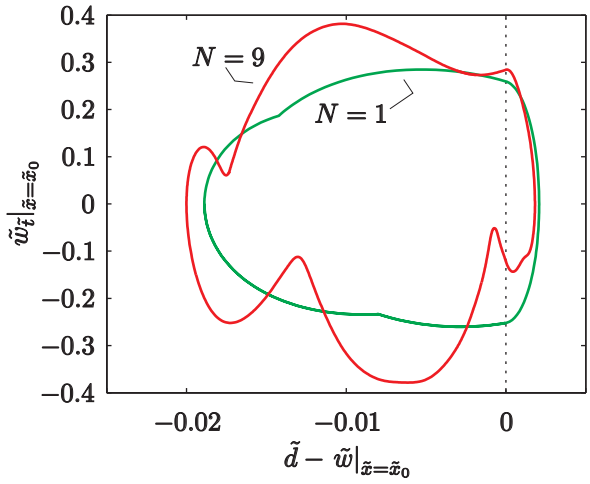

Figure 3.7: Post-grazing, high-amplitude steady-state response using the single-mode and nine-mode approximations for $\tilde{V}_{amp} = 0.03$ and $\tilde{k} = 5000$.

3.5 Discussion

The results in the previous section document grazing-induced, dramatic changes in system response of the beam dynamics across small intervals containing the critical parameter value. In agreement with the theory of grazing bifurcations in systems with compliant contact, the onset of low-velocity contact has been found to result in the termination of a pre-grazing branch of periodic steady-state oscillations through a cyclic fold bifurcation. The loss of a local attractor has been shown to result in a transition to a branch of high-amplitude

steady-state oscillations. While the pre-grazing solution is dominated by the lowest-order mechanical mode, the high-amplitude post-grazing response includes measurable contributions from higher-order mechanical modes that cannot be neglected in the limit of small compliance.

As was mentioned in Sec. 3.3, the system response to a grazing bifurcation is expected to be quite dramatic. The next chapter investigates in detail the transient response of a mechanical system undergoing a grazing bifurcation. Analytical, numerical, and experimental results are presented which indicate that as the bifurcation point is approached, the system response rate grows without bound. It is this behavior which suggests using the grazing bifurcation as a mechanism for a fast-acting limit switch sensor.

Chapter 4

Transient Behavior Near a Nonsmooth Fold Bifurcation

4.1 Introduction

In this chapter analytical, numerical, and experimental methods are employed to investigate the near-grazing transient behavior in a representative, rigid-body mechanical system. It is shown that the rate of growth of successive impact velocities increases beyond all bounds as the threshold parameter value is approached. A limit switch based on the proposed nonsmooth fold scenario would thus be expected to outperform one that relies on a smooth bifurcation, such as the cyclic-fold bifurcation, in terms of switching speed and sensitivity.

Generalizations to periodic steady-state attractors of the snap-like action due to saddle-node bifurcations of equilibria have been proposed recently for limit-switch design using nonlinear circuitry as well as parametrically excited microelectromechanical devices [1, 49, 51, 60, 67, 70, 71, 78, 79]. The corresponding cyclic-fold bifurcation is characterized by the mutual annihilation of a stable and unstable periodic trajectory beyond the threshold value. Using center-manifold theory and the theory of normal forms, the local dynamics in the vicinity of a cyclic-fold bifurcation may be described by the discrete map

$$x_{n+1} = x_n + \mu + x_n^2, \tag{4.1}$$

where μ denotes the deviation of the system parameter from the threshold value and x_n and x_{n+1} parametrize the deviation from the periodic trajectory at $\mu = 0$ upon successive intersections of a state-space trajectory with a suitably defined Poincaré surface [37]. Here, $x_{n+1} = x_n = x_*$ for some μ corresponds to a periodic response of the continuous state of the device. In particular, it follows that there exist two such periodic responses with $x_* \approx 0$ for $\mu \lesssim 0$, one when $\mu = 0$, and none for $\mu \gtrsim 0$. Specifically, for $0 < \mu, |x_0| \ll 1$ deviations away from the original periodic trajectory grow linearly with n , for sufficiently small n.

The purpose here is to investigate the nonsmooth fold associated with a grazing bifurcation in a vibro-impacting mechanical system for use in limit-switch design [58, 82]. As demonstrated below, this alternative compares favorably with the cyclic-fold bifurcation in terms of the growth rate of deviations away from

the original periodic trajectory, indicating the potential to ensure a quicker switch response. Here, at the critical threshold value, there exists a periodic oscillation of an internal element of the device that achieves zero-relative-velocity (grazing) contact with a rigid obstacle at some phase of the oscillation. Computable conditions distinguish between the case in which a steady-state attractor persists in the neighborhood of the grazing periodic oscillation for nearby parameter values and the case of interest here, in which the disappearance of a local attractor results in a rapid transition to a distinctly different steady-state behavior. Indeed, as shown using the theory of discontinuity mappings [15, 52] and rederived here in terms of successive values of the relative velocity at impact, the growth rate of deviations away from the grazing oscillation increases beyond all bounds as the threshold parameter value is approached.

The chapter is organized as follows. Section 4.2 describes an experimental setup used to explore the near-grazing dynamics and, specifically, the growth of relative velocity at successive impacts. An approximate map describing the relationship between successive values of the relative impact velocity is rigorously derived and validated against numerical simulations in Section 4.3. Section 4.4 reports on collected experimental data and compares the observed behavior to the theoretical predictions. Finally, the chapter concludes with a discussion summarizing key findings.

4.2 Phenomenology

4.2.1 Experimental apparatus

An experimental impacting mechanical system, shown schematically in Fig. 4.1, was chosen to investigate the transient dynamics following the onset of low-velocity impacts (cf. [7, 19, 23, 43, 57, 61]). The system consists of a spherical steel ball attached to the end of a cantilevered beam. The ball and beam assembly is in turn clamped to a support and oriented as shown in Fig. 4.1 with the ball resting in front of the head of a Brüel and Kjær Type 4809 electromagnetic shaker. When the shaker is excited (a signal generator and a Brüel and Kjær Type 2706 power amplifier were used), the head moves relative to the body, which is stationary relative to the support. With sufficient excitation amplitude, the head of the shaker will impact the ball resulting in the behavior of interest.

A Polytec PDV100 laser vibrometer was used to gather velocity data. The laser was mounted on a tripod and aimed axially with the motion of the ball. The laser beam was passed through small holes in the support so as to reflect off the objects of interest on the other side (the head and ball), as shown in Fig. 3.1. Signal generation, data acquisition, and signal processing were performed using a Spectral Dynamics SigLab Model 20-42 Dynamic Signal Analyzer and SigLab software (running in Matlab). For further discussion regarding

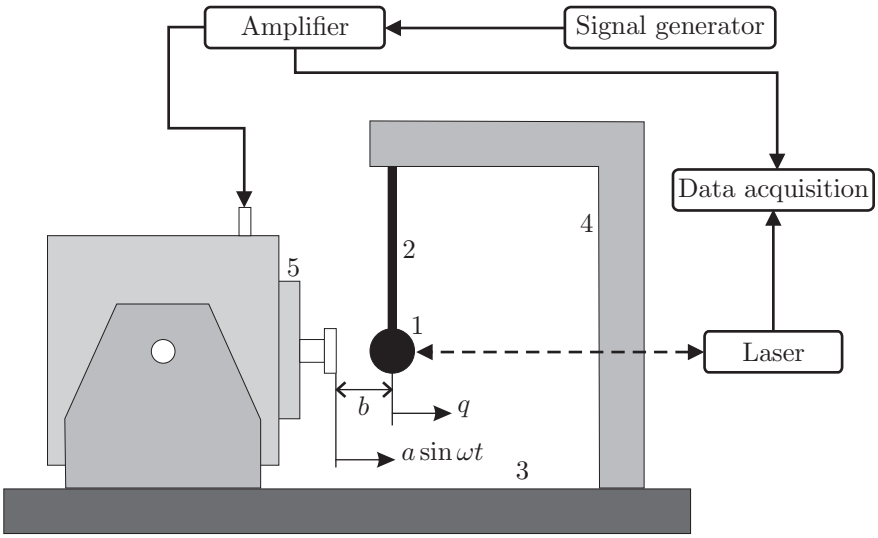

Figure 4.1: Schematic of the experimental apparatus used for investigating near-grazing transient dynamics. The system consists of a spherical steel ball (1) attached to the end of a cantilevered beam (2), clamped to a base (3) through a rigid support (4), and oriented such that the ball rests in front of the head of an electromagnetic shaker (5).

the experimental apparatus, see [18].

4.2.2 Experimental procedure and data processing

To investigate the transient behavior experimentally, a sinusoidal signal was generated using the Virtual Function Generator (VFG) supplied with SigLab. The output from the VFG was routed into an amplifier, then from the amplifier to the inputs of the shaker, again shown schematically in Fig. 4.1. The shaker was started from rest and the gain of the amplifier increased manually until the amplitude of the shaker oscillations brought the head of the shaker close to the ball.

To get as close as possible to grazing contact, the input signal was then incremented quasi-statically using the digital controls within SigLab until impacting behavior was observed. The amplitude of the increments was the minimal amount possible within SigLab, corresponding to approximately 0.26% of the full-scale input. Subsequent to the onset of impacts, data was sampled at 12.8 kHz for approximately 30 cycles of the excitation. A characteristic time evolution is shown in Fig. 4.2(b) and demonstrates the anticipated dramatic growth of the ball velocity over time.

4.2.3 Mathematical model

Consider, for simplicity, a lumped parameter model of the experimental apparatus in which the ball and beam assembly is represented by a massive particle constrained to straight-line motion and affected by a

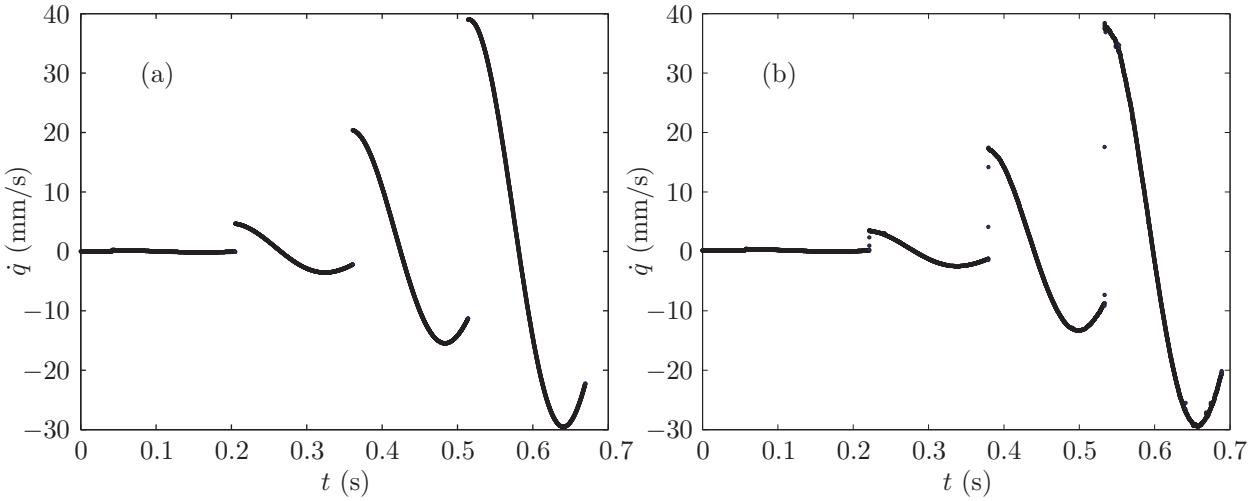

Figure 4.2: Characteristic time evolutions for the ball velocity subsequent to the onset of impacts. (a) numerical simulation; (b) experiment.

linear restoring force and damping. Specifically, let q be the displacement of the particle away from its equilibrium position and suppose that $-b + a \sin \omega t$, where $a, b, \omega > 0$, represents the displacement of the shaker head relative to the particle's equilibrium position.

Let

$$\mathbf{x} = \begin{pmatrix} q & \dot{q} & \theta = \omega t \mathrm{mod} 2\pi \end{pmatrix}^T \tag{4.2}$$

denote the state of the corresponding hybrid dynamical system with continuous dynamics governed by the smooth vector field

$$\mathbf{f}(\mathbf{x}) = \begin{pmatrix} \dot{q} & -2\zeta\omega_n \dot{q} - \omega_n^2 q & \omega \end{pmatrix}^T \tag{4.3}$$

as long as

$$h_{\mathrm{impact}}(\mathbf{x}) \stackrel{\mathrm{def}}{=} q + b - a \sin\theta \geq 0, \tag{4.4}$$

and discrete jumps given by

$$\mathbf{x} \longmapsto \mathbf{g}(\mathbf{x}) = \begin{pmatrix} q & -e\dot{q} + (1+e)\, a\omega \cos\theta & \theta \end{pmatrix}^T \tag{4.5}$$

triggered by transversal crossings of the zero-level surface of h_{impact}. Here, ζ is the damping factor, ω_n is the natural frequency of the system, and e represents a coefficient of restitution. In particular,

$$h_{\mathrm{turning}}(\mathbf{x}) \stackrel{\mathrm{def}}{=} \partial_{\mathbf{x}} h_{\mathrm{impact}}(\mathbf{x}) \cdot \mathbf{f}(\mathbf{x}) = \dot{q} - a\omega \cos\theta \tag{4.6}$$

denotes the rate of change of h_{impact} along trajectories of the smooth vector field, i.e., the relative velocity between the particle and shaker. From the expression for $\mathbf{g}$ it follows that

$$h_{\text{turning}}(\mathbf{g}(\mathbf{x})) = -e h_{\text{turning}}(\mathbf{x}) \tag{4.7}$$

and thus that trajectories that reach $h_{\text{impact}} = 0$ at *incoming points* with $h_{\text{turning}} < 0$ are connected to trajectories based at *outgoing points* on $h_{\text{impact}} = 0$ with $h_{\text{turning}} > 0$.

4.2.4 Numerical simulations

A free vibration test of the ball and beam assembly was completed to characterize the damping factor ζ and natural frequency ω_n . The ball was given an initial displacement and released from rest. The transient dynamics of the system were then captured as the system settled to equilibrium. From experimental data averaged over 10 runs and using the method of logarithmic decrement, ζ was estimated at 0.0881 and ω_n was estimated at 25.2 rad/s.

As the collected data was limited to the absolute velocity of the ball, it was necessary to rely on indirect methods for determining a suitable numerical estimate of the coefficient of restitution e. Specifically, e was estimated at 0.55 so as to result in close agreement between the resultant simulated velocity data (shown in Fig. 4.2(a)) and the experimental data (shown in Fig. 4.2(b)).

4.3 Theoretical analysis

4.3.1 Near-grazing dynamics

As long as $a \leq b$,

$$\mathbf{x}(t) = \begin{pmatrix} 0 & 0 & \omega t \bmod 2\pi \end{pmatrix}^T \tag{4.8}$$

describes a smooth periodic trajectory of the hybrid dynamical system. In particular, for $a = a^* \stackrel{\text{def}}{=} b$ a simple tangential (*grazing*) contact occurs between this trajectory and $h_{\text{impact}} = 0$ at

$$\mathbf{x}^* = \begin{pmatrix} 0 & 0 & \frac{\pi}{2} \end{pmatrix}^T. \tag{4.9}$$

In particular, $h_{\text{turning}}(\mathbf{x}^*) = 0$. Of interest in the subsequent analysis is the dynamics of nearby initial conditions for $a \approx a^*$.

Specifically, let $a - a^* = \varepsilon\delta a$ and consider the initial condition

$$\mathbf{x}_0 = \mathbf{x}^* + \varepsilon \begin{pmatrix} \delta a & \delta\dot{q} & \frac{\delta h_{\text{turning}} - \delta\dot{q}}{b\omega} \end{pmatrix}^T + \mathcal{O}\left(\varepsilon^2\right) \tag{4.10}$$

such that $h_{\text{impact}}\left(\mathbf{x}_0\right) = \mathcal{O}\left(\varepsilon^2\right)$ and $h_{\text{turning}}\left(\mathbf{x}_0\right) = \varepsilon\delta h_{\text{turning}} + \mathcal{O}\left(\varepsilon^2\right)$, where $\delta h_{\text{turning}} < 0$ (cf. Fig. 4.3). It follows that

$$\mathbf{x}_1 = \mathbf{g}\left(\mathbf{x}_0\right) = \mathbf{x}^* + \varepsilon \begin{pmatrix} \delta a & \delta\dot{q} - (1+e)\,\delta h_{\text{turning}} & \frac{\delta h_{\text{turning}} - \delta\dot{q}}{b\omega} \end{pmatrix}^T + \mathcal{O}\left(\varepsilon^2\right) \tag{4.11}$$

such that $h_{\text{impact}}\left(\mathbf{x}_1\right) = \mathcal{O}\left(\varepsilon^2\right)$ and $h_{\text{turning}}\left(\mathbf{x}_1\right) = -\varepsilon e\delta h_{\text{turning}} + \mathcal{O}\left(\varepsilon^2\right)$.

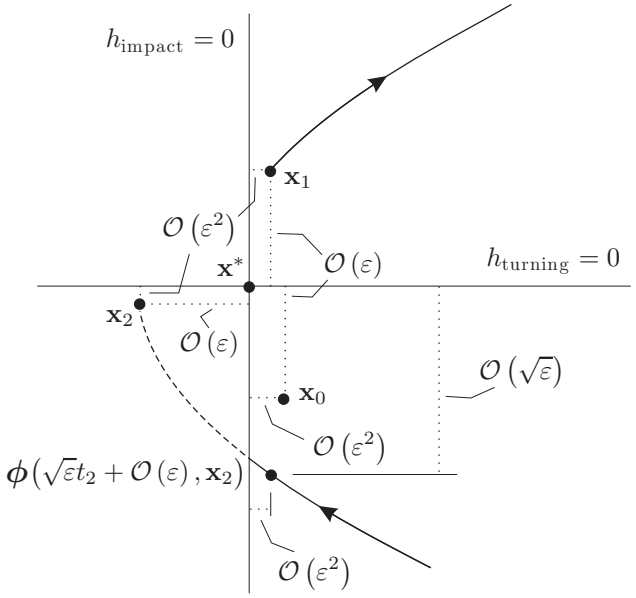

Figure 4.3: Schematic illustrating the sequence of points introduced in the derivation of Eqn. (4.24) and the growth in order in ε of the value of h_{turning} at successive impacts.

In the case that $\zeta < 1$, the smooth flow corresponding to the vector field $\mathbf{f}$ is given by

$$\boldsymbol{\phi}\left(t, \tilde{\mathbf{x}}\right) = \begin{pmatrix} \frac{e^{-t\zeta\omega_n}}{\Omega}\left(\tilde{q}\Omega\cos\Omega t + \left(\dot{\tilde{q}} + \tilde{q}\zeta\omega_n\right)\sin\Omega t\right) \\ \frac{e^{-t\zeta\omega_n}}{\Omega}\left(\dot{\tilde{q}}\Omega\cos\Omega t - \omega_n\left(\dot{\tilde{q}}\zeta + \tilde{q}\omega_n\right)\sin\Omega t\right) \\ \tilde{\theta} + \omega t \end{pmatrix}, \tag{4.12}$$

where $\Omega = \omega_n\sqrt{1-\zeta^2}$. In particular, with

$$t_1 \stackrel{\text{def}}{=} \frac{1}{b\omega^2}\left(\delta\dot{q} - \delta h_{\text{turning}} - \frac{e^{-2n\pi\zeta\omega_n/\omega}}{\Omega}\begin{pmatrix}\left(\delta\dot{q} - (1+e)\,\delta h_{\text{turning}}\right)\Omega\cos\frac{2n\pi\Omega}{\omega}\\ -\omega_n\left(\omega_n\delta a + \delta\dot{q}\zeta - (1+e)\,\zeta\delta h_{\text{turning}}\right)\sin\frac{2n\pi\Omega}{\omega}\end{pmatrix}\right) \tag{4.13}$$

for some positive integer n, it follows that

$$h_{\text{turning}}\left(\boldsymbol{\phi}\left(\frac{2n\pi}{\omega} + \varepsilon t_1 + \mathcal{O}\left(\varepsilon^2\right), \mathbf{x}_1\right)\right) = \mathcal{O}\left(\varepsilon^2\right) \tag{4.14}$$

and

$$h_{\text{impact}}\left(\boldsymbol{\phi}\left(\frac{2n\pi}{\omega} + \varepsilon t_1 + \mathcal{O}\left(\varepsilon^2\right), \mathbf{x}_1\right)\right) = \delta h_{\text{impact}}\varepsilon + \mathcal{O}\left(\varepsilon^2\right), \tag{4.15}$$

where

$$\delta h_{\text{impact}} = -\delta a + \frac{e^{-2n\pi\zeta\omega_n/\omega}}{\Omega}\begin{pmatrix}\Omega\delta a\cos\frac{2n\pi\Omega}{\omega}\\ +\left(\omega_n\zeta\delta a + \delta\dot{q} - (1+e)\,\delta h_{\text{turning}}\right)\sin\frac{2n\pi\Omega}{\omega}\end{pmatrix}. \tag{4.16}$$

Let n be the smallest integer[1] such that δh_{impact} is negative and set

$$\mathbf{x}_2 = \boldsymbol{\phi}\left(\frac{2n\pi}{\omega} + \varepsilon t_1 + \mathcal{O}\left(\varepsilon^2\right), \mathbf{x}_1\right). \tag{4.17}$$

It follows that a transversal crossing of h_{impact} must have occurred prior to the trajectory reaching $\mathbf{x}_2$. In particular, with

$$t_2 \stackrel{\text{def}}{=} -\sqrt{-\frac{2\delta h_{\text{impact}}}{b\omega^2}} \tag{4.18}$$

it follows that

$$h_{\text{impact}}\left(\boldsymbol{\phi}\left(\sqrt{\varepsilon}t_2 + \mathcal{O}\left(\varepsilon\right), \mathbf{x}_2\right)\right) = \mathcal{O}\left(\varepsilon^2\right) \tag{4.19}$$

and

$$h_{\text{turning}}\left(\boldsymbol{\phi}\left(\sqrt{\varepsilon}t_2 + \mathcal{O}\left(\varepsilon\right), \mathbf{x}_2\right)\right) = -\sqrt{-2b\omega^2\delta h_{\text{impact}}}\sqrt{\varepsilon} + \mathcal{O}\left(\varepsilon\right), \tag{4.20}$$

whereas

$$\dot{\phi}_2\left(\sqrt{\varepsilon}t_2 + \mathcal{O}\left(\varepsilon\right), \mathbf{x}_2\right) = \mathcal{O}\left(\varepsilon\right) \tag{4.21}$$

corresponding to the value of absolute velocity, $\dot{q}$, at this location (see Fig. 4.3).

The above analysis demonstrates that for sufficiently small ε, repeated iterations of the three steps described above yield a value of h_{turning} that eventually deviates from 0 by $\mathcal{O}\left(\sqrt{\varepsilon}\right)$ while $\delta\dot{q}$ remains $\mathcal{O}\left(\varepsilon\right)$.

[1] Such an integer is guaranteed to exist in the underdamped case $\zeta < 1$.

It follows that δa and $\delta\dot{q}$ terms in the expression for δh_{impact} may eventually be ignored yielding

$$\delta h_{\text{impact}} = -(1+e)\,\delta h_{\text{turning}} \frac{e^{-2n\pi\zeta\omega_n/\omega}}{\Omega} \sin\frac{2n\pi\Omega}{\omega} \tag{4.22}$$

and the map

$$\delta h_{\text{turning}} \longmapsto -\sqrt{2b\omega^2\,(1+e)\,\delta h_{\text{turning}} \frac{e^{-2n\pi\zeta\omega_n/\omega}}{\Omega} \sin\frac{2n\pi\Omega}{\omega}} \tag{4.23}$$

from one impact to the next, where n is the smallest integer that guarantees that the argument of the radical is positive.

From Eqn. (4.5), it follows that the jump $\Delta\dot{q}$ in absolute velocity due to impacts is proportional with coefficient $-(1+e)$ to the relative velocity $\delta h_{\text{turning}}$ at impact, thus yielding the map

$$\Delta\dot{q} \longmapsto c\,(e,\omega,b,\omega_n,\zeta)\,\sqrt{\Delta\dot{q}}, \tag{4.24}$$

where

$$c\,(e,\omega,b,\omega_n,\zeta) = \omega\,(1+e)\,\sqrt{-2b\frac{e^{-2n\pi\zeta\omega_n/\omega}}{\Omega} \sin\frac{2n\pi\Omega}{\omega}}. \tag{4.25}$$

4.3.2 Numerical results

To validate the approximations made in the derivation of the discrete map, Eqn. (4.24), a series of numerical experiments were performed in which data for several successive low-velocity impacts were collected and the value of $\Delta\dot{q}$ at one impact was graphed against the value at the previous impact. The Matlab code used to execute these simulations is shown in Appendix A. Specifically, simulations were performed with the numerical values of ζ, ω_n, and e previously estimated, with $b = 0.65$ mm, and $f = \frac{\omega}{2\pi} = 6$, 10, 14, 18, and 22 Hz. For each set of parameter values, a large number of runs were performed with random initial conditions near $\mathbf{x} = \mathbf{0}$ and with a range of values of a near b. For each run, data was collected for successive impacts as long as $\Delta\dot{q}$ did not exceed 50 mm/s.

Figure 4.4 shows a log-log plot of the collected data for the five different excitation frequencies. In each case, a linear regression fit was performed on the all data with $\Delta\dot{q} \in (0.01, 1)$ mm/s. The corresponding values of the slope and intercept are shown in tabular form in Table 4.1. The table further contains predicted values for the slope and intercept (i.e., $\log c\,(e,\omega,b,\omega_n,\zeta)$) as obtained from Eqn. (4.24) and Eqn. (4.25). The results confirm the validity of the discrete map in predicting the near-grazing transient dynamics.

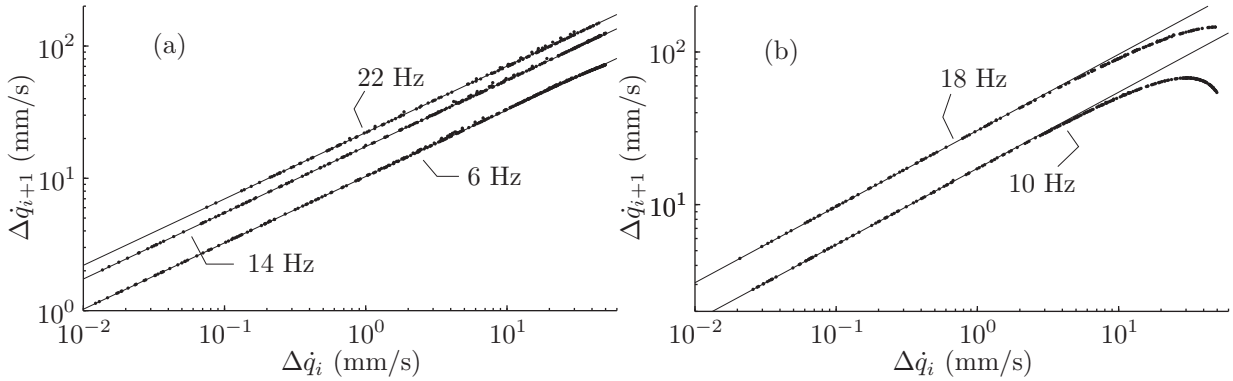

Figure 4.4: Numerically simulated $\Delta\dot{q}_{i+1}$ vs. $\Delta\dot{q}_i$ at successive impacts for $\Delta\dot{q} \leq 50$ mm/s. Here, straight lines represent linear regression fits performed in the log-log representation using $\Delta\dot{q}_i \in (0.01, 1)$ mm/s corresponding to 77 points for $f = 6$ Hz, 67 points for $f = 10$ Hz, 63 points for $f = 14$ Hz, 57 points for $f = 18$ Hz, and 35 points for $f = 22$ Hz.

	Numerical Results		Mapping Results	
$\omega/2\pi$ (Hz)	Slope	Intercept	Slope	Intercept
6	0.5015	1.0140	0.5	1.0116
10	0.4990	1.2373	0.5	1.2387
14	0.5005	1.2404	0.5	1.2396
18	0.4986	1.4869	0.5	1.4887
22	0.5017	1.3456	0.5	1.3441

Table 4.1: Comparison of slope and intercept describing the linear fit shown in Fig. 4.4 and predicted values obtained using Eqns. (4.24-4.25) with $b = 0.65$. Here, $n = 1$ when $\omega = 12\pi$, $n = 2$ when $\omega = 20\pi$ and 28π, and $n = 3$ when $\omega = 36\pi$ and 44π.

4.4 Experimental results

Experiments were performed following the protocol described in Section 4.2.2 and data was collected and processed in the same manner as described in Section 4.3.2 with the proviso that for each excitation frequency, the value of b was adjusted to maintain the excitation voltage within an allowable range.

Figure 4.5 shows a log-log plot of the collected data for the five different excitation frequencies. In each case, the behavior predicted from Eqn. (4.24) is represented by the included straight lines (where $b = 0.65$ for $f = 6$ Hz and 14 Hz, $b = 0.67$ for $f = 10$ Hz, $b = 0.59$ for $f = 18$ Hz, and $b = 0.54$ for $f = 22$ Hz). The results again confirm the validity of the discrete map in predicting the near-grazing transient dynamics (although a noticeable discrepancy is noticed in the intercept in the case that $f = 22$ Hz). Indeed, the experimental data conforms with the predicted value of the integer n, i.e., the smallest integer that guarantees that the argument of the radical in Eqn. (4.25) is positive.

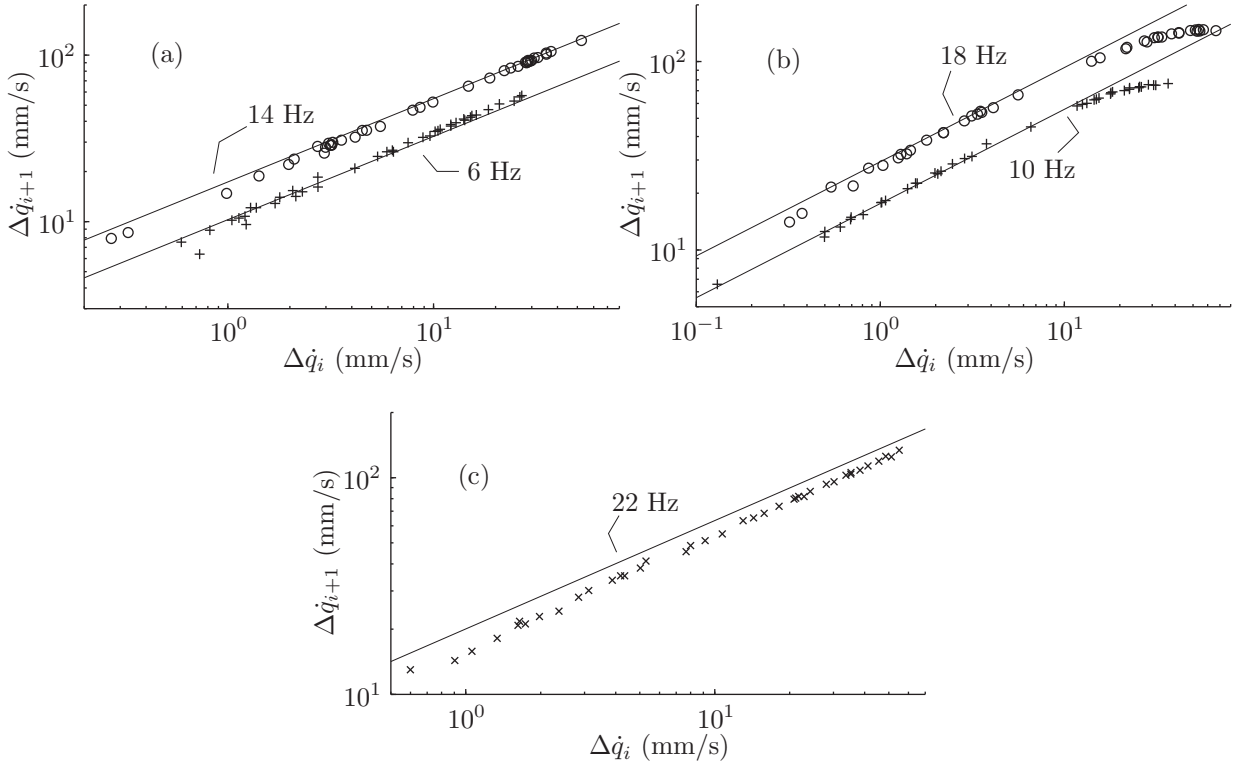

Figure 4.5: Experimentally measured values of $\Delta\dot{q}_{i+1}$ vs. $\Delta\dot{q}_i$ collected for three successive impacts. Here, straight lines represent predicted relationship as obtained from Eqn. (4.24).

It was observed that the limitations imposed by the measurement hardware and the method for extracting jumps in the absolute velocity made it difficult to collect accurate data for extremely low-relative-velocity impacts (cf. the leftmost impact in Fig. 4.6). Indeed, while the discontinuity in the data is still somewhat

apparent, the nature of the discontinuity is not as abrupt as in the case of the latter impacts shown in Fig. 4.6. For this reason, a lower limit was imposed on the values of $\Delta\dot{q}$ included in the analysis.

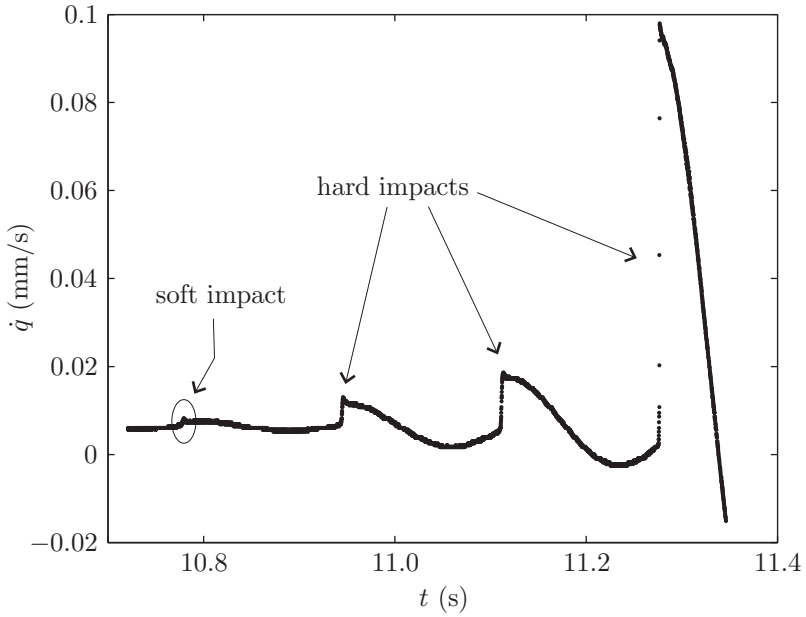

Figure 4.6: "Soft" impacts with $\Delta\dot{q}$ below the discernible limit were not included in the processed data.

4.5 Discussion

The experimental, analytical, and numerical results presented here demonstrate clearly the near-grazing transient behavior that supports the proposed reliance on the nonsmooth fold bifurcation in vibro-impacting systems as the operating principle of a novel class of limit switches. In particular, the increase beyond all bounds of the transient growth rate of near-grazing impact velocities as the threshold parameter value is approached suggests a high sensitivity and rapid switching speed of a corresponding limit switch. In contrast, for limit switches that rely on saddle-node bifurcations of equilibria or smooth cyclic-fold bifurcations of periodic oscillations, the corresponding growth rate would fall off to zero as the threshold value was approached.

Recent work on the control of near-grazing dynamics in vibro-impacting systems suggest a mechanism for regulating the limit switch response [13, 14]. With the inclusion of additional feedback, the nonsmooth fold bifurcation associated with near-grazing dynamics can be replaced with the persistence scenario in which a steady-state attractor persists in the vicinity of the threshold parameter value. Such a regulator would enable the inclusion of a secondary fail-safe mechanism that would first need to be triggered in order to enable the limit switch. This would enhance the ability to adjust the sensitivity of the switch to noise and

is a suggested topic for further study.

Although other investigators have explored the near-grazing dynamics of vibro-impact oscillators, previous work has primarily focused on the form of steady-state attractors and not on the transient behavior following the initial onset of low-relative-velocity impacts [7, 19, 23, 43, 57, 59, 61]. As the emphasis here has been on the immediate response of a limit switch following the crossing of the threshold value, only transient results have been included in the analysis. The study of the steady-state behaviors to which the internal state of the switch would be attracted following the initial transient would provide insight into the overall switch design. The following chapter addresses these questions, as well as suggesting a means by which the switch in state might be intrinsically detected via the electrical signals in a coupled electromechanical system.

Chapter 5

A Discontinuity-Enabled Sensing and Actuation Testbed

5.1 Introduction

As alluded to in the introductory chapter, microelectromechanical systems have of late become a popular choice for sensor and actuator device designs, due to a number of favorable characteristics affecting their fabrication and deployment, including size and power requirements [45]. As these devices feature inherent coupling, for example between mechanical and electrical energy domains, they may be purposefully designed to take advantage of integrated transduction mechanisms for simultaneous actuation and sensing. For example, excitation of the electrical degrees of freedom may be transduced to excite the mechanical elements of such a device. At the same time, difficult-to-observe phenomena in the mechanical degrees of freedom may manifest themselves in measurable dynamics in the electrical elements.

With miniaturization and multiple interacting physical domains comes the potential of significant influence of nonlinearities, for example due to large mechanical deflections or electrostatic actuation. Such nonlinearities offer novel opportunities for enhanced functionality across wider parameter ranges than their linear counterparts. While challenging to analyze and often eliminated through overly conservative designs, the purposeful introduction of nonlinearities may desensitize device designs to parameter uncertainty and/or dramatically improve sensor gains.

The strongly nonlinear phenomenon of intermittent contact and, in particular, the dramatic changes in dynamic response of mechanical systems at the onset of impulsive contact have been proposed in the previous chapters as a fundamental operating principle for a high-gain sensor. Similar transitions in non-impacting systems have been proposed in the design of microelectromechanical mass sensors [67, 78, 79], there relying on nonlinearities associated with parametric excitation.

In light of these observations, it is of interest to explore the possibility of a microelectromechanical implementation of the above-mentioned operating principle, relying on discontinuous transitions in the mechanical response, excited by the electrical system and induced by the onset of contact, and transducing this response into directly observable changes in the electrical characteristics of the device. The relatively short transients

combined with the high natural frequencies of the micromechanical system suggest that a sensor designed according to these principles would exhibit an ultrafast response.

There are, however, significant challenges with pursuing such microdevice designs at an initial exploratory stage, primarily associated with fabrication and testing [45]. A compromise, therefore, is to explore device designs at millimeter scale that retain some of the essential characteristics of the microscale devices, primarily the multidomain coupling and impact-induced transitions, while enabling repeated experimentation at a reasonable expense in money and time.

To this end, the discussion in this chapter details the design, construction, experimental investigation, theoretical modeling, and numerical exploration of a macroscale device, which includes the possibility of recurrent mechanical contact and exploitable signal transduction between the mechanical and electrical degrees of freedom. It is not the primary goal to document the presence of particular classes of changes in steady-state system response associated with the onset of mechanical contact, as this has been well documented in the existing literature [12, 15, 19, 21, 24, 23, 50, 57, 59, 61, 66, 64, 81]. Nor is it the goal to establish the rapidity of the transient dynamics immediately following the onset of contact, since this was just established in the preceding chapter. Rather, the goal is to illustrate the use of inductive coupling between the mechanical and electrical degrees of freedom to actuate the mechanical system and transduce the changes in the mechanical response due to the onset of contact into a measurable change in the oscillatory behavior of the device current.

In particular, it is desireable to show that changes in the dynamical behavior that originate in the mechanical system can be detected in the coupled response of the electrical system used to actuate the device. This is clearly important to enable a useful sensor design [22]. If changes in these dynamics are to be relied upon as an indicator mechanism in a sensor, it is desirable to be able to detect those changes without large, expensive, and complicated data acquisition equipment or an excessive number of additional stages of transduction. Usually this information should be available via an electrical signal which is conducive to processing using integrated circuits and/or digital computers. As an example, while changes in the mechanical response typically will result in changes in the amplitude content of the current signal, it may be more desirable to design the device so as to have the onset of contact result in observable changes in the signal's frequency content.

The remainder of the chapter is organized as follows. Section 5.2 outlines the principal design elements introduced in the device in order to support the desired multidomain coupling and contact-related dynamics. This is followed by a detailed discussion of the device construction and experimental setup used to produce the experimental data reported in this section. A periodically excited three-dimensional mathematical model

of the coupled electromagnetic and mechanical systems is developed in Section 5.3. This section further presents a system-identification procedure used to associate numerical values with model parameters and simulation results obtained with these values under numerical experiments designed to mimic the physical experiments. A concluding discussion in Section 5.4 highlights some particularly interesting features of the steady-state response on a neighborhood of the parameter values associated with the onset of contact, including such changes in the frequency response of the electrical current mentioned previously.

5.2 Experimental testbed

5.2.1 Device design

As outlined in the introduction, two fundamental objectives form the basis for the device design. First, the device should allow for intermittent contact between an oscillatory mechanical element and a fixed obstacle. As per the extensive literature on the topic of vibro-impact oscillators, such contact and, in particular, its onset under parameter variations, is known to be associated with strong nonlinearities and sudden and dramatic bifurcations in system response. Second, the device should allow for the transduction of the mechanical response to a coupled electrical system and vice versa. This affords a mechanism for actuating the mechanical system while simultaneously detecting changes in the dynamics of the mechanical system through observation of the electrical response.

Clearly, the possibility of mechanical contact is easily achieved through the introduction in the device geometry of a physical stopper that limits the oscillatory motion of the mechanical element in one direction. This would also likely be the way in which this feature would be introduced in a microscale device, although contact there might be more diffuse and less impulsive.

Several alternatives exist for transduction between the mechanical and electrical domains [22]. For example, the mechanical element could constitute the movable part of a potentiometer, whereby changes in the mechanical displacement would be observed through variations in the resistance in a coupled electrical circuit. Measurements of the circuit current for a given voltage could then be used to estimate the resistance and to back out the mechanical response characteristics. This transduction mechanism is entirely one-way, in that no force is generated on the mechanical system from changes in the electrical circuit, so this coupling can therefore not serve as a means of actuating the mechanical system. Finally, it is far from obvious how an analogous implementation could be developed at the microscale.

A more appealing alternative is to allow the mechanical element to constitute a movable part of a parallel-plate capacitor (a subject taken up in the next chapter), whereby changes in the mechanical displacement

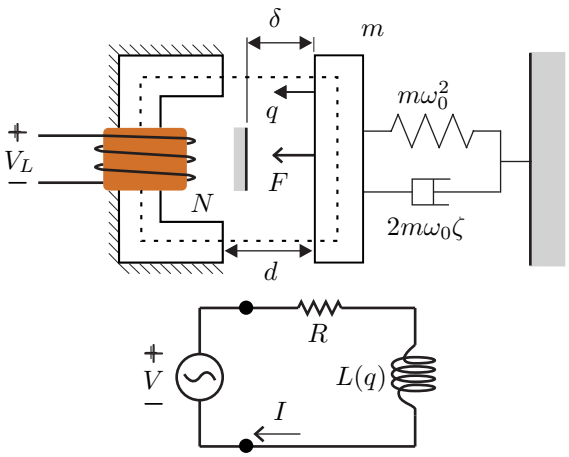

Figure 5.1: Schematic representations of the mechanical and electrical systems. The filled circles in the circuit schematic refer to the input terminals of the actual device.

would be observed through variations in the capacitance in a coupled electrical circuit. Here, again, measurements of the circuit response to given voltage variations could be used to estimate the capacitance and to back out the mechanical response characteristics. In contrast to the resistive design, this transduction mechanism is two-way, in that a force acting on the mechanical element results from a circuit voltage. This coupling can therefore serve as a means of actuating the mechanical system while allowing the state of the system to be interrogated through the circuit response. Capacitive sensing and actuation is straightforward to realize at the microscale, but the actuation property scales poorly in the macroscale, where other forces dominate.

Consider, instead, the possibility of allowing the mechanical element to constitute a movable part of an electromagnetic circuit, whereby changes in the mechanical displacement would be observed through variations in the circuit inductance. Analogously to the capacitive design, this transduction mechanism is two-way, in that the circuit flux depends on the mechanical displacement while inducing a mechanical force on the movable element. This coupling can therefore serve the dual objective of actuation and sensing. Moreover, the force applied to the mechanical element resembles that obtained in the capacitive case, in that it is proportional to the square of a circuit quantity, namely the current (voltage in the case of the parallel-plate capacitor), and inversely proportional to the square of a separation distance (the plate gap in the case of the capacitor). Finally, inductive sensing and actuation is straightforward to realize at the macroscale, but scales poorly in the microscale where electrostatic interactions dominate.

A schematic of a testbed relying on the inductive transduction mechanism and explored throughout this paper is shown in Fig. 5.1. The device consists of a movable ferromagnetic bar suspended coplanarly and opposite to a U-shaped electromagnet built from a ferromagnetic core with an inductive coil wrapped around

the midpoint. As suggested previously, oscillations of the bar, here constrained to the direction toward and away from the electromagnet, induce variations in the magnetic reluctance (and effective resistance) of the electromagnetic circuit. These, in turn, result in variations in the magnetic flux through the ferromagnetic core and corresponding variations in the coil current, assuming an ideal voltage source. The circuit current, in turn, generates a magnetic flux through the electromagnet which imposes an attractive force (in the direction toward the magnet) on the suspended bar.

5.2.2 An electromagnetically forced vibro-impactor

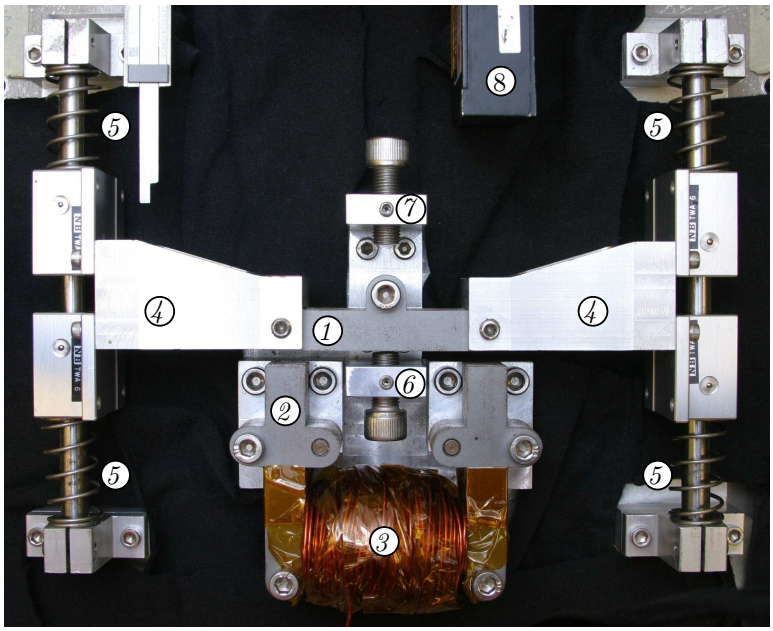

Figure 5.2: Photograph of the experimental testbed. Labeled parts are described in the main text.

A photograph of the experimental apparatus is shown in Fig. 5.2. Key elements of the device have been labeled for clarity. Parts *1* and *2*, which are separated by an air gap, are approximately 2.54 cm thick laminated stacks of 0.356 mm M19 non-oriented electrical steel with C5 core plating. These parts, which have the same cross-sectional area, make up the ferromagnetic cores of the electromagnet. The choice of material was guided by a desire to minimize magnetic hysteresis and eddy current losses in the cores. All parts in close proximity to the ferromagnets were made of aluminum or nonmagnetic stainless steel so as to minimize disturbances to the flux paths within the cores.

Part *2* is securely pinned and bolted to an aluminum baseplate, which is largely obscured by a black cloth used to provide contrast for the photograph. This plate was in turn bolted to a Newport sealed top optical table. Wrapped around part *2* is a 200 turn, hand-wound coil made of 16 AWG copper magnet wire,

labeled *3*. Part *1* is clamped between two aluminum endpieces, marked *4*, on either end of which there is a pair of linear ball bearings which ride on horizontal shafts. Concentric to the shafts are four coil springs, labeled *5*, which suspend the oscillating assembly. The bearings and shafts were precisely machined and adjusted to eliminate any noticeable freeplay. This constrains the motion of part *1* to pure translation in the horizontal plane in a direction parallel to the shafts.

Limiting the linear motion of the oscillating assembly are two independently adjustable stops, labeled *6* and *7*. These stops were either used in tandem to clamp the oscillating mass in place for system identification purposes, as discussed in a later section, or with stop *7* removed and stop *6* adjusted to provide a fixed obstacle in the path of the oscillating assembly with which recurrent impacts could occur.

The velocity response of the oscillating assembly was measured with a Polytec PSV300U laser vibrometer, not shown in the photograph. The displacement response of the oscillating assembly was measured using a NAiS LM200 laser controller with a NAiS ANL2500A laser displacement sensor. The laser displacement sensor is partially visible in the upper part of the photo, labeled *8*.

An Ohmite model L100J1ROE, 1 Ω, 100 W power resistor (represented by R in Fig. 5.1) was connected in series with the coil. By measuring the voltage drop across the power resistor, the current (represented by I in Fig. 5.1) in the circuit can be calculated using Ohm's law. The system was excited by a voltage source (represented by V in Fig. 5.1), not shown in the picture, consisting of an HP33120A digital function generator providing a low power waveform to a Techron 5530 power supply amplifier. The output terminals of the amplifier were connected to the input terminals of the device (shown as two filled circles in the schematic circuit diagram in Fig. 5.1). Voltage signals were measured and acquired using a National Instruments USB-6211 data acquisition board with twisted-pair wiring connecting all terminals. Data was recorded either with National Instruments SignalExpress software or using Matlab with the Data Acquisition Toolbox. The HP33120A was either controlled manually or through the RS232 serial interface using the Instrument Control Toolbox in Matlab. The applied voltage was measured at the input terminals of the device, across the series connected coil and power resistor. Typical input voltage amplitudes ranged from $\approx 2 - 8$ V with current response on the order of one to several Amps, so as to generate a sufficient attractive force on the suspended oscillating assembly.

5.2.3 Experimental results

To generate the experimental data reported below, the digital function generator was set to produce a harmonic, low-power signal which was subsequently amplified by the power supply to provide a sinusoidal voltage across the input terminals of the device. The displacement, velocity, and electric current time

histories were acquired simultaneously along with the input voltage. Sampled phase section data was then extracted through post-processing of the acquired time histories. To generate the experimental bifurcation diagrams, the process of setting the inputs, letting the system settle, and acquiring the time history of the system variables was automated using a Matlab script and the RS232 interface to the function generator. The script is shown as `DENSAT_acquire_swpV.m` in Appendix B, along with other scripts used to process the experimental data. Each sweep was accomplished by fixing the input frequency and successively incrementing the amplitude of the generated signal from low to high and back to low in very small steps. For each amplitude, the system was allowed to settle for 20 s and data was then acquired for ≈ 10 s at a sampling rate of 1 kHz. A sample time evolution of the system is shown in Fig. 5.3. This procedure was repeated for each frequency investigated. In all the cases reported here, the equilibrium gap distance between the oscillating assembly and the ferromagnetic core was set at 4.79 mm and the equilibrium separation between the oscillating assembly and the stopper was set at 1.11 mm.

Each point in the bifurcations diagrams below corresponds to a sampled value of the velocity or current plotted against the average input voltage amplitude V_0 across the entire 10 s acquisition time. Specifically, phase section data was collected at zero-crossings of the oscillating input voltage. Data corresponding to zero-crossings in the increasing direction are shown as blue dots in the figures below. To accommodate an anticipated symmetry in the system response (see discussion in Sec. **??**), data corresponding to zero-crossings in the decreasing direction, shown as red dots, are also included in the same diagrams after negating the sign on the current values. Consequently, for each input amplitude, the bifurcation diagrams include two points per period of excitation. In the event that these two points coincide, the response is said to be symmetric.

Figures 5.4-5.6 below show some typical sweeps of the input amplitude at excitation frequencies below and above mechanical resonance ($f \approx 15$ Hz), bearing in mind that the mechanical forcing originating in the magnetic field is proportional to the squared current. Specifically, Fig. 5.4 shows the experimental bifurcation diagram obtained when sweeping the amplitude of the signal generator voltage at an excitation frequency of $f = 6.1$ Hz. Panels (a) and (c) show the sampled velocities for each period of excitation when increasing the voltage amplitude (a) and decreasing the voltage amplitude (c). Starting with a symmetric periodic orbit for low input amplitude, the onset of low-velocity contact is induced at an input amplitude near 5 V, after which the system settles onto a noisy, apparently period-three, nonsymmetric attractor. The figure clearly illustrates the hysteretic nature of the response about the point of onset of contact, as this period-three attractor persists far below the initial parameter value associated with the onset of contact. Panels (b) and (d) show the corresponding sampled currents for each period of excitation, again for increasing (b) and decreasing (d) values of the input voltage amplitude. Although the change in frequency characteristics

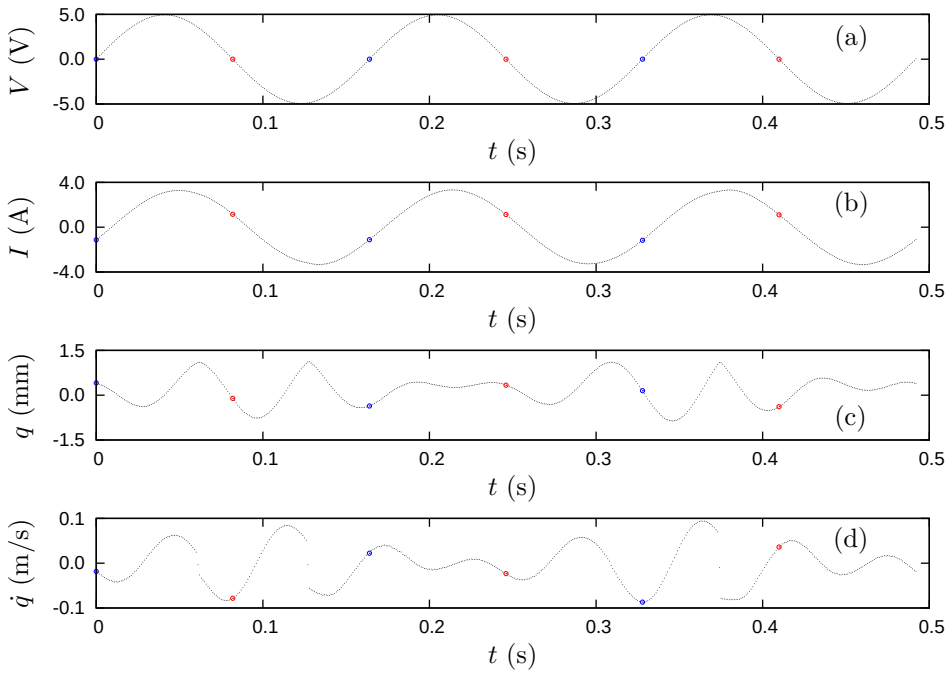

Figure 5.3: Experimental time evolution of the system over three periods of the input for $f = 6.1$ Hz. Panel (a) shows the input voltage, panel (b) shows the current response, panel (c) shows the position respon se, and panel (d) shows the velocity response. Here and in all subsequent figures reporting on experimental results, blue circles/dots indicate data taken at zero-crossings of the input voltage as it is rising and red circles/dots indicate data taken at zero-crossings of the input voltage as it is falling.

subsequent to the onset of contact is again visible in the current response, this is somewhat obscured by the greater degree of variability in the current measurements.

A similar bifurcation diagram is shown in Fig. 5.5 for an excitation frequency of $f = 7$ Hz, i.e., still below resonance. Here, the transition following the onset of contact (near 3.6 V) again involves a discontinuous transition from the nonimpacting period-one response to a distinct steady-state attractor, here irregular and apparently chaotic. As seen from a comparison between panels (a) and (c), there again exists a (relatively small) interval of parameter hysteresis. It is also interesting to note the existence of windows of (possibly periodic) attractors of period three (near 4.8 V), period four (near 4.3 V), and possibly period five (near 4 V). Again, due to the noisiness of the current measurements, it is distinctly more difficult to make out the changes in the response in panels (b) and (d). As the attractor is irregular, the frequency content is clearly broadband in this case.

Finally, Fig. 5.6 shows the bifurcation diagram obtained in the case of an excitation frequency of $f = 8$ Hz (above resonance). Here, the response before and after the onset of contact is period-one and symmetric with a significant interval of coexistence of the corresponding steady-state solutions. Although there is thus no change in the frequency content as a result of the onset of contact, panels (b) and (d) show a sudden

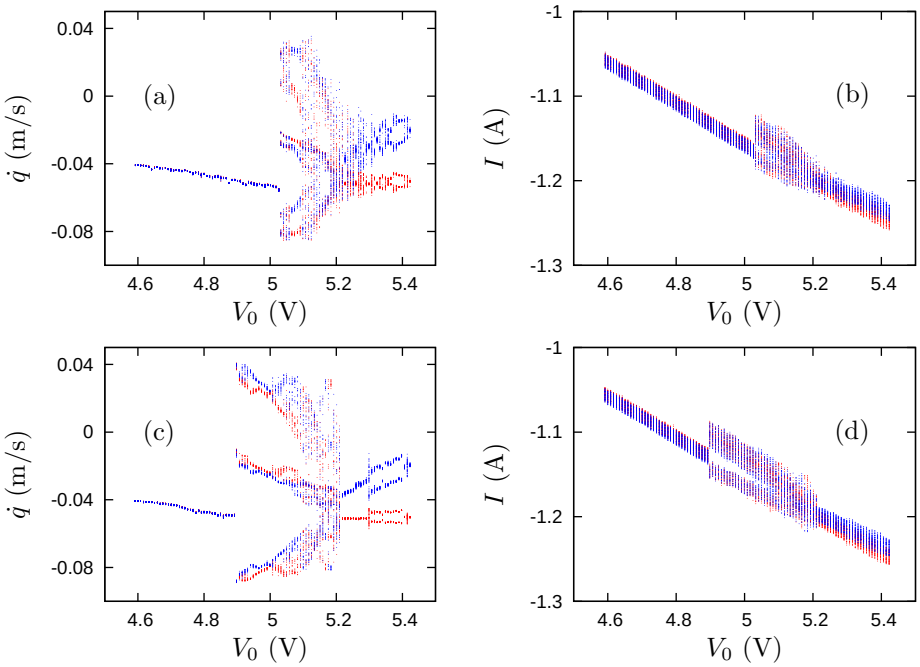

Figure 5.4: Experimental bifurcation diagrams for $f = 6.1$ Hz. Panels (a) and (c) show sampled velocities for sweeps in the up and down directions, respectively. Panels (b) and (d) show sampled electrical current for sweeps in the up and down directions, respectively.

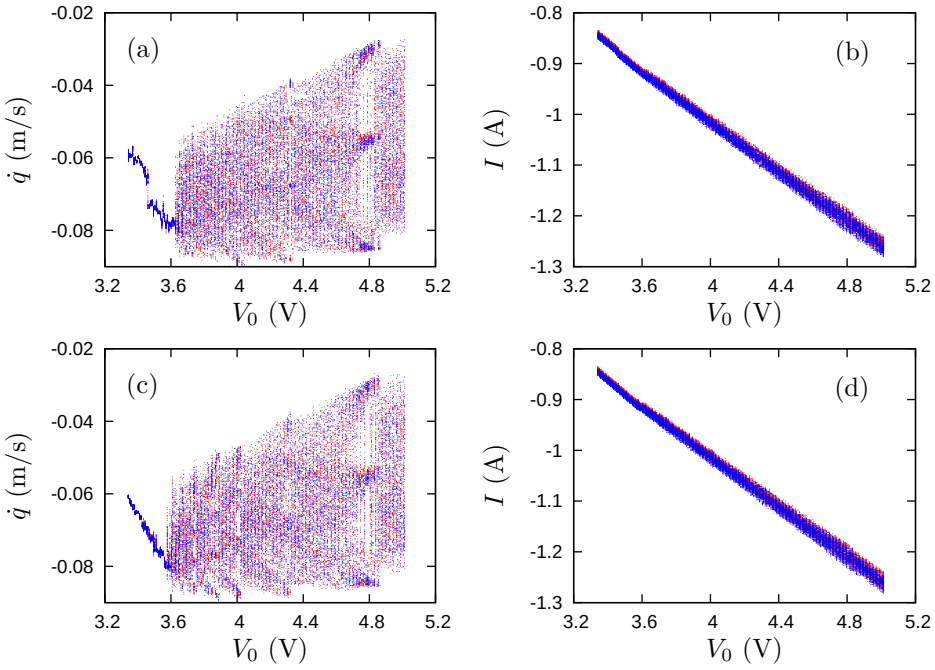

Figure 5.5: Experimental bifurcation diagrams for $f = 7$ Hz. Panels (a) and (c) show sampled velocities for sweeps in the up and down directions, respectively. Panels (b) and (d) show sampled electrical current for sweeps in the up and down directions, respectively.

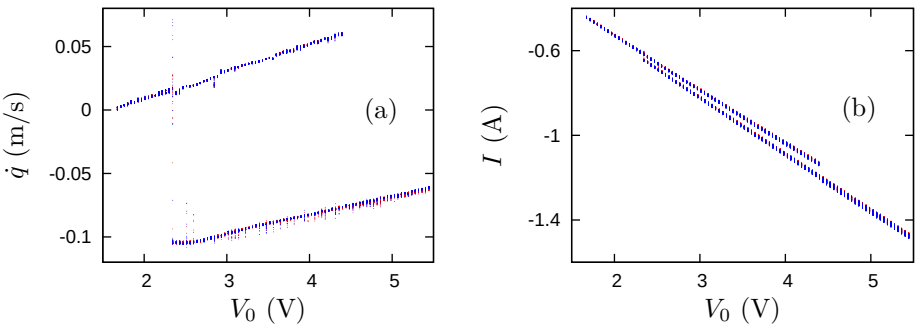

Figure 5.6: Experimental bifurcation diagrams for $f = 8$ Hz. Panels (a) and (b) show sampled velocities and currents, respectively, for sweeps in both the up and down directions.

change in the measured current values.

5.3 Mathematical model

We proceed to derive an approximate dynamical systems model of the coupled electromechanical system, which respects the constrained dynamics of the movable mechanical element corresponding to parts *1* and *4* in Fig. 5.2 and the response of the electromagnetic circuit.

With reference to the schematic in Fig. 5.1, let the oscillating assembly be modeled by a single-degree-of-freedom particle of mass m, connected to the inertial frame through a parallel arrangement of an equivalent linear spring of stiffness $m\omega_0^2$ and linear dashpot with damping coefficient $2m\omega_0^2\zeta$. Here, ω_0 is the natural frequency of the undamped spring-mass system and ζ denotes the damping ratio. Let q, d and δ denote the displacement of the particle relative to its equilibrium position, the equilibrium gap in the electromagnetic circuit, and the equilibrium separation between the particle and the fixed stopper, respectively, in the absence of excitation. Typically, $\delta < d$, from which it follows that $q \leq \delta$.

The electrical system is modeled as consisting of an ideal voltage source $V(t)$, where t is time, a linear effective resistance, R, a displacement dependent inductance, $L(q)$, with the current flowing in the circuit denoted by I. The coupling fields are assumed to be conservative and field transients are assumed negligible on the time scale of the mechanical oscillator.

In order to arrive at approximate expressions for the inductance $L(q)$ and the magnetically induced force F on the oscillating mass, consider the dotted line in Fig. 5.1 corresponding to the mean flux path. The length of this path is the sum of the mean length l_m in the magnetic material and the mean air gap length $2(d-q)$, where we assume the two air gaps to be identical. Ampere's law states that the line integral of the magnetic field intensity about this closed path is equal to the total amount of electrical current enclosed

within the path. Assuming that the magnetic field is everywhere perfectly aligned with the mean path then yields

$$h_m l_m + 2h_a (d - q) = NI, \tag{5.1}$$

where h_m and h_a are the magnetic field intensities in the ferromagnetic material and in the air gaps, respectively, and N is the number of windings in the coil.

Taking the magnetic properties of air and the ferromagnetic material to be linear and isotropic gives the constitutive law $B = \mu_r \mu_0 h$, where B denotes the magnetic flux density in the medium, μ_r is the relative permeability of the medium, and μ_0 is the permeability of vacuum. To determine the total magnetizing flux in the circuit, we assume that the flux density is uniformly distributed over the cross-sectional areas of the magnetic members and air gap. These areas are assumed to be equal and denoted by A. By conservation of the magnetic flux Φ_m through the circuit, it follows that $\Phi_m = B_a A = B_m A$, where B_a and B_m correspond to the magnetic flux densities in the air gap and ferromagnetic material, respectively. Together with Eqn. 5.1 and the constitutive relationship between flux density and field intensity this yields

$$\Phi_m = \frac{\mu_0 ANI}{l_m/\mu_m + 2(d - q)}, \tag{5.2}$$

where μ_m denotes the relative permeability of the ferromagnetic material and the approximation $\mu_a = 1$ has been introduced.

In the linear approximation, the voltage V_L across the inductor equals the time derivative of the flux linkage $\lambda = N\Phi$, where $\Phi = \Phi_l + \Phi_m$ is the total flux in the inductor. Here, Φ_l represents the leakage flux and accounts for that flux linkage which is not magnetizing. For simplicity assume that the corresponding leakage flux linkage is proportional to the current I with a proportionality constant given by the leakage inductance L_l. It follows that

$$\lambda = L(q) I = \left(L_l + \frac{\mu_0 AN^2}{l_m/\mu_m + 2(d - q)} \right) I. \tag{5.3}$$

Applying Kirchhoff's voltage law to the circuit shown in Fig. 5.1 and introducing the coupling constants $\beta_1 = N^2 \mu_0 A/2$ and $\beta_2 = l_m \mu_m^{-1}/2$ then yields the electrical balance equation

$$\left(L_l + \frac{\beta_1}{\beta_2 + d - q} \right) \dot{I} + \left(R + \frac{\beta_1}{(\beta_2 + d - q)^2} \dot{q} \right) I = V(t), \tag{5.4}$$

where dots denote derivatives with respect to time.

The electromagnetic forcing exerted on m is given by the gradient with respect to q of the potential

energy in the coupling field

$$E_c = \frac{1}{2}\left(L_l + \frac{\beta_1}{\beta_2 + d - q}\right) I^2, \tag{5.5}$$

i.e.,

$$F = \frac{\beta_1}{2\left(\beta_2 + d - q\right)^2} I^2. \tag{5.6}$$

Newton's second law then yields the coupled equation of motion for the mechanical system

$$m\ddot{q} + 2m\omega_0\zeta\dot{q} + m\omega_0^2 q = \frac{\beta_1}{2\left(\beta_2 + d - q\right)^2} I^2. \tag{5.7}$$

For a more detailed treatment of these derivations, see the book by Krause and Wasynczuk [34] (specifically, Eqns. (1.7-16) and (2.6-5) in [34]).

To excite the system dynamics, let $V(t) = V_0 \sin \omega t$ ($\omega = 2\pi f$) and let

$$\mathbf{x} \stackrel{def}{=} \begin{pmatrix} q & \dot{q} & I & \theta = \omega t \bmod 2\pi \end{pmatrix}^T \tag{5.8}$$

denote the system state vector, in which case

$$\frac{d\mathbf{x}}{dt} = \mathbf{f}(\mathbf{x}) \stackrel{def}{=} \begin{pmatrix} x_2 \\ -2\omega_0\zeta x_2 - \omega_0^2 x_1 + \frac{\beta_1}{2m(\beta_2+d-q)^2} x_3^2 \\ \left(L_l + \frac{\beta_1}{\beta_2+d-x_1}\right)^{-1} \left(V_0 \sin x_4 - \left(R + \frac{\beta_1}{(\beta_2+d-x_1)^2} x_2\right) x_3\right) \\ \omega \end{pmatrix}. \tag{5.9}$$

Finally, let collisional contact with the fixed stopper, corresponding to an intersection with the zero-level surface of $\delta - x_1$, result in a discrete jump in the state vector given by the map

$$\mathbf{g}(\mathbf{x}) = \begin{pmatrix} x_1 & -ex_2 & x_3 & x_4 \end{pmatrix}^T, \tag{5.10}$$

where e is a kinematic coefficient of restitution.

It is straightforward to show that the vector field $\mathbf{f}$ is equivariant under the group of transformations generated by the transformation

$$\gamma : \begin{pmatrix} x_1 & x_2 & x_3 & x_4 \end{pmatrix}^T \longmapsto \begin{pmatrix} x_1 & x_2 & -x_3 & x_4 \pm \pi \end{pmatrix}^T \tag{5.11}$$

(note that the vector field is periodic in x_4 with period 2π). It follows that if

$$\mathbf{x}(t) = \begin{pmatrix} x_1(t) & x_2(t) & x_3(t) & x_4(t) \end{pmatrix}^T \tag{5.12}$$

is a solution to the corresponding dynamical system, then so is the vector

$$\begin{pmatrix} x_1(t) & x_2(t) & -x_3(t) & x_4(t) + \pi \end{pmatrix}^T.$$

In particular, a solution that is invariant under the group action will be said to be symmetric. This is consistent with the previous definition in the case of the experimental results.

Suppose that trajectories are sampled at the zero-level surfaces of x_4 and $x_4 - \pi$, respectively. In the case of a symmetric solution, all points of intersection with $x_4 = \pi$ map under γ onto the corresponding points of intersection with $x_4 = 0$. This does not hold, however, in the case of a nonsymmetric solution. As there is no way of distinguishing the two members of the group orbit corresponding to a nonsymmetric solution by a uniform criterion across an arbitrary range of parameter values, it makes sense to record not just the intersections with $x_4 = 0$ but also the images under γ of the intersections with $x_4 = \pi$, as these collections represent both members of the group orbit. This was the methodology adopted in the experimental results reported above.

5.3.1 System identification

In order to validate the model against the experimental observations, we proceed to outline a system identification procedure used to determine values for the model parameters appearing in the vector field $\mathbf{f}$.

Mechanical parameters

The mass m of the oscillating assembly was measured on an Ohaus Series 700/800 triple beam mechanical balance and found to equal 0.646 kg. The remaining mechanical parameters ω_0 and ζ were estimated using the method of logarithmic decrements applied to the time evolution of the velocity of the unforced response after the mechanical element was released from an initial position with zero initial velocity. In particular, in each of ten separate runs, the movable mechanical element was pressed against the stop with $\delta = 0.762$ mm and released from rest. Data was collected corresponding to the first ten positive peak velocities and ω_0 and ζ were estimated for each adjacent pair of points. This resulted in a sample of 90 estimates of ω_0 and ζ, from which we selected the mean values 95.94 rad/s and 0.01626, respectively. The positive data from a sample run and the envelope calculated using the results of the identification are shown in Fig. 5.7. The fitted exponential

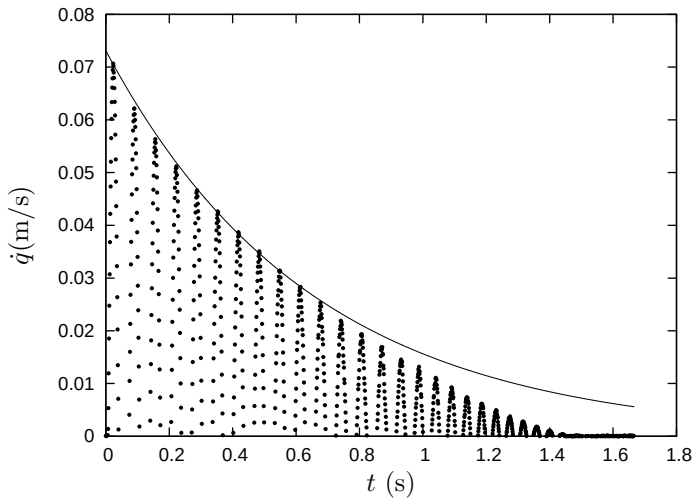

Figure 5.7: Positive half of velocity time history after release from rest. Discrete points are experimental data and the solid line is the exponential decay envelope calculated using the results from the logarithmic decrement procedure.

envelope agrees well with the decay until the oscillation amplitude falls below ≈ 0.02 m/s, suggesting that viscous damping dominates other dissipative mechanism at these amplitudes. Below 0.02 m/s, however, the theoretical prediction assuming a linear viscous damping force deviates from the experimental results. A possible source for this apparent nonlinearity is measurable contributions to damping due to dry friction.

An experimental kinematic coefficient of restitution can be calculated from trajectory data by taking the negated ratio between the velocity after each impact and the velocity before the impact. The mean of these ratios from a sample of 2000 impacts across a range of input conditions yielded $e = 0.866$. For a particular set of input conditions, e did not exhibit much variation between different individual impacts. However, for sets of impacts at different input conditions, differences in the calculated value of e between the sets could be as high as 10%.

Coupling constants

To determine the electromagnetic coupling constants, β_1 and β_2, a series of static loading experiments were performed. For each constant voltage applied, V_{DC}, the system was allowed to equilibrate and the corresponding equilibrium displacement, q_{eq}, and equilibrium current, I_{eq}, were recorded. This procedure was performed over ten separate runs. The experimental data, q_{eq} vs. I_{eq}, are plotted as discrete points in Fig. 5.8. The maximum stable equilibrium position was limited by the existence of a static snap-through point in the vicinity of $I_{eq} = 4.6$ A.

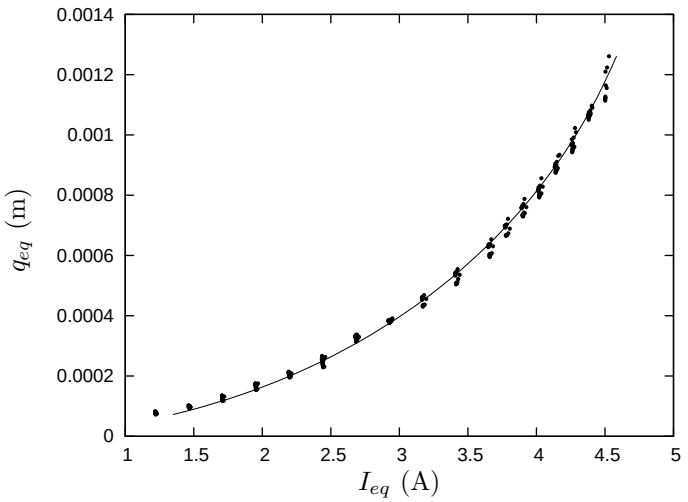

Figure 5.8: Equilibrium displacements q_{eq} and equilibrium currents I_{eq} obtained under constant excitation V_{DC}. Discrete points are from experiment and the solid line is calculated from a least squares regression using Eqn. 5.13.

For equilibria, Eqn. (5.7) yields

$$(d - q_{eq})\sqrt{2m\omega_0^2 q_{eq}} = I_{eq}\sqrt{\beta_1} - \beta_2\sqrt{2m\omega_0^2 q_{eq}}, \tag{5.13}$$

which can be used to formulate the sum of squared residuals as

$$E = \sum_{i=1}^{n}\left(I_i\sqrt{\beta_1} - \beta_2\sqrt{2m\omega_0^2 q_i} - (d - q_{eq,i})\sqrt{2m\omega_0^2 q_i}\right)^2, \tag{5.14}$$

where I_i and q_i are corresponding equilibrium current and displacement values and n is the number of data points. Applying least squares regression, i.e., requiring that $\partial E/\partial\sqrt{\beta_1} = \partial E/\partial\beta_2 = 0$, and solving for β_1 and β_2 then yields

$$\beta_1 = 2m\omega_0^2\left(\frac{\sum_{i=1}^{n}\sum_{j=1}^{n} q_i(d - q_j)I_j\sqrt{q_j} - (d - q_i)\,q_i I_j\sqrt{q_j}}{\sum_{i=1}^{n}\sum_{j=1}^{n} q_i I_j^2 - \left(\sum_{i=1}^{n} I_i\sqrt{q_i}\right)^2}\right)^2 \tag{5.15}$$

and

$$\beta_2 = -\frac{\sum_{i=1}^{n}\sum_{j=1}^{n} q_i(d - q_i)I_j^2 - I_i\sqrt{q_i}\,(d - q_j)\,I_j\sqrt{q_j}}{\sum_{i=1}^{n}\sum_{j=1}^{n} q_i I_j^2 - \left(\sum_{i=1}^{n} I_i\sqrt{q_i}\right)^2}. \tag{5.16}$$

Using Eqns. (5.15) and (5.16) with the experimental data shown in Fig. 5.8 resulted in the estimated parameter values $\beta_1 = 0.01902$ H·mm and $\beta_2 = 1.631$ mm. The resulting regression curve is shown as the solid line in Fig. 5.8.

Electrical parameters

The remaining electrical parameters were determined from the amplitude and phase response of the current signal when the movable element was clamped at fixed q and a harmonic input was applied to the terminals of the system. With the velocity term eliminated and setting $V = V_0 \sin \omega t$, Eqn. (5.4) admits the closed form solution

$$I = I_0 \sin(\omega t - \phi), \tag{5.17}$$

where

$$\tan \phi = \frac{\omega}{R}\left(L_l + \frac{\beta_1}{\beta_2 + d - q}\right) \tag{5.18}$$

and

$$I_0 = \frac{V_0}{\sqrt{R^2 + \omega^2\left(L_l + \frac{\beta_1}{\beta_2 + d - q}\right)^2}}. \tag{5.19}$$

The leakage inductance L_l and the effective resistance R can now be estimated by experimentally measuring the phase and amplitude of the steady-state response. In the time domain, the phase lag $\phi = \omega t_0$ is calculated using the known input frequency and measuring the time difference t_0 between zero-crossings of the voltage input and current response traces, respectively, as shown in Fig. 5.9. The amplitude of the current response I_0 is obtained by direct measurement in the acquired experimental data. Using a large sample of data points resulted in the estimated values $L_l = 10.55$ mH and $R = 1.390\ \Omega$. A plot of the theoretical solution calculated using the identified parameters is also shown in Fig. 5.9 for comparison with the corresponding experimental data at excitation conditions $\omega = 25.1$ rad/s, $V_0 = 1.66$ V, $d = 4.79$ mm, and $q = 1.27$ mm. (Equally convincing results were obtained when comparing response and prediction at different gap distances and input frequencies.)

Values for L_l and R obtained using this procedure were explored across a range of parameter values $V_0 = 1.66 - 6.79$ V, $q = 0 - 2.54$ mm, and $\omega = 12.57 - 50.27$ rad/s. L_l was very consistent, exhibiting little variation, and showed little if any dependence on q, V_0, or ω in these intervals. The electrical dissipation showed some slight dependence on frequency, with R increasing with ω. This variation might be due to frequency dependent dissipation in the coupling field between the coil and the electromagnet. The smallest value $R = 1.345\ \Omega$ and the largest value $R = 1.463\ \Omega$ indicate a maximum change of 8.7% over the total frequency interval. The value $R = 1.390\ \Omega$ used in the numerical simulations reported below has a maximum error of $\approx 5.2\%$.

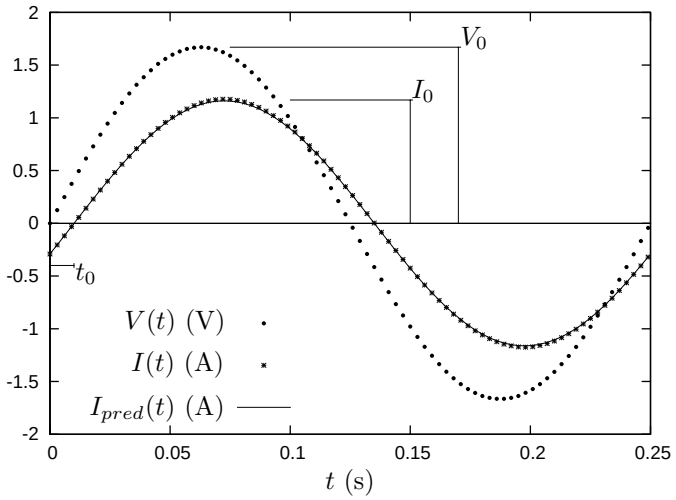

Figure 5.9: Experimental input voltage and coil current time histories (points). Solid lines show the predicted current from Eqns. 5.17-5.19 using numerical parameter values obtained through system identification.

5.3.2 Numerical results

Forward simulation of the governing equations was used to conduct numerical investigations which closely mimic the experiments carried out on the physical device. The Matlab scripts and functions used to do this are shown in Appendix C. The system behavior was numerically investigated over a frequency range of 2–10 Hz with typical input voltage amplitudes of 2–8 V. Parameters used in the numerical investigation were those found from the system identification procedure described above and the gap distances, $d = 4.79$ mm and $\delta = 1.11$ mm, were chosen so as to agree with those measured in the experimental investigations. Here, selected results are shown that demonstrate interesting behavior in the neighborhood of the onset of contact between the particle and the stopper and bear resemblance to the experimental results reported in Sec. 5.2.3.

The choice of forward simulation for the numerical investigations, rather than more sophisticated continuation techniques, is due to the complexity of the system response in the vicinity of the onset of contact. Many of the transitions to contacting behavior resulted in the system evolving to a chaotic attractor.

The bifurcation diagrams in Fig.'s 5.10, 5.11, and 5.12 were again generated by fixing the excitation frequency and alternately sweeping the input voltage amplitude in the increasing and decreasing directions, respectively, in increments of $\Delta V = 0.001$ V. The final state at the conclusion of a simulation at a particular value of the excitation parameters was used as the initial state for the subsequent simulation at a nearby value of the excitation voltage. Data shown are intersections of the solution trajectories with the constant phase sections $x_4 = 0$ and $x_4 = \pi$, albeit after applying the transformation γ to data collected at the latter section. The system was simulated for a maximum of 150 input cycles. Periodicity was checked at each intersection of the trajectory with $x_4 = 0$. If a periodic orbit was found, the simulation was stopped, relevant

section data saved, and the input voltage incremented (decremented). If no periodicity was detected, data from the last 100 intersections of the trajectory with the sections was retained prior to input increment (decrement).

Figure 5.10 shows the numerical bifurcation diagram obtained when sweeping the input voltage at an excitation frequency of $f = 6.25$ Hz. This should be compared to Fig. 5.4, which although obtained at a slightly different excitation frequency bears a significant resemblance to the results shown here. As with Fig. 5.4, panels (a) and (c) show the sampled velocities for each period of excitation when increasing the voltage (a) and decreasing the voltage (c). Starting with a symmetric periodic orbit for low input voltage (see discussion about symmetry in Sec. 5.3), the onset of low-velocity contact is induced at an input voltage near 4.85 V, after which the system settles onto a period-three, symmetric attractor, which subsequently undergoes a symmetry-breaking bifurcation to a nonsymmetric period-three attractor. This then undergoes a sequence of bifurcation to a banded chaotic attractor. Again, a significant parameter hysteresis is evident in the figure as the symmetric period-three attractor disappears in a cyclic fold bifurcation near 4.8 V. Panels (b) and (d) show the corresponding sampled currents for each period of excitation, again for increasing (b) and decreasing (d) values of the input voltage amplitude.

Similarly, Fig. 5.11 shows the results of a parameter sweep for an excitation frequency of $f = 7$ Hz. The response here clearly resembles that observed in the case of the experimental bifurcation results (see Fig. 5.5), albeit without the sometimes obfuscating noise of the experimental data. In particular, the periodic windows alluded to previously are here clearly visible including alternations between symmetric and nonsymmetric trajectories. Finally, the experimental results shown in Fig. 5.6 are closely captured by the numerical bifurcation diagram obtained for $f = 8$ Hz and shown in Fig. 5.12.

5.4 Discussion

The experimental and numerical results reported in previous sections support the notion of relying on the multidomain coupling inherent in microscale electromechanical systems for simultaneous actuation and sensing. In particular, the analysis exemplifies the possible use of nonlinear bifurcation characteristics in device design. Specifically, it was shown that the onset of contact commonly results in a significant change in the steady-state response in the mechanical system and a corresponding change in the electrical response. As an example, transitions were observed between nonimpacting periodic responses with periodicity equal to that of the excitation and impacting periodic or banded chaotic responses with recurrence three times that of the excitation. While this was somewhat obscured by noise in the experimental bifurcation diagrams

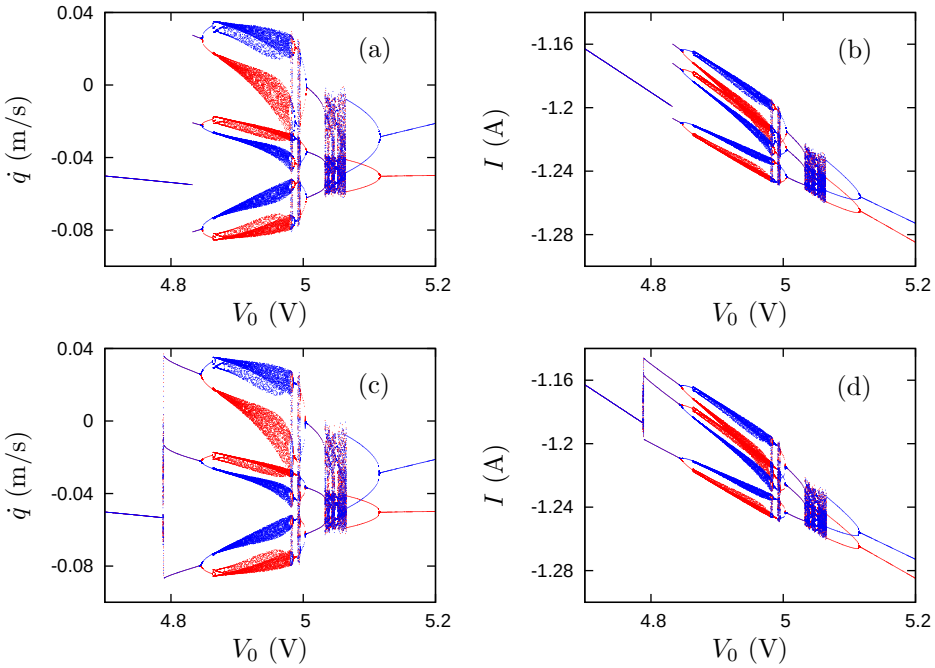

Figure 5.10: Numerical bifurcation diagrams for $f = 6.25$ Hz. Panels (a) and (c) show sampled velocities for sweeps in the up and down directions, respectively. Panels (b) and (d) show sampled electrical current for sweeps in the up and down directions, respectively. Here and in the following figures reporting numerical results, and in agreement with the experimental procedure, blue dots indicate data taken at zero-crossings of the input voltage as it is rising (i.e., at $x_4 = 0$) and red dots indicate data taken at zero-crossings of the input voltage as it is falling (i.e., at $x_4 = \pi$).

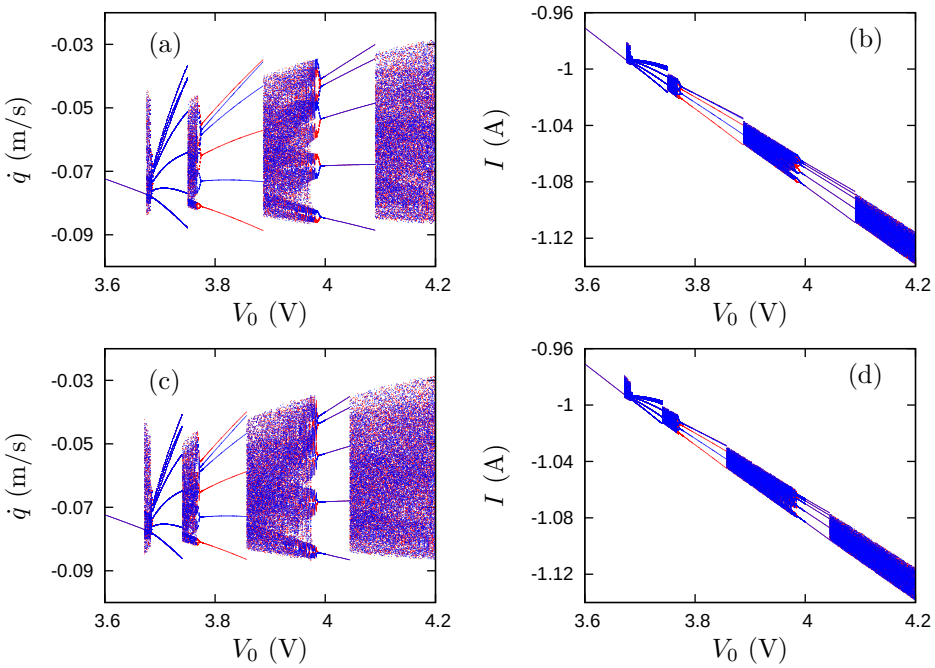

Figure 5.11: Numerical bifurcation diagrams for $f = 7$ Hz. Panels (a) and (c) show sampled velocities for sweeps in the up and down directions, respectively. Panels (b) and (d) show sampled electrical current for sweeps in the up and down directions, respectively.

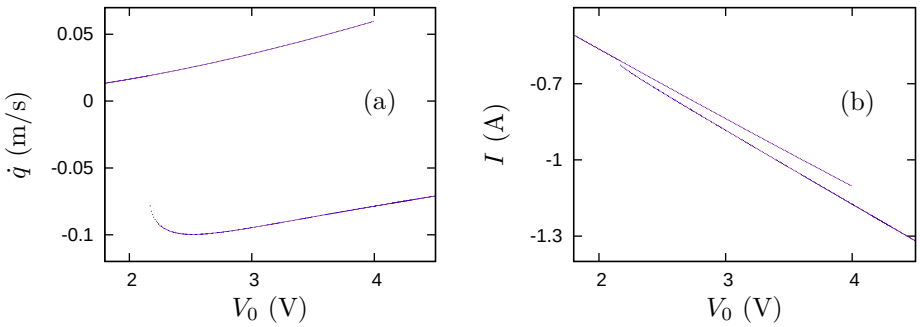

Figure 5.12: Numerical bifurcation diagrams for $f = 8$ Hz. Panels (a) and (b) show sampled velocities and currents, respectively, for sweeps in both the up and down directions.

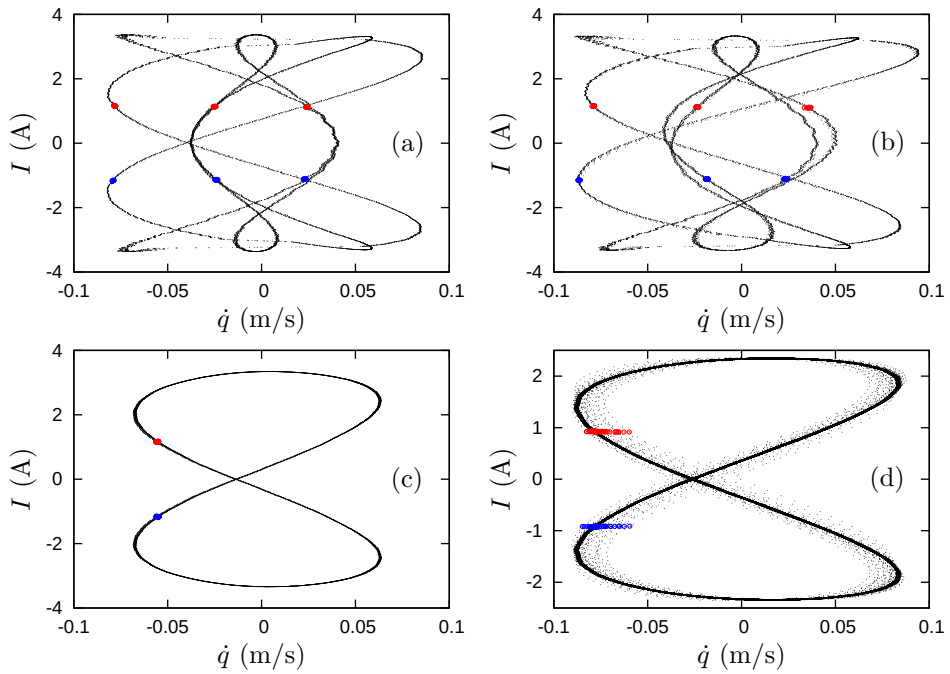

Figure 5.13: Experimental trajectories with sampled data ($V = 0$ V) shown as circles. Panel (a) shows an impacting, symmetric, period-3 orbit for $f = 6.1$ Hz, $V_0 = 5.00$ V. Panel (b) shows an impacting, nonsymmetric, period-3 orbit for $f = 6.1$ Hz, $V_0 = 4.94$. Panel (c) shows a non-impacting, symmetric, period-1 orbit for $f = 6.1$ Hz, $V_0 = 5.03$ V. Panel (d) shows as a solid line a non-impacting, symmetric, period-1 orbit for $f = 7$ Hz, $V_0 = 3.62$ V, and shows as discrete points a nearby chaotic attractor for $f = 7$ Hz, $V_0 = 3.63$ V.

showing the current response, a clearer picture emerges from the state-space trajectories.

To this end, Fig. 5.13 shows the projection of experimental state-space trajectories onto the velocity-current coordinate plane. In panel (d), the nonimpacting period-one response found for $f = 7$ Hz and $V_0 = 3.62$ V is superimposed on the chaotic impacting response found at $V_0 = 3.63$ V. In this case, the recurrence of the chaotic attractor is similar to that of the periodic response, suggesting only a broadening of the individual peaks in the frequency spectrum and relatively small changes in amplitude content. In contrast, panels (a) and (b) show the period-three impacting, symmetric and nonsymmetric responses found for $f = 6.1$ Hz and $V_0 = 5.00$ V and $V_0 = 4.94$ V, respectively. For comparison, a non-impacting period-one trajectory is shown in panel (c) for $f = 6.1$ Hz and $V_0 = 5.03$ V. Also shown in these figures are the sampled data points previously shown in Figs. 5.4 and 5.5. As seen here, triggering sampling at zero-crossings of the input voltage may result in current measurements, for which individual differences are obscured by noise. On the other hand, a different sampling scheme might result in clearly distinguishable changes in frequency content as surmised from the sampled data. Figure 5.14 illustrates the same observation in the case of the numerically simulated data.

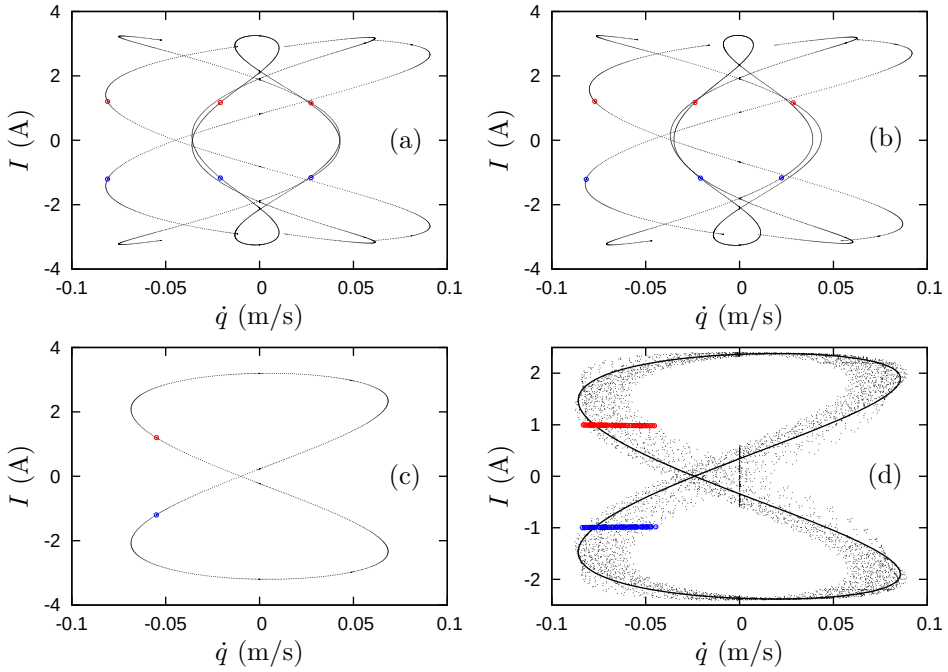

Figure 5.14: Numerical trajectories with sampled data shown as blue ($x_4 = 0$) and red ($x_4 = \pi$) circles. Panel (a) shows an impacting, symmetric, period-3 orbit for $f = 6.25$ Hz, $V_0 = 4.833$ V. Panel (b) shows an impacting, nonsymmetric, period-3 orbit for $f = 6.25$ Hz, $V_0 = 4.849$. Panel (c) shows a non-impacting, symmetric, period-1 orbit for $f = 6.25$ Hz, $V_0 = 4.832$ V. Panel (d) shows as a solid line a non-impacting, symmetric, period-1 orbit for $f = 7$ Hz, $V_0 = 3.675$ V, and shows as discrete points a nearby chaotic attractor for $f = 7$ Hz, $V_0 = 3.676$ V. (The vertical cluster of points near $\dot{q} = 0$ is a result of careful detection of local maxima in the position during integration.)

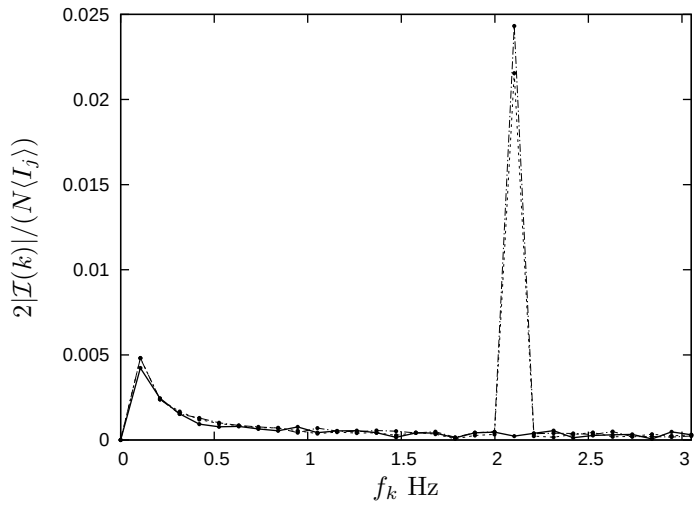

Figure 5.15: Normalized amplitude spectrum (see text for details) of the experimental data given by the blue dots in Fig. 5.13 (a) (dashed), (b) (dash-dot), and (c) (solid), respectively.

To further illustrate the change in frequency content associated with the transition to impacting behavior, let $\{I_j\}_{j=1}^N$ denote a sequence of N consecutively sampled current values at phases corresponding to zero crossings of the input voltage as it is rising, and let $\langle I_j\rangle$ denote the average of the sequence. Denote by

$$\mathcal{I}(k) = \sum_{j=1}^{N} (I_j - \langle I_j\rangle) \exp^{(-2\pi i)(j-1)(k-1)/N} \tag{5.20}$$

the discrete Fourier transform of the corresponding mean shifted sequence. It follows that, for $1 < k \leq N/2$, $2|\mathcal{I}(k)|/N$ is the amplitude of the component of the response with frequency $f_k = (k-1)/(4\pi N)$. Figure 5.15 shows the result of performing this procedure when applied to the $N = 60$ sampled experimental data corresponding to the blue circles in Fig. 5.13 panels (a)-(c), respectively. For the non-impacting, periodic orbit the sampled values are nearly constant and the resultant data represents the noise floor as a percentage of the average of the sampled currents. In the case of the two impacting orbits, the distinct peak in the data represents the contribution to the response at frequency equal to one-third the excitation frequency. As seen in the figure, the magnitude of the additional component is several percent of the signal average with a signal-to-noise ratio close to 50:1.

The agreement between numerical and experimental data demonstrated here and in previous sections is quite satisfying given the great uncertainties in parameterizing various dissipation mechanisms. This was reflected in uncertainties in the estimates of the coefficient of restitution e and the effective resistance R. Similarly, it was found that the viscous damping model yielded an estimated damping factor ζ, with which good agreement with experimental data was found only in certain ranges of displacement amplitude.

The study presented here was motivated by a desire to ultimately implement in a microelectromechanical device the two fundamental operating principles of multidomain actuation and sensing and impact-induced transitions in the steady-state response. The next chapter presents work on the design and fabrication of such a microscale device which relies on capacitive coupling for excitation of the mechanical response.

Chapter 6

Grazing-Bifurcation-Enabled MEMS Limit Switch

6.1 Introduction

As suggested in Chapter 3, many MEMS devices use some form of electrostatic interaction, either in the form of parallel-plate capacitors or through the use of electrostatic fringing fields in comb-drive actuators, in order to drive displacements or oscillations of movable elements. In the parallel-plate configuration, two conductive plates separated by a dielectric gap are placed so that their plan areas overlap. Typically one plate is fixed in a grounded frame and the other plate is suspended relative to that frame. When a voltage is applied across the plates, electrostatic interactions generate an attractive force between the plates.

Of particular interest to the design of limit switches is the snap-through instability present in parallel-plate capacitive drives. Assuming linear suspension behavior for the suspended plate, under suitable DC input voltage conditions, this configuration will undergo snap-through when the restoring force of the suspension is unable to balance the attractive electrostatic force. This results in the plates coming together and forming a conductive path of very low resistance across the device. A similar phenomenon occurs under AC input voltage conditions when the dynamic response to an oscillatory excitation exceeds a critical amplitude.

The snap-through functionality is a natural candidate for the design of a so-called crowbar, a circuit-protection device that is connected in parallel with the circuit to be protected and its source of power. Normally the crowbar is an open circuit and no current passes through it. However, if the input source rises beyond a safe operating range for the circuit being powered, the crowbar becomes a short circuit, safely routing the excessive current around the load being protected. From the above discussion, it follows that a crowbar mechanism could be implemented using a parallel-plate drive MEMS device designed to transition to the clamped configuration at the desired trigger voltage. Indeed, this type of device might be used to provide a faster acting protection mechanism than would be achievable with a more typical fuse or circuit breaker implementation.

The snap-through phenomenon described above is induced by changes in the (amplitude of the) excitation voltage across a critical level associated with a smooth subcritical bifurcation (a saddle-node or cyclic-fold

bifurcation, respectively, in the static and dynamic case), and is directly related to the nonlinear nature of the electrostatic attraction between the two parallel plates. In contrast, the grazing bifurcation induced by the onset of low-velocity contact between a moving mass and a barrier is a direct result of the nonsmoothness associated with the contact interactions. The introduction of a physical barrier in the path of the movable plate might therefore induce snap-through at an excitation voltage below the critical value associated with the electrostatic actuation. Adjustments to the position of the barrier might provide a mechanism for a tunable snap-through criticality.

The remainder of this chapter explores these ideas and is organized as follows. The next section presents numerical results on a particular switch architecture which makes use of a grazing bifurcation to trigger snap-through in a parallel plate capacitive drive. Section 6.3 then describes the fabrication of an alternative architecture which has the same mathematical description. The packaging of the devices is discussed in Sec. 6.4, which is followed by a report of the testing results in Sec. 6.5. The chapter ends with a discussion of important findings and suggestions for future direction.

6.2 An Electrostatic MEMS Switch

A schematic of one particular proposed design is shown in Fig. 6.1 and an operational schematic of the device is shown in Fig. 6.2. The device consists of a die stack in which the top die is highly doped silicon which acts as the fixed plate in a parallel-plate capacitor. Below and directly opposing the top die is an inertial mass, suspended by polymer beams, that has had its top surface plated with aluminum to form the moveable plate in the parallel-plate arrangement. The top plate and the aluminum film are separated by a polymer layer that acts as a dielectric spacer. An input voltage $\hat{V}$ is applied between the two parallel plates to generate the electrostatic forcing. Below the proof mass, a third die is bonded with a spacer layer such that contact may occur between the proof mass and a stopper patterned on the lowest die. As the amplitude of the driving voltage is increased, the amplitude of the moving electrode will grow, eventually bringing it into contact with the stopper. As shown below, through suitable design, the grazing bifurcation associated with the onset of impacts induces a rapid transient growth of oscillation amplitude that carries the moving electrode to snap-through. At this point the switch closes and current is shunted through the now shorted capacitor.

Referring to the operational schematic of the proposed MEMS device shown in Fig. 6.2, the suspended inertial mass is modeled as a point mass $\hat{m}$ suspended by a linear spring $\hat{m}\hat{\omega}_0^2$ and damper $2\hat{m}\hat{\omega}_0\zeta$, where $\hat{\omega}_0$ is the undamped natural frequency and ζ is the damping ratio. The stopper is modeled as a rigid stop

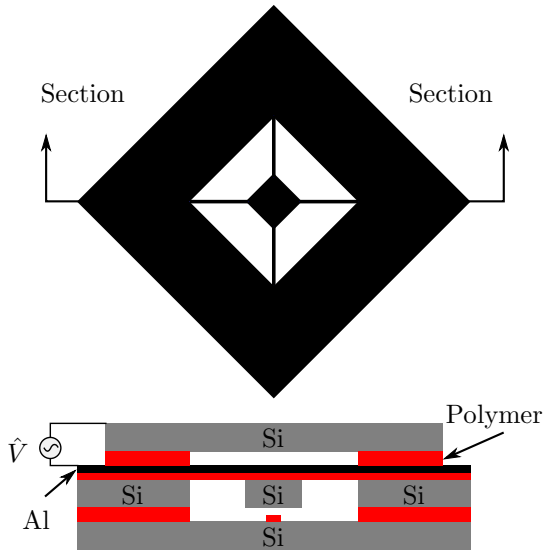

Figure 6.1: Plan (upper) and sectional (lower) schematic views of the proposed MEMS device for investigating grazing-induced snap-through behavior.

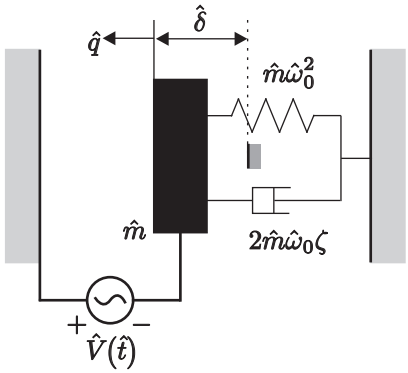

Figure 6.2: An operational schematic of the capacitively-excited parallel-plate device shown in Fig. 6.2.

with coefficient of restitution e and zero excitation equilibrium distance $\hat{\delta}$ separating $\hat{m}$ and the stop. The balance equation for the coupled electromechanical system is

$$\hat{m}\frac{d^2\hat{q}}{d\hat{t}^2} + 2\hat{m}\hat{\omega}_0\zeta\frac{d\hat{q}}{d\hat{t}} + \hat{m}\hat{\omega}_0^2\hat{q} = \frac{\hat{\varepsilon}\hat{A}_c}{2\left(\hat{d}-\hat{q}\right)^2}\hat{V}^2 \tag{6.1}$$

where $\hat{q}$ denotes the displacement of the movable electrode, $\hat{t}$ denotes time, $\hat{\varepsilon}$ is the electrical permittivity, $\hat{A}_c$ is the capacitive area, and $\hat{d}$ is the electrode gap in the absence of excitation. The rescaling $\hat{q} = \hat{d}q$ and

$\hat{t} = \hat{\omega}_0^{-1} t$ then yields the nondimensional form of the balance equation as

$$\ddot{q} + 2\zeta\dot{q} + q = \frac{E^2}{(1-q)^2} \tag{6.2}$$

where

$$E^2 = \frac{\hat{\varepsilon}\hat{A}_c\hat{V}^2}{2\hat{m}\hat{\omega}_0^2\hat{d}^3} \tag{6.3}$$

Let E be given by a square wave that switches between the levels V and 0 every π/ω units of rescaled time and denote by

$$\mathbf{x} = \begin{pmatrix} q & \dot{q} & \theta = \omega t \mathrm{mod} 2\pi \end{pmatrix}^T \tag{6.4}$$

the system state vector. Finally, let collisional contact with the fixed stopper, corresponding to the vanishing of the function $h_{\mathrm{impact}}(\mathbf{x}) = x_1 + \delta$, where $\delta = \hat{\delta}\,\hat{d}^{-1}$, result in a discrete jump in the state vector given by the map

$$\mathbf{g}(\mathbf{x}) = \begin{pmatrix} x_1 & -ex_2 & x_3 \end{pmatrix}^T \tag{6.5}$$

Suppose that $\zeta = 0.02$, $\omega = 1$, $e = 0.8$, and $\delta = 0.6$. Then, for $V = V^* \approx 0.2014$, a grazing periodic steady-state oscillation is found that is asymptotically stable in the absence of the fixed stopper. Figure 6.3 shows the time histories for the velocity of the movable electrode starting with initial conditions at the point of grazing contact with $x_3 \approx 0.7306$ and $V = V^* - 10^{-4}$ (solid) and $V = V^* + 10^{-4}$ (dotted), respectively.

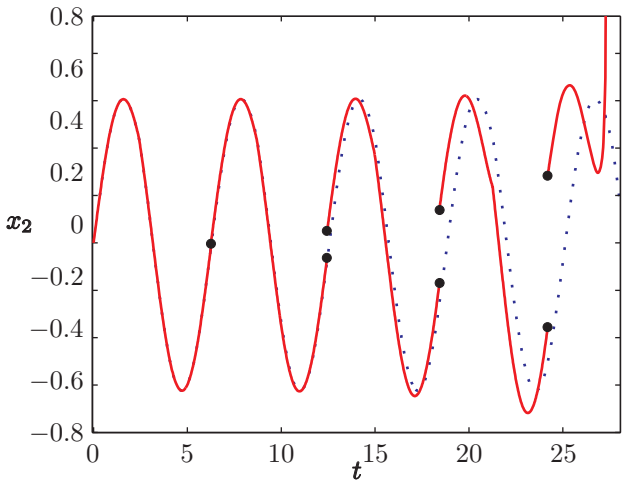

Figure 6.3: The steady-state pre-grazing response (dotted) and the transient post-grazing response (solid) with large black dots corresponding to $h_{\mathrm{impact}} = 0$.

As seen in the figure, the transient post-grazing response exhibits a rapid growth in jumps in the absolute velocity over the course of a couple of excitation cycles. The movable electrode reaches the singularity

corresponding to snap-through shortly after $t = 27.3$. This suggests that one might accurately control the introduction of snap-through by controlling the stopper position. This feature would be more difficult if relying on a smooth cyclic fold bifurcation of periodic trajectories to initiate snap-through. Additionally, near a smooth fold bifurcation, the growth rate of deviations away from the critical periodic trajectory is expected to decay to zero in the limit as the initial deviation goes to zero [37]. A snap-through function relying on perturbations away from such a condition would thus be expected to take many more cycles of excitation.

6.3 Fabrication of a revised architecture

Bulk fabrication of MEMS devices usually takes place as a series of addition and removal processes on planar layers of materials. Many of these processes, such as photolithography and thin film deposition, are directly borrowed from the microelectronics industry, while a few processes, such as deep reactive ion etching, were developed specifically for fabrication of micromechanicial structures. By selectively depositing, patterning, and removing different materials, small structures can be built to perform particular tasks and accomplish useful functions.

Many kinds of materials are used in MEMS structures to provide a wide range of mechanical and electrical properties as well as flexibility in manufacturing processes. Single crystal silicon is a very popular substrate and structural material since much processing knowledge can be used from the microelecronics industry, where it is used heavily for its properties as an inexpensive, versatile, and widely available semiconductor. Also, since MEMS are often integrated with microelectronic circuitry, having a common substrate means devices can be consolidated together on the same set of dies. Metals, such as aluminum, chrome, and gold are used as conductive layers and pathways as well as sacrificial masks in certain processing steps. Many polymers also find use in MEMS as processing masks, dielectric layers, adhesives, and permanent structures [8, 20, 45, 48, 79].

Despite the seeming simplicity of the device described in the previous section, it was found that the particular stack of patterns and material layers would be virtually impossible to fabricate. In particular, chemical incompatibilities between subsequent steps in proposed fabrication processes and lack of suitable bonding procedures to adhere the die stacks conspired to force a reconsideration of device architecture.

A plan-view schematic of the revised device architecture is shown in Fig. 6.4 with key features labeled. In the center is an H-shaped mass which is symmetrically suspended from an external frame on either side by folded-flexure assemblies. To the left of the mass (the suspended electrode) is the other electrode of the

parallel plate drive, which is fixed relative to the frame, but is electrically isolated from it. The suspension provides an electrically conductive pathway from the frame to the mass. Applying a voltage across the fixed electrode and frame actuates the mechanism. This arrangement is very similar to the design proposed by Mita et al. [8] that was studied in Chapter 2.

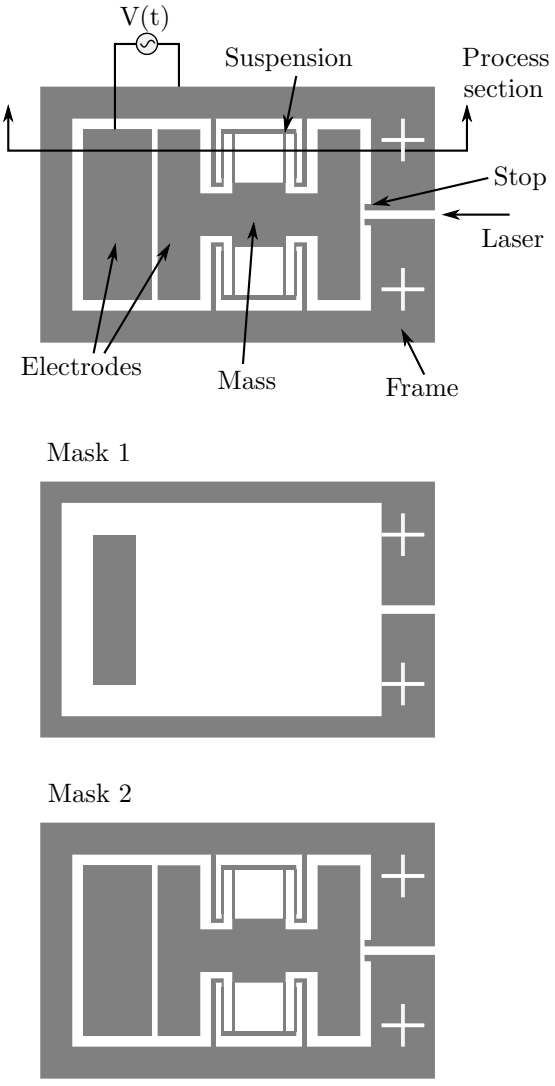

Figure 6.4: Schematic of the proposed micro-electromechanical device architecture (top) and two masks used in its fabrication (middle and bottom).

In a significant departure from Mita's design, and like the proposed device architecture shown above in Sec. 6.2, the revised design does not prevent snapthrough of the suspended electrode toward the fixed electrode, nor does it allow movement of the frame relative to a substrate. Instead of positioning a barrier in the path of the suspended electrode in order to prevent snapthrough, here the barrier (in the form of two protruding stops) is placed to the right of the mass. Between the stops is a gap in the frame to allow passage

of a laser beam for external interrogation of the motion of the mass. It should be noted that this design can still be analyzed with the same procedure presented in Sec. 6.2 of this chapter.

Several different sets of devices with different dimensions were built to explore the parameter space and to investigate the effects of processing on different feature sizes. The remainder of this section describes in some detail the process used to manufacture these devices. A more detailed process and recipe is included in Appendix D.1.

The chart in Fig. 6.5 enumerates the fabrication steps used to process the proposed micro-electro-mechanical devices, which consist of a bonded stack of dies electrically isolated by a dielectric adhesive. This fabrication procedure requires the use of two masks for the photolithography steps and two wafers are needed for each set of completed devices.

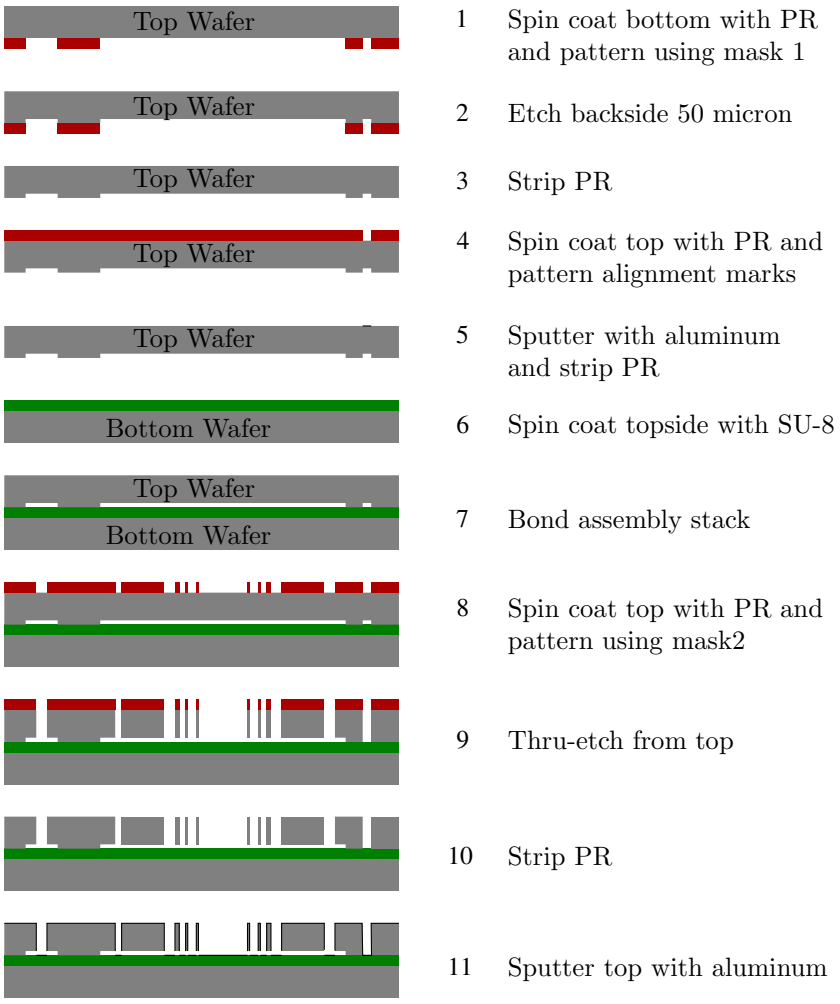

Figure 6.5: Schematics and fabrication steps as described in Section 6.3.

In the first step of the fabrication process, photoresist (PR) is spincoated on the backside of a 300 micron

thick silicon wafer and patterned using mask 1, which is shown schematically in the middle panel of Fig. 2. In the second step, the wafer is then etched to a depth of approximately 50 microns using an inductively coupled plasma (ICP) etching process, after which the PR is stripped from the top wafer in step three. These steps result in chambers in the back side of the top wafer that allow the shuttle mass to move freely without contacting the bottom wafer once the stack is bonded. The rectangle in the middle of the chamber that is not etched is the base for the fixed electrode that gets bonded to the base wafer.

In later steps, the features on the top side of the top wafer need to be aligned with the features that were etched on the bottom side of the top wafer in the first step. However, these features are hidden from view once the stack has been bonded. To provide the necessary alignment features, in the fourth step, the topside of the top wafer is spincoated with PR and patterned with mask 2, shown schematically in the lower panel of Fig. 6.5, using a backside alignment. However, only topside alignment marks are developed. In step five, aluminum is then sputtered on the topside and a lift-off procedure performed to leave the patterned aluminum alignment marks on the topside of the top wafer.

In the sixth step, a second, 500 micron thick silicon wafer is prepared for bonding by spincoating the topside with a 3 micron thick layer of thermosetting SU-8 epoxy. The bottom and top of the assembly are then bonded in step seven in an anodic bonding chamber which presses the wafer stack between two heated plates to thermally set the SU-8 epoxy in a vacuum atmosphere.

In step eight, the top of the bonded stack is spincoated with PR and patterned using mask 2, shown schematically in the lower panel Fig. 6.5. This defines the final shape of the proof mass and suspension. The features of the top mask are aligned to the features on the back using the alignment marks patterned in steps four and five. The PR developer acts as an etchant for the aluminum, thus cleaning the aluminum from the surface in preparation for the subsequent ICP etching of the silicon.

In step nine, the top wafer is thru-etched with the same ICP process used to etch the backside chambers. The SU-8 acts as a good etch stop so that the bottom wafer is not inadvertently etched in the process. The PR is removed in step 10 to expose the final device structure.

Finally, in step 11, the entire top of the bonded stack is conformally sputtered with aluminum to provide a layer of high electrical conductivity. This substantially reduces the resistance of the devices and provides for highly conductive capacitor plates. Note that the conformal sputtering does not short the capacitor plates, due to the reliefs that are undercut at the edges of the lower bonding surfaces.

At number of wafers were processed using this protocol. At the end of processing, typically only one or two devices, out of eight on each wafer, were still intact. Breakage usually occurred during step nine in Fig. 6.5 when the top wafer was thru-etched. It was theorized that heat transfer from the shuttle mass

was limited due to the presence of the chambers on the backside of the top wafer. Temperature build-up in the mass and suspensions due to this limited heat transfer caused the etch rates to increase locally. This resulted in failure of the thin suspension beams, freeing the masses completely, which subsequently fell out of the wafer if it was inverted.

Some failures also occurred in step ten in Fig. 6.5 when the last layer of PR was stripped from the top wafer. For reasons that are not yet clearly understood, the SU-8 adhesive layer exposed to the liquid PR stripper would begin to delaminate from the bottom wafer. Particles of the SU-8 would then foul the suspensions and become lodged in the capacitor gaps, effectively locking the masses in place. It was found that under extended soaking in stripper while in an ultrasonic cleaner, the particles could sometimes be dislodged. However, the ultrasonic waves in the bath sometimes destroyed the suspensions due to over-excitation.

6.4 Packaging

To minimize manufacturing, packaging, and testing difficulties, the individual devices were not diced and removed from the silicon wafers from which they were fabricated. Instead, the entire wafer was used as the external frame to which the suspensions were attached. The devices are distributed radially along the circumferences of the wafer so that by rotating the wafer around its central vertical axis, the channels between the stops can be aligned with the laser beam used to interrogate the devices.

The testing fixture shown in Fig. 6.6 was designed and built to seal the entire wafer assembly in a clean, protected chamber. The wafer rests on a central platter that is free to rotate within the chamber and is actuated by an external shaft. The laser sensor head remains on the outside of the chamber and is held so that the beam is directed down the channels through a clear viewing window in the side of the sealed chamber. This window aligns with the central vertical axis of the platter so that each device can in turn be rotated into alignment with the laser.

On the top of the fixture are two bosses with set-screws which hold gold-plated, spring loaded pins that extend into the chamber. The tips of these pins press against the electrical contact pads which provide power to the actuators.

The testing fixture was fabricated with extreme precision, but the sensor mount which was attached to it lacked sufficient adjustability and rigidity to reliably hold the laser sensor in alignment with the channel. To permanently remedy this issue, a revised apparatus for holding the sensing head would need to be designed and constructed to work with the rest of the existing fixture. Prelimiary tests of the prototype devices were

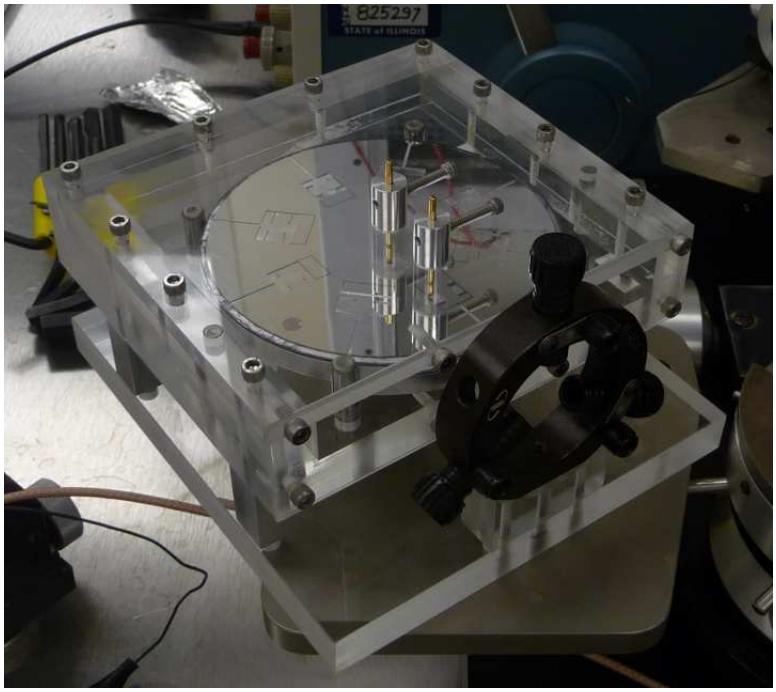

Figure 6.6: A testing fixture used to seal the entire wafer assembly in a protected chamber while allowing the laser beam clear and uninterrupted access to the shuttle mass.

conducted with the laser mounted temporarily to a 3-axis micromanipulator.

It was also found that the clear viewing window through which the laser passed was actually generating some unwanted reflections. Prior to fabricating the fixture, the idea of a window was tested by passing the laser through a sample piece of clear acrylic and the results indicated the beam was not being affected. Perhaps differences in surface quality or material properties between the test sample and the acrylic used in the construction of the fixture are to blame. The window was simply removed for testing, since the preliminary investigation took place within the cleanroom.

6.5 Preliminary Tests of the Prototype

A photograph of the apparatus as tested is shown in Fig. 6.7. In the center of the image is the acrylic test packaging in which the wafer rests. To the right is the micromanipulator with the LMI Technologies LNS 18/120 laser displacement sensor mounted on its arm. Although this was still not robust even to light disturbances, it provided precise enough movements that the laser could be accurately pointed down the channel to reflect off the shuttle mass. On top of the acrylic chamber, the two leads which power the device are clamped to the input pins.

The laser beam from the displacement sensor has a beam diameter of 4 μm, so it is nearly impossible

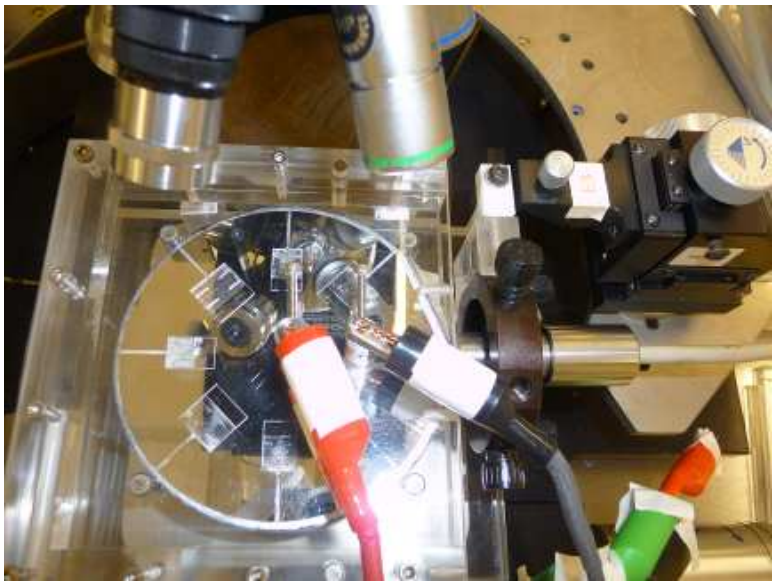

Figure 6.7: Photograph of the MEMS apparatus under test.

to see or adjust by the naked eye. To determine alignment, the output of the sensor was monitored on a Tektronix 2235 oscilloscope while the micromanipulator was adjusted until a signal was observed. A series of static excitation voltages in the range of 0–50 VDC was applied to the terminal pins using a Keithley 237 high voltage power supply. Movement of the shuttle mass was confirmed visually and the signal from the LNS registered slight changes at the different voltage levels. The shuttle mass was also visually confirmed to snap-through to the closed position when incrementing the input beyond 50VDC. However, the signal from the LNS only indicated a movement of 1 μm, which was clearly incorrect. Since the integrity of the data could not be guaranteed, no experimental data is included here.

6.6 Concluding discussion

The overall device design and construction process was successful and resulted in functioning MEMS devices. The devices were visually confirmed to be operational and indications are that further efforts to refine the experimental test fixture would result in accurate and satisfactory test data. Additonal means of obtaining experimental data are also being investigated. For example, a high speed camera could be mounted above the test fixture to capture images of a device as it was actuated. Image processing routines could then be used to edge-detect the moving mass and obtain a time evolution of the movement of the mass.

After confirming the validity of the data being acquired, system identification procedures would need to be developed, similar to those presented in Chapter 5. This would result in parameter values which could

be used in numerical simulation for comparison to experimental data.

Further, it would be interesting to examine and adjust process variables to try to increase the yield rate. One iteration of this was already performed by trying a second mask 2 which had different device sizes. It would also be of interest to perform a design-of-experiment analysis to investigate the impact of process parameters on yield, in particular for the bonding and thru-etch processes which were the primary causes of device failure.

From the point of view of the broader research effort, the success in producing functioning devices is a big step in moving towards sensing systems based on these ideas. Having a baseline from which to work and develop opens up possibilities for further device enhancement. For instance, through the introduction of moveable stops, a tunable device might be created, which could be adjusted to provide different trigger points. In future development, one might even imagine real-time control, as suggested in Dankowicz and Svahn [10], which would further augment device functionality.

Chapter 7

Conclusions

This dissertation has explored the potential for grazing bifurcations to provide a useful means of creating fast-acting limit switches. Chapter 1 discussed the use of limit switches as indicators and control devices and how they are critical mechanisms for providing logic and safety interlocks in many consumer and industrial applications. This chapter also introduced the reader to some of the concepts to be examined in detail in later chapters.

Chapter 2 went on to present a detailed numerical analysis of a MEMS impact actuator using the software application $\widehat{\text{TC}}$. This chapter discussed modeling of hybrid systems and demonstrated how numerical continuation can be used to map out the bifurcation behavior of a mechanism in the state space of of the system. The basic architecture of the example device was later borrowed for use in Chapter 6 in a novel implementation of a MEMS limit switch.

Chapter 3 presented an exploration of an electrostatically-actuated, microscale Euler-Bernoulli beam which was modeled using continuum assumptions. The PDE which described its behavior was discretized using the Galerkin method and a sequence of reduced-order models were presented. Through the use of this example, the chapter demonstrated modeling and numerical simulation techniques and also discussed the characteristic features of grazing-induced bifurcations in mechanical systems with rigid impact and compliant contact. Numerical results were presented which showed changes in system response associated with the onset of low-relative-velocity contact.

In Chapter 4, the rapid transient behavior associated with grazing bifurcations in a mechanical system was studied using analytical, numerical, and experimental methods. It was shown that the rate of growth of successive impact velocities increases beyond all bounds as the threshold parameter value is approached. It was then argued that a limit switch based on this nonsmooth fold scenario would be expected to outperform one that relies on a smooth bifurcation, such as the cyclic-fold bifurcation, in terms of switching speed and sensitivity.

To explore these ideas further and investigate the possibility for direct transduction of the mechanically-induced bifurcation in a coupled electrical signal, a custom testbed was designed and built which allows

further study of grazing bifurcations in the context of coupled, electromechanical systems. The material presented in Chapter 5 demonstrated good agreement between numerical and experimental results. Further, it was shown that changes in periodicity of the post-grazing response could be used, with suitable signal processing, to readily detect the bifurcation in the electrical current response.

Finally, Chapter 6 combined these concepts to propose a novel implementation of a MEMS-based limit switch which uses grazing bifurcations to trigger snap-through of the plates in a parallel-plate, electrostatic actuator. The operational phenomenology of the mechanism was shown to work in numerical simulation and experimental specimens were fabricated to demonstrate an actual, working device. The devices were visually verified to be moving, indicating that the fabrication process was viable. Issues related to data acquisition prevented complete validation of the numerical predictions.

Ongoing and future work should focus on resolving the data acquisition issues which prevented successful demonstration of the MEMS switch developed in Chapter 6. Some additional possibilities which avoid the use of a laser displacement sensor, as was attempted here, include the use of a laser doppler vibrometer or the use of high speed imaging equipment with image processing software. It might also be possible to make use of capacitance sensing to deduce the displacement of the oscillating mass.

Appendix A

Matlab Simulation Files for Chapter 4

```
% Bryan Wilcox
% SwedenDriver.m
% 11/3/2007
% Script to drive the numerical simulator for the experimental apparatus
% from the Summer 2007 trip to Sweden

% Initial Separation Distance
b = 0.6500;

% Coefficient of Restitution
e=0.55;

% Input Frequency and Amplitude

freq = 6; % [Hz]
omega = 2*pi*freq; % Calculate circular frequency for simulation purposes
A = b+5e-4;

% Maximum number of impacts to simulate.

max_impacts = 20;

% Simulation Precision (See ode45 help file)

rel_tol = 1e-12;
abs_tol = 1e-12;
init_step = .0001;

% Number of input cycles before simulation is aborted without impacts
% This prevents an infinite loop because of a mistake in setting initial
% separation and driving amplitude.

t_incr = 8*pi/omega;

t_int = [0 t_incr]; % Set the time increment for an integration run

% Initial Conditions on ['position' 'velocity' 'phase']
IC = [0 0 0];


% Index control variable and counter for number of impacts
i = 1;

% Initialize empty arrays to prevent logic errors
time_data=[];
vel_data=[];
pos_data=[];

while i ≤ max_impacts % Stop after 'max_impacts' impacts
    clear sol
```

```
    sol=DynSim(rel_tol,abs_tol,init_step,t_int,IC,A,b,omega);

    if isempty(sol.ie)
        % No impact detected before the end of the time interval, break the SIM
        fprintf('No Impact.\n')
        fprintf('Check step sizes in the integration.\n')
        fprintf(['Make sure input amplitude is greater than initial ' ...
                 'separation distance.\n'])
        break
    elseif sol.ie(end) == 1
        % Impact detected as event function decreased. Save data, apply jump
        % map, reset time interval, increment counter, then pass to loop
        % control.

        saved_sol(i)=sol; % Save all data from each run.
        time_data(end+1:end+length(sol.x))=sol.x; % Isolate time data
        pos_data(end+1:end+length(sol.x))=sol.y(1,:); % Isolate position data
        vel_data(end+1:end+length(sol.x))=sol.y(2,:); % Isolate velocity data

        IC = [sol.y(1,end)+1e-6 A*omega*cos(sol.y(3,end))+...
              e*(A*omega*cos(sol.y(3,end))-sol.y(2,end)) sol.y(3,end)];
        t_int = [sol.x(end) sol.x(end)+t_incr];
        i=i+1;
    elseif sol.ie(end) == 2
        % Impact detected as event function increased. Something strange, sound
        % the alert.
        fprintf(['ALERT: Impact detected as event function increased. ' ...
                 'Investigate. \n'])
        break
    else
        % Catch-all in case something really weird happens
        fprintf('Uh oh, something really broke. Tell Bryan.\n')
        break
    end
end

figure
plot(time_data,vel_data,'.')
xlabel('Time (s)','FontSize',14)
ylabel('Ball velocity (mm/s)','FontSize',14)
```

```
% Bryan Wilcox
% DynSym.m
% 11/3/2007
% Code to forward simulate the Sweden Apparatus

% First two event functions watch for impacts. They should only occur as
% the event function decreases, but the increasing case is checked as
% well to look for errors in the formulation.

% UPDATE: Modified to investigate rates of increase in the
% displacement. Watch the turn-around point with event function number
% 3.

function sol=DynSim(rel_tol,abs_tol,init_step,t_int,IC,Z,z_0,omega)
options = odeset('Events',@events,'RelTol',rel_tol,'InitialStep', ...
                 abs_tol,'MaxStep',init_step);

sol = ode45(@DE,t_int,IC,options,Z,z_0,omega);

%-----------------------------------------------------------------------
function [value,isterminal,direction] = events(t,x,Z,z_0,omega)
% Impact Event
value(1) = x(1)-(Z*sin(x(3))-z_0);    %
```

```
isterminal(1) = 1;  % 1 if the integration is to terminate at a zero of this
                    % event function and 0 otherwise
direction(1) = -1;  % 0 if all zeros are to be computed (the default), +1 if
                    % only the zeros where the event function increases, and
                    % -1 if only the zeros where the event function decreases.

value(2) = x(1)-(Z*sin(x(3))-z_0);
isterminal(2) = 1;
direction(2) = 1;
% Period Event
value(3) = x(2); % Check peak displacement
isterminal(3) = 0;
direction(3) = -1;

%-------------------------------------------------------------------------
function dx = DE(t,x,Z,z_0,omega)
dx=zeros(3,1);
dx(1)=x(2);
% damping and nat. freq. current as of 4-16-2008
dx(2)=-(2*0.0881*25.2*x(2)+25.2^2*x(1));
dx(3)=omega; % Input frequency
```

Appendix B

Matlab Data Acquisition Files for Chapter 5

```
%% Bryan Wilcox
%% DENSAT_acquire_swpV.m
%% 20104030
%% Script to automatically sweep the input voltage for experimental
%% DENSAT bifurcation diagrams

%% Initialize sweep parameters

%% Start points
begfreq=6.1;
endfreq=6.1;
freqincr=0.1;
freq=begfreq:freqincr:endfreq;
lenfreq=length(freq);

minvpp=5.5;
maxvpp=6.5;
vppincr=0.01;

vppup=minvpp:vppincr:maxvpp;
vppdwn=maxvpp:-vppincr:minvpp;
lenvppup=length(vppup);
lenvppdwn=length(vppdwn);

dirflag=1;

%% Initialize serial connection to function generator
s=serial('COM1','baudrate',9600,'parity','none', ...
     'StopBits',2,'FlowControl','software');
fopen(s)
fprintf(s,'SYST:REM')
fprintf(s,'*CLS')

%% Initialize analog acquisition connection to USB-6211 on Dev1
ai = analoginput('nidaq','Dev1');
addchannel(ai, 0:3);
set(ai,'InputType','Differential');
ai.SampleRate = 1000;
ai.SamplesPerTrigger = 10000; % 10 s of data
aiduration=ai.SamplesPerTrigger/ai.SampleRate;

freqind=1;
while freqind≤lenfreq
  inputcmd=sprintf('APPL:SIN %i, %i, 0',freq(freqind),vppup(1));
  fprintf(s,inputcmd);
  vppupind=1;
  if dirflag==1
    while vppupind≤lenvppup
      %% Set HP33120A outputs
      freq(freqind)
```

```
51        vpp=vppup(vppupind)
52        dirflag
53        inputcmd=sprintf('VOLT %i',vpp);
54        fprintf(s,inputcmd);
55
56        pause(20); % give the system 10 seconds to settle
57        % Start the acquisition
58        start(ai);
59        % Wait up to additional 5 seconds before getting data
60        wait(ai,aiduration+20);
61
62        % Acquire data into the MATLAB workspace
63        [data,time] = getdata(ai);
64        % format output matrix
65        outdat=[time, data];
66        % outfile string format
67        % yearmonthday_hrminsec_freq(in mHz)_VPP(in mV)
68        % sample corresponds to Mar. 31, 2010 at 3:30:21 pm 5 Hz 5 VPP
69        % 20100331_153021_5000_5000
70        outtime=fix(clock);
71        freqout=freq(freqind)*1000; % convert to mHz
72        vppout=vpp*1000; % convert to mV
73        outfile= ...
74            sprintf('%4d%02d%02d_%02d%02d%02d_%05.0f_%05.0f_%1.0f.dat', ...
75                    outtime(1:6),freqout,vppout,dirflag);
76        save(outfile,'-ascii','-double','outdat')
77        vppupind=vppupind+1;
78      end
79    end
80
81    dirflag=0;
82    vppdwnind=1;
83    while vppdwnind≤lenvppdwn
84        %% Set HP33120A outputs
85        freq(freqind)
86        vpp=vppdwn(vppdwnind)
87        dirflag
88        inputcmd=sprintf('VOLT %i',vpp);
89        fprintf(s,inputcmd);
90
91        pause(10); % give the system 10 seconds to settle
92        % Start the acquisition
93        start(ai);
94        % Wait up to additional 5 seconds before getting data
95        wait(ai,aiduration+5);
96
97        % Acquire data into the MATLAB workspace
98        [data,time] = getdata(ai);
99        % format output matrix
100       outdat=[time, data];
101       % outfile string format
102       % yearmonthday_hrminsec_freq(in mHz)_VPP(in mV)
103       % sample corresponds to Mar. 31, 2010 at 3:30:21 pm 5 Hz 5 VPP
104       % 20100331_153021_5000_5000
105       outtime=fix(clock);
106       freqout=freq(freqind)*1000; % convert to mHz
107       vppout=vpp*1000; % convert to mV
108       outfile= ...
109           sprintf('%4d%02d%02d_%02d%02d%02d_%05.0f_%05.0f%1.0f.dat', ...
110                   outtime(1:6),freqout,vppout,dirflag);
111       save(outfile,'-ascii','-double','outdat')
112       vppdwnind=vppdwnind+1;
113   end
114
115   dirflag=1;
116   freqind=freqind+1;
117 end
```

```
118
119 %% Clean up serial connection
120 vpp=0.1;
121 inputcmd=sprintf('APPL:SIN %i, %i, 0',freq(freqind),vpp);
122 fprintf(s,inputcmd);
123 fclose(s)
124 delete(s)
125 clear s
126
127 %% Clean up DAQ connection
128 stop(ai);
129 delete(ai);
```

```
1  %% Bryan Wilcox
2  %% phasesecs.m
3  %% 20104030
4
5  % Processes data from DENSAT Vpp sweep experiments to extract Poincare
6  % sections at different values of the phase.
7
8  %% slice and dice
9  superclean;
10
11
12 constphase={};
13 % velmaxima={};
14 % velminima={};
15 % posmaxima={};
16 % posminima={};
17 velmax={};
18 velmin={};
19 posmax={};
20 posmin={};
21
22 temp=dir('*.dat');
23 numch=4; % number of data channels acquired
24 %% time is the first column of the data file
25 incol=2;  % column of the input
26 chname={'V','I','q','dotq'};
27
28 phasefrac=[0 1/4 1/2 3/4];  % input phase (fraction of 2pi) to sample
29                             % data. i.e. 1/4=>pi/2
30
31 %%%%%%%%%%%%%%%%%%%  START: Info from filenames  %%%%%%%%%%%%%%%%%%%%%%%%%%%
32 j=0;
33 for i=1:length(temp)
34     if strncmp(temp(i).name,'2010',4)
35         %% only load original data files, must start with 2010
36         j=j+1;
37         datfile{j}=temp(i).name;
38         freq(j)=str2num(temp(i).name(17:21))/1000; % convert mHz to Hz
39         vpp(j)=str2num(temp(i).name(23:27))/1000;        % convert mV to V
40         swpdir(j)=str2num(temp(i).name(29));
41     end
42 end
43 %%%%%%%%%%%%%%%%%%%  END: Info from filenames  %%%%%%%%%%%%%%%%%%%%%%%%%%%
44
45 %%%%%%%%%%%%%%%%%%%  START: Datamining  %%%%%%%%%%%%%%%%%%%%%%%%%%%
46 ufreq=unique(freq)
47
48 k= 1;% k indexes over unique frequencies
49 ufreqind=find(freq==ufreq(k)); % get indices for current unique
50                                % frequency
51 %% initialize freq-wide datasets
```

```
freqphasedat=cell(size(phasefrac));

%% Cycle through individual runs to collect data
for r=1:length(ufreqind) % r is index for each unique run at a freq
    i=ufreqind(r) % i contains the index of the run in the global set
    data=load(datfile{i}); % get the raw data
    dt=data(2,1)-data(1,1); % get the sampling rate
    T=1/freq(i); % calculate the period

    %% Time shift data set to index input voltage as sin input
    for j=1:(length(data(:,1))-1)
        % looking for zero crossing in the increasing direction
        if data(j,incol)<0 && data(j,incol)*data(j+1,incol)<0
            %% zero index the time to make input a sin wave
            %% use linear interpolation to locate t=0
            %% start of sine wave is between j and j+1
            tshift=interp1([data(j,incol) data(j+1,incol)],...
                           [data(j,1),data(j+1,1)],0);
            data(:,1)=data(:,1)-tshift; % zero index the time
            data=data(j:end,:); % remove junk prior to t=0;
            break
        end
    end

    %        for a=1:length(phasefrac)
    runphasedat=[];
    %% Collect data at constant phase Poincare sections
    %% Generate array of time stamps on the available zero phase sections
    tphase=0:T:data(end,1);
    runphasedat0=[tphase(1:end-1)' zeros(length(tphase)-1,numch)];
    runphasedat1=[(tphase(1:end-1)+T/4)' zeros(length(tphase)-1,numch)];
    runphasedat2=[(tphase(1:end-1)+T/2)' zeros(length(tphase)-1,numch)];
    runphasedat3=[(tphase(1:end-1)+3*T/4)' zeros(length(tphase)-1,numch)];
    len=length(tphase);

    for m=1:len-1 % index over the periods
        %% Get the index for the first point beyond the time stamp
        ind0=find(data(:,1)>tphase(m),1);
        for n=1:numch
            %% Interpolate data and save into cell array
            runphasedat0(m,n+1)=interp1([data(ind0-1,1) data(ind0,1)],...
                                [data(ind0-1,n+1) data(ind0,n+1)],tphase(m));
        end
        ind1=find(data(:,1)>tphase(m)+T/4,1);
        %% phase section lies between ind and ind-1
        for n=1:numch
            %% Interpolate data and save into cell array
            runphasedat1(m,n+1)=interp1([data(ind1-1,1) data(ind1,1)],...
                                        [data(ind1-1,n+1) data(ind1,n+1)],...
                                        tphase(m)+T/4);
        end
        ind2=find(data(:,1)>tphase(m)+T/2,1);
        %% phase section lies between ind and ind-1
        for n=1:numch
            %% Interpolate data and save into cell array
            runphasedat2(m,n+1)=interp1([data(ind2-1,1) data(ind2,1)],...
                                        [data(ind2-1,n+1) data(ind2,n+1)],...
                                        tphase(m)+T/2);
        end
        ind3=find(data(:,1)>tphase(m)+3*T/4,1);
        %% phase section lies between ind and ind-1
        for n=1:numch
            %% Interpolate data and save into cell array
            runphasedat3(m,n+1)=interp1([data(ind3-1,1) data(ind3,1)],...
                                        [data(ind3-1,n+1) data(ind3,n+1)],...
                                        tphase(m)+3*T/4);
        end
```

```
    end
    % average the input voltage amplitudes
    Vin=mean(abs([runphasedat1(:,2);runphasedat3(:,2)]));
    %% Append run phase data to freq phase data set.
    freqphasedat{1}=[freqphasedat{1}; vpp(i)*ones(len-1,1) Vin*ones(len-1,1) ...
                     runphasedat0 swpdir(i)*ones(len-1,1)];
    freqphasedat{2}=[freqphasedat{2}; vpp(i)*ones(len-1,1) Vin*ones(len-1,1) ...
                     runphasedat1 swpdir(i)*ones(len-1,1)];
    freqphasedat{3}=[freqphasedat{3}; vpp(i)*ones(len-1,1) Vin*ones(len-1,1) ...
                     runphasedat2 swpdir(i)*ones(len-1,1)];
    freqphasedat{4}=[freqphasedat{4}; vpp(i)*ones(len-1,1) Vin*ones(len-1,1) ...
                     runphasedat3 swpdir(i)*ones(len-1,1)];
    %      end

end
%% save off global data sets for this freq
%% constphase becomes a cell array of cell arrays, the first index
%% corresponds to a unique frequency, the second index corresponds to a
%% phase section within that group of frequency runs
constphase{k}=freqphasedat;


clear T data dt extind freqphasedat freqposmax freqposmin freqvelmax freqvelmin
clear i incol ind ind1 ind2 j k len m n runphasedat runposmax runposmin
clear runvelmax runvelmin temp tperiod tphase tshift r a ufreqind

save phasesecsoutput
```

```
%% Bryan Wilcox
%% velpeaks.m
%% 20104030

% Processes data from DENSAT Vpp sweep experiments to extract peak
% values of the data for each period.

%% slice and dice
superclean;


constphase={};
% velmaxima={};
% velminima={};
% posmaxima={};
% posminima={};
velmax={};
velmin={};
posmax={};
posmin={};

temp=dir('*.dat');
numch=4; % number of data channels acquired
%% time is the first column of the data file
incol=2;  % column of the input
chname={'V','I','q','dotq'};

% input phase (fraction of 2pi) to sample data. i.e. 1/4=>pi/2
phasefrac=[0 1/4 1/2 3/4];

%%%%%%%%%%%%%%%%%%%%  START: Info from filenames  %%%%%%%%%%%%%%%%%%%%%%%%%%
j=0;
for i=1:length(temp)
    if strncmp(temp(i).name,'2010',4)
        %% only load original data files, must start with 2010
        j=j+1;
```

```
        datfile{j}=temp(i).name;
        freq(j)=str2num(temp(i).name(17:21))/1000; % convert mHz to Hz
        vpp(j)=str2num(temp(i).name(23:27))/1000;       % convert mV to V
        swpdir(j)=str2num(temp(i).name(29));
    end
end
%%%%%%%%%%%%%%%%%%%%  END: Info from filenames  %%%%%%%%%%%%%%%%%%%%%%%%%%

%%%%%%%%%%%%%%%%%%%%  START: Datamining  %%%%%%%%%%%%%%%%%%%%%%%%%%%%%%
ufreq=unique(freq);

%% Collect data from each unique frequency
for k=1:length(ufreq) % k indexes over unique frequencyis
    ufreqind=find(freq==ufreq(k)); % get indices for current unique frequency
    %% initialize freq-wide datasets
    freqphasedat=cell(size(phasefrac));
    freqvelmin=[];
    freqvelmax=[];
    freqposmin=[];
    freqposmax=[];

    %% Cycle through individual runs to collect data
    for r=1:length(ufreqind) % r is control index for each unique run at a freq
        i=ufreqind(r) % i contains the index of the run in the global set
        data=load(datfile{i}); % get the raw data

        %% THIS IS BIG - cut the collected data sample in half. Some of the
        %% runs appear to ring at the beginning.

        data=data(end/2:end,:);

        dt=data(2,1)-data(1,1); % get the sampling rate
        T=1/freq(i); % calculate the period

        %% Time shift data set to index input voltage as sin input
        for j=1:(length(data(:,1))-1)
            % looking for zero crossing in the increasing direction
            if data(j,incol)<0 && data(j,incol)*data(j+1,incol)<0
                %% zero index the time to make input a sin wave
                %% use linear interpolation to locate t=0
                %% start of sine wave is between j and j+1
                tshift=interp1([data(j,incol) data(j+1,incol)], ...
                               [data(j,1),data(j+1,1)],0);
                data(:,1)=data(:,1)-tshift; % zero index the time
                data=data(j:end,:); % remove junk prior to t=0;
                break
            end
        end


        for a=1:length(phasefrac)
            runphasedat=[];
            %% Collect data for a constant phase Poincare section
            %% Generate array of time stamps on the phase section
            tphase=phasefrac(a)*T:T:data(end,1);
            runphasedat=[tphase' zeros(length(tphase),numch)];
            len=length(tphase);
            for m=1:len
                %% Get the index for the first point beyond the time stamp
                ind=find(data(:,1)>tphase(m),1);
                for n=1:numch
                    %% Interpolate data and save into cell array
                    runphasedat(m,n+1)=interp1([data(ind-1,1) ...
                                        data(ind,1)],[data(ind-1,n+1) ...
                                        data(ind,n+1)],tphase(m));
                end
            end
```

```
104
105             %% Append run phase data to freq phase data set.
106             freqphasedat{a}=[freqphasedat{a}; vpp(i)*ones(len,1) ...
107                             runphasedat swpdir(i)*ones(len,1)];
108         end
109
110         %% Sequentially search for max and min per period
111         tperiod=0:T:data(end,1);
112         runvelmin=zeros(length(tperiod)-1,numch+1);
113         runvelmax=zeros(length(tperiod)-1,numch+1);
114         runposmin=zeros(length(tperiod)-1,numch+1);
115         runposmax=zeros(length(tperiod)-1,numch+1);
116         len=length(tperiod)-1;
117         for m=1:len
118             ind1=find(data(:,1)≥tperiod(m),1);
119             ind2=find(data(:,1)≥tperiod(m+1),1);
120
121             [temp,extind]=min(data(ind1:ind2,5)); % min velocity
122             runvelmin(m,:)=data(ind1+extind-1,:); % get data at min index
123             [temp,extind]=max(data(ind1:ind2,5)); % max velocity
124             runvelmax(m,:)=data(ind1+extind-1,:); % get data at max index
125
126             [temp,extind]=min(data(ind1:ind2,4)); % min position
127             runposmin(m,:)=data(ind1+extind-1,:); % get data at min index
128             [temp,extind]=max(data(ind1:ind2,4)); % max postion
129             runposmax(m,:)=data(ind1+extind-1,:); % get data at max index
130         end
131 % plot(runposmax(:,1),runposmax(:,4),'ko',runposmin(:,1),runposmin(:,4),'ko')
132 % plot(runvelmax(:,1),runvelmax(:,5),'ko',runvelmin(:,1),runvelmin(:,5),'ko')
133         %% Append run extrema data to freq extrema data set.
134         freqvelmin=[freqvelmin; vpp(i)*ones(len,1) runvelmin ...
135                     swpdir(i)*ones(len,1)];
136         freqvelmax=[freqvelmax; vpp(i)*ones(len,1) runvelmax ...
137                     swpdir(i)*ones(len,1)];
138         freqposmin=[freqposmin; vpp(i)*ones(len,1) runposmin ...
139                     swpdir(i)*ones(len,1)];
140         freqposmax=[freqposmax; vpp(i)*ones(len,1) runposmax ...
141                     swpdir(i)*ones(len,1)];
142     end
143     %% save off global data sets for this freq
144     %% constphase becomes a cell array of cell arrays, the first index
145     %% corresponds to a unique frequency, the second index corresponds to a
146     %% phase section within that group of frequency runs
147     constphase{k}=freqphasedat;
148     velmin{k}=freqvelmin;
149     velmax{k}=freqvelmax;
150     posmin{k}=freqposmin;
151     posmax{k}=freqposmax;
152 end
153
154 clear T data dt extind freqphasedat freqposmax freqposmin freqvelmax freqvelmin
155 clear i incol ind ind1 ind2 j k len m n runphasedat runposmax runposmin
156 clear runvelmax runvelmin temp tperiod tphase tshift r a ufreqind
157 %% save off plot data
158
159 % dirname=pwd;
160 %
161 % for j=1:numch
162 %     figure(j)
163 %     plotdata=[datset(:,1) datset(:,j+2)];
164 %     plot(plotdata(:,1),plotdata(:,2),'b.');
165 %     hold on
166 %     outfile=sprintf('%s_%s.dat',dirname(end-18:end),chname{j});
167 %     save(outfile,'plotdata','-ascii');
168 % end
169
170 for i=1:length(ufreq)
```

```
    figure(i)
    plot(posmax{i}(:,1),posmax{i}(:,5),'.')
end
```

```
% Bryan Wilcox
% sectionplots.m

% plot data from phasesecs.m and velpeaks.m output

close all

sec=1;
secsym=3;
xmin=5.5;
xmax=6.5;
vpk=2; %% index into constphase cell array for peak input voltage
% col 1=vpp
% col 2=time
% col 3=Vin
% col 4=I
% col 5=pos
% col 6=vel
% col end = 0,1 0-> downsweep, 1-> upsweep
for i=1:length(ufreq)
    figure(floor(ufreq(i)*1000))
    ind1=find(posmax{i}(:,end)==1);
    ind2=find(posmax{i}(:,end)==0);
    ind3=find(constphase{i}{sec}(:,end)==1);
    ind4=find(constphase{i}{sec}(:,end)==0);
    ind5=find(constphase{i}{secsym}(:,end)==1);
    ind6=find(constphase{i}{secsym}(:,end)==0);
    indinup=find(constphase{i}{vpk}(:,end)==1);
    indindwn=find(constphase{i}{vpk}(:,end)==0);

    subplot(4,1,1)
    plot(constphase{i}{sec}(ind3,1),constphase{i}{sec}(ind3,6),'b.', ...
         constphase{i}{secsym}(ind5,1),constphase{i}{secsym}(ind5,6),'c.')
    axis([xmin xmax -2 4])

    subplot(4,1,2)
    plot(constphase{i}{sec}(ind4,1),constphase{i}{sec}(ind4,6),'r.', ...
         constphase{i}{secsym}(ind6,1),constphase{i}{secsym}(ind6,6),'m.')
    axis([xmin xmax -2 4])

    subplot(4,1,3)
    plot(posmax{i}(ind1,1),posmax{i}(ind1,5),'b.',posmax{i}(ind2,1), ...
         posmax{i}(ind2,5),'r.')
    axis([xmin xmax -Inf Inf])

    % Plot current at the section
    subplot(4,1,4)
    plot(constphase{i}{sec}(ind3,1),constphase{i}{sec}(ind3,4),'b.', ...
         constphase{i}{secsym}(ind5,1),constphase{i}{secsym}(ind5,4),'c.', ...
         constphase{i}{sec}(ind4,1),constphase{i}{sec}(ind4,4),'r.', ...
         constphase{i}{secsym}(ind6,1),constphase{i}{secsym}(ind6,4),'m.')
    axis([xmin xmax -2 4])
    %     % Plot input voltage at the terminals subplot(4,1,4)
    %     plot(constphase{i}{vpk}(indinup,1),constphase{i}{vpk}(indinup,4),
    %     'b.',constphase{i}{vpk}(indindwn,1),constphase{i}{vpk}(indindwn,4),'r.')
    %     axis([5.2 6.2 -Inf Inf])
end


indevo=find(freq==6.1 & vpp==5.92);
```

```
61
62 % for i=1:length(ufreq)
63 %     figure(floor(ufreq(i)*100))
64 %     ind1=find(posmax{i}(:,end)==1);
65 %     ind2=find(posmax{i}(:,end)==0);
66 %
67 %     subplot(3,1,1)
68 %     plot(velmax{i}(ind1,1),velmax{i}(ind1,6),'b.')
69 %     axis([2 8 -2 3])
70 %
71 %     subplot(3,1,2)
72 %     plot(velmax{i}(ind2,1),velmax{i}(ind2,6),'r.')
73 %     axis([2 8 -2 3])
74 %
75 %     subplot(3,1,3) plot(posmax{i}(ind1,1),posmax{i}(ind1,5),'b.',
76 %     posmax{i}(ind2,1),posmax{i}(ind2,5),'r.')  axis([2 8 -Inf Inf])
77 % end
78
79 % NOTE: There is a symmetry that corresponds to a mirroring of current
80 % and a time shift in the input. For this reason, show phase sections in
81 % increments of pi
```

```
1  % Bryan Wilcox
2  % plottraj6100nonsym.m
3
4  % extract and plot trajectory and discrete fft
5
6  data=load('20100427_203411_06100_05920_0.dat');
7  T=1/6.1; % calculate the period
8  numch=4; % number of data channels acquired
9  dt=data(2,1)-data(1,1); % get the sampling rate
10 incol=2;  % column of the input
11
12 %% Pull phase section data
13 %% Time shift data set to index input voltage as sin input
14 for j=1:(length(data(:,1))-1)
15     % looking for zero crossing in the increasing direction
16     if data(j,incol)<0 && data(j,incol)*data(j+1,incol)<0
17         %% zero index the time to make input a sin wave
18         %% use linear interpolation to locate t=0
19         %% start of sine wave is between j and j+1
20         tshift=interp1([data(j,incol) data(j+1,incol)],[data(j,1), ...
21                             data(j+1,1)],0);
22         data(:,1)=data(:,1)-tshift; % zero index the time
23         data=data(j:end,:); % remove junk prior to t=0;
24         break
25     end
26 end
27
28 %        for a=1:length(phasefrac)
29 runphasedat=[];
30 %% Collect data at constant phase Poincare sections
31 %% Generate array of time stamps on the available zero phase sections
32 tphase=0:T:data(end,1);
33 runphasedat0=[tphase(1:end-1)' zeros(length(tphase)-1,numch)];
34 runphasedat1=[(tphase(1:end-1)+T/4)' zeros(length(tphase)-1,numch)];
35 runphasedat2=[(tphase(1:end-1)+T/2)' zeros(length(tphase)-1,numch)];
36 runphasedat3=[(tphase(1:end-1)+3*T/4)' zeros(length(tphase)-1,numch)];
37 len=length(tphase);
38
39 for m=1:len-1 % index over the periods
40     %% Get the index for the first point beyond the time stamp
41     ind0=find(data(:,1)>tphase(m),1);
42     for n=1:numch
```

```
        %% Interpolate data and save into cell array
        runphasedat0(m,n+1)=interp1([data(ind0-1,1) data(ind0,1)], ...
                                    [data(ind0-1,n+1) data(ind0,n+ ...
                                                          1)],tphase(m));
    end
    ind1=find(data(:,1)>tphase(m)+T/4,1);
    %% phase section lies between ind and ind-1
    for n=1:numch
        %% Interpolate data and save into cell array
        runphasedat1(m,n+1)=interp1([data(ind1-1,1) data(ind1,1)], ...
                                    [data(ind1-1,n+1) data(ind1,n+ ...
                                                          1)],tphase(m)+T/4);
    end
    ind2=find(data(:,1)>tphase(m)+T/2,1);
    %% phase section lies between ind and ind-1
    for n=1:numch
        %% Interpolate data and save into cell array
        runphasedat2(m,n+1)=interp1([data(ind2-1,1) data(ind2,1)], ...
                                    [data(ind2-1,n+1) data(ind2,n+ ...
                                                          1)],tphase(m)+T/2);
    end
    ind3=find(data(:,1)>tphase(m)+3*T/4,1);
    %% phase section lies between ind and ind-1
    for n=1:numch
        %% Interpolate data and save into cell array
        runphasedat3(m,n+1)=interp1([data(ind3-1,1) data(ind3,1)], ...
                                    [data(ind3-1,n+1) data(ind3,n+ ...
                                                          1)],tphase(m)+3*T/4);
    end
end

Vin=mean(abs([runphasedat1(:,2);runphasedat3(:,2)]))

ind3T=find(data(:,1)≥3*T,1);
time3T=data(1:ind3T,1);

pos=data(:,4)*0.0791868*0.0254;
pos3T=pos(1:ind3T);
vel=-data(:,5)*25/1000;
vel3T=vel(1:ind3T);
cur=data(:,3);
cur3T=cur(1:ind3T);
vin=data(:,2);
vin3T=vin(1:ind3T);

pos0=runphasedat0(:,4)*0.0791868*0.0254;
vel0=-runphasedat0(:,5)*25/1000;
cur0=runphasedat0(:,3);
vin0=runphasedat0(:,2);
time0=runphasedat0(:,1);

pospi=runphasedat2(:,4)*0.0791868*0.0254;
velpi=-runphasedat2(:,5)*25/1000;
curpi=runphasedat2(:,3);
vinpi=runphasedat2(:,2);
timepi=runphasedat2(:,1);

avg=mean(cur0);
dat=cur0-avg;
NFFT=length(cur0);
Fs=6.1;
f = Fs/2*linspace(0,1,NFFT/2);
CUR0=fft(dat,NFFT)/NFFT;
plotdata=abs([CUR0(1), 2*CUR0(2:NFFT/2)']/avg);

figure(1)
hold on
```

```
plot(f,plotdata,'r')

% Save off data
outdat=[f' plotdata'];
save('6100_fftnonsym.dat','-ascii','-double','outdat')

figure(2)
plot(vel,cur,'k.',vel0,cur0,'bo',velpi,curpi,'ro','MarkerSize',5)

figure(3)
plot3(pos,vel,cur,'k.',pos0,vel0,cur0,'bo',pospi,velpi,curpi,'ro','MarkerSize',2)

figure(4)
subplot(4,1,1)
plot(time3T,vin3T,'k.',time0(1:3),vin0(1:3),'bo',timepi(1:3),vinpi(1:3),'ro')
subplot(4,1,2)
plot(time3T,cur3T,'k.',time0(1:3),cur0(1:3),'bo',timepi(1:3),curpi(1:3),'ro')
subplot(4,1,3)
plot(time3T,pos3T,'k.',time0(1:3),pos0(1:3),'bo',timepi(1:3),pospi(1:3),'ro')
subplot(4,1,4)
plot(time3T,vel3T,'k.',time0(1:3),vel0(1:3),'bo',timepi(1:3),velpi(1:3),'ro')

% Save off data
outdat=[vel cur];
save('6100_vel_cur_nonsym.dat','-ascii','-double','outdat')

outdat=[vel0 cur0];
save('6100_sec0_nonsym.dat','-ascii','-double','outdat')

outdat=[velpi curpi];
save('6100_secpi_nonsym.dat','-ascii','-double','outdat')

%% Time evolution
outdat=[time3T vin3T];
save('6100_tevo_vin.dat','-ascii','-double','outdat')

outdat=[time3T cur3T];
save('6100_tevo_cur.dat','-ascii','-double','outdat')

outdat=[time3T pos3T*1000]; % scale into mm
save('6100_tevo_pos.dat','-ascii','-double','outdat')

outdat=[time3T vel3T];
save('6100_tevo_vel.dat','-ascii','-double','outdat')

outdat=[time0(1:3) vin0(1:3)];
save('6100_tevo_vin_sec0.dat','-ascii','-double','outdat')

outdat=[time0(1:3) cur0(1:3)];
save('6100_tevo_cur_sec0.dat','-ascii','-double','outdat')

outdat=[time0(1:3) pos0(1:3)*1000]; % scale into mm
save('6100_tevo_pos_sec0.dat','-ascii','-double','outdat')

outdat=[time0(1:3) vel0(1:3)];
save('6100_tevo_vel_sec0.dat','-ascii','-double','outdat')

outdat=[timepi(1:3) vinpi(1:3)];
save('6100_tevo_vin_secpi.dat','-ascii','-double','outdat')

outdat=[timepi(1:3) curpi(1:3)];
save('6100_tevo_cur_secpi.dat','-ascii','-double','outdat')

outdat=[timepi(1:3) pospi(1:3)*1000]; % scale into mm
save('6100_tevo_pos_secpi.dat','-ascii','-double','outdat')

outdat=[timepi(1:3) velpi(1:3)];
```

```
177 save('6100_tevo_vel_secpi.dat','-ascii','-double','outdat')
```

Appendix C

Matlab Simulation Files for Chapter 5

```
%% Bryan Wilcox
%% 04142010
%% simdriver.m
%% script to drive the simulation function to generate numerical data for
%% comparison to experiment.
superclean
sysid;            %load system parameters

% begfreq=7; % Hz
% endfreq=7; % Hz
% freqincr=0.05;
% freqHz=begfreq:freqincr:endfreq;

freqHz=[6.25,7,8];
freq=freqHz*2*pi/d.w0; % nondimensionalized

begV0=[4.5,3.0,1.5];
endV0=[5.5,5.5,5.5];
V0incr=0.001;
maxT=6; % Maximum periodicity to look for in swpsim
maxshots=150; % Maximum number of input phases to simulate
tol=1e-6;

%% DELETE the next two lines to run for real
% V0incr=1;
% maxshots=1; % Maximum number of input phases to simulate

[junk ind]=max(endV0-begV0);

savedICup=cell(length(freq),length(begV0(ind):V0incr:endV0(ind)));
savedICdwn=cell(length(freq),length(begV0(ind):V0incr:endV0(ind)));
simphase=cell(1,4); % saving 4 phase sections 0,pi/2,pi,3pi/2, see events.m
phaseevents=[1 5 6 7];
maxpos=[];

simconstphaseup=cell(1,length(freq));
simmaxposup=cell(1,length(freq));
simconstphasedwn=cell(1,length(freq));
simmaxposdwn=cell(1,length(freq));

%% First call to populate Y array
tic
x0=[0   1e-10  0   0   begV0(1)    freq(1)     p.zeta]'; % Initial condition
[T,Y,TE,YE,IE,x]=sim1per(x0,p,s);
toc

x0=x; % reset IC
i=0;
while i<length(freq)
    i=i+1;
```

```
51
52      %% GOING UP
53      simphase=cell(1,4); % saving 4 phase sections 0,pi/2,pi,3pi/4, see events.m
54      maxpos=[];
55      j=0;
56      V0dim=begV0(i):V0incr:endV0(i);
57      V0=V0dim/(d.w0^2*sqrt(2*d.m*d.beta1*d.beta2)); % nondimensionalized
58
59      while j<length(V0)
60          j=j+1;
61          x0=[x0(1:4);V0(j);freq(i);p.zeta];
62          [T,Y,TE,YE,IE,NT,x]=swpsim(x0,maxT,maxshots,tol,p,s,d);
63          x0=x;
64          for k=1:length(phaseevents)
65              ind=find(IE==phaseevents(k));
66              if phaseevents(k)==1
67                  zerophase{k}=[V0(j)*ones(length(ind),1) TE(ind) YE(ind,1:4)];
68              end
69              simphase{k}=[simphase{k}; V0(j)*ones(length(ind),1) TE(ind) YE(ind,1:4)];
70          end
71
72          ind2=find(IE==2); % find points of impact, this a max position
73          ind3=find(IE==3); % find local maxima
74
75          maxpos=[maxpos; V0(j)*ones(length(ind2),1) IE(ind2) TE(ind2) YE(ind2,1:4)];
76          maxpos=[maxpos; V0(j)*ones(length(ind3),1) IE(ind3) TE(ind3) YE(ind3,1:4)];
77
78          savedICup{i,j}=x0;
79
80          %% put up some debug plots
81          tmp1=simphase{1}(:,1)*(d.w0^2*sqrt(2*d.m*d.beta1*d.beta2));
82          tmp2=simphase{1}(:,4)*d.beta2*d.w0;
83          tmp3=simphase{3}(:,1)*(d.w0^2*sqrt(2*d.m*d.beta1*d.beta2));
84          tmp4=simphase{3}(:,4)*d.beta2*d.w0;
85          tmp5=simphase{1}(:,1)*(d.w0^2*sqrt(2*d.m*d.beta1*d.beta2));
86          tmp6=simphase{1}(:,5)*sqrt((2*d.m*d.w0^2*d.beta2^3)/d.beta1);
87          tmp7=simphase{3}(:,1)*(d.w0^2*sqrt(2*d.m*d.beta1*d.beta2));
88          tmp8=simphase{3}(:,5)*sqrt((2*d.m*d.w0^2*d.beta2^3)/d.beta1);
89
90          figure(round(freqHz(i)*1000))
91          subplot(2,1,1)
92          plot(tmp1,tmp2,'r.',tmp3,tmp4,'m.')
93          subplot(2,1,2)
94          plot(tmp5,tmp6,'r.',tmp7,tmp8,'m.')
95          drawnow
96      end
97      simconstphaseup{i}=simphase;
98      simmaxposup{i}=maxpos;
99      save
100     %% END GOING UP
101
102
103     %% GOING DOWN
104     simphase=cell(1,4); % saving 4 phase sections 0,pi/2,pi,3pi/4, see events.m
105     maxpos=[];
106     j=0;
107     V0dim=endV0(i):-V0incr:begV0(i);
108     V0=V0dim/(d.w0^2*sqrt(2*d.m*d.beta1*d.beta2)); % nondimensionalized
109
110     while j<length(V0)
111         j=j+1;
112
113         x0=[x0(1:4);V0(j);freq(i);p.zeta];
114         [T,Y,TE,YE,IE,NT,x]=swpsim(x0,maxT,maxshots,tol,p,s,d);
115         x0=x;
116
117         for k=1:length(phaseevents)
```

```
            ind=find(IE==phaseevents(k));
            if phaseevents(k)==1
                zerophase{k}=[V0(j)*ones(length(ind),1) TE(ind) YE(ind,1:4)];
            end
            simphase{k}=[simphase{k}; V0(j)*ones(length(ind),1) TE(ind) YE(ind,1:4)];
        end

        ind2=find(IE==2); % find points of impact, this a max position
        ind3=find(IE==3); % find local maxima

        maxpos=[maxpos; V0(j)*ones(length(ind2),1) IE(ind2) TE(ind2) YE(ind2,1:4)];
        maxpos=[maxpos; V0(j)*ones(length(ind3),1) IE(ind3) TE(ind3) YE(ind3,1:4)];

        savedICdwn{i,j}=x0;

        %% put up some debug plots
        tmp1=simphase{1}(:,1)*(d.w0^2*sqrt(2*d.m*d.beta1*d.beta2));
        tmp2=simphase{1}(:,4)*d.beta2*d.w0;
        tmp3=simphase{3}(:,1)*(d.w0^2*sqrt(2*d.m*d.beta1*d.beta2));
        tmp4=simphase{3}(:,4)*d.beta2*d.w0;
        tmp5=simphase{1}(:,1)*(d.w0^2*sqrt(2*d.m*d.beta1*d.beta2));
        tmp6=simphase{1}(:,5)*sqrt((2*d.m*d.w0^2*d.beta2^3)/d.beta1);
        tmp7=simphase{3}(:,1)*(d.w0^2*sqrt(2*d.m*d.beta1*d.beta2));
        tmp8=simphase{3}(:,5)*sqrt((2*d.m*d.w0^2*d.beta2^3)/d.beta1);

        figure(round(freqHz(i)*1000))
        subplot(2,1,1)
        plot(tmp1,tmp2,'r.',tmp3,tmp4,'m.')
        subplot(2,1,2)
        plot(tmp5,tmp6,'r.',tmp7,tmp8,'m.')
        drawnow
    end
    simconstphasedwn{i}=simphase;
    simmaxposdwn{i}=maxpos;
    save
    %% END GOING DOWN
end

% %% Generate dimensional data to compare with experiment
% num.time=T/d.w0;
% num.pos=Y(:,1)*d.beta2;
% num.vel=Y(:,2)*d.beta2*d.w0;
% num.cur=Y(:,3)*sqrt((2*d.m*d.w0^2*d.beta2^3)/d.beta1);
% figure(1)
% clf
% plot(num.time,num.pos,'r',[num.time(1) num.time(end)],[d.delta d.delta],'k')
% ylabel('Position (m)')
```

```
function [T,Y,TE,YE,IE,x0]=sim1per(x,p,s)

% Bryan Wilcox
% sim1per.m
%% Returns a trajectory from the IC to the phase=0 surface
%%%%%%%%%%%%%%%%%%%%%%%%%%%%%%%%%%%%%%%%%%%%%%%%%%%%%%%%%%%%%%%%%%%%%%%%%%%%%%%
%% This stuff really shouldn't be here I don't think. It should be passed
%% as part of a problem definition structure.

FUNC=@diffeq; % declare the vector field function

tstart=0;
% make sure plenty of sim time to cover max. periodicity
tfinal=(s.maxper+1)*pi/x(s.freq);
x0=reshape(x,s.dim,1);
Px0=eye(s.dim);
```

```
17
18  options=odeset('RelTol',1e-8,'AbsTol',1e-8,'Events',@events);
19  %%%%%%%%%%%%%%%%%%%%%%%%%%%%%%%%%%%%%%%%%%%%%%%%%%%%%%%%%%%%%%%%%%%%%%%%%%%%
20  % save calculations
21  dim2=s.dim^2;
22  jacbeg=s.dim+1;
23  jacend=s.dim+dim2;
24
25  T=[];
26  Y=[];
27  TE=[];
28  YE=[];
29  IE=[];
30
31  modind=0;
32  while tstart<tfinal
33      [t,y,te,ye,ie]=ode45(FUNC,[tstart tfinal],[x0;reshape(Px0',dim2,1)],options,p);
34      tstart=t(end);
35
36      T=[T;t];
37      Y=[Y;y];
38      TE=[TE;te];
39      YE=[YE;ye];
40      IE=[IE;ie];
41
42      x0=y(end,1:s.dim)';
43      dphidx=reshape(y(end,jacbeg:jacend),s.dim,s.dim)';
44
45      if ¬isempty(ie)
46          if ie(end)==1
47
48              dh=[0,0,0,-1,0,0,0]; % jacobian of the event function
49              x0(4)=x0(4)-2*pi; % mod. phase
50              % get vector field, post mapping
51              temp=FUNC(te(end),[x0;reshape(eye(s.dim),dim2,1)],p);
52              f=temp(1:s.dim); % isolate state vector field
53              gx=eye(s.dim); % jacobian of of event map
54              % project coord jacobian onto event surface
55              Px0=gx*(eye(s.dim)-f*dh/(dh*f))*dphidx;
56              % give a frendly bump to avoid false positive on restart
57              x0=x0+1e-12*f;
58
59              % Break when phase=0 surface reached. To get one full period
60              % this implictly assumes that the initial condition was on (or
61              % very near) the phase=0 surface
62              break
63
64          % IMPACT event
65          elseif ie(end)==2
66              %display('contact')
67              dh=[-1,0,0,0,0,0,0];
68              x0(2)=-p.e*x0(2);
69              temp=FUNC(te(end),[x0;reshape(eye(s.dim),dim2,1)],p);
70              f=temp(1:s.dim);
71              gx=[1,0,0,0,0,0,0;
72                  0,-p.e,0,0,0,0,0;
73                  0,0,1,0,0,0,0;
74                  0,0,0,1,0,0,0;
75                  0,0,0,0,1,0,0;
76                  0,0,0,0,0,1,0
77                  0,0,0,0,0,0,1];
78              Px0=gx*(eye(s.dim)-f*dh/(dh*f))*dphidx;
79              x0=x0+1e-12*f;
80
81          % local MAX position (velocity goes (+) to (-)
82          elseif ie(end)==3
83              dh=[0,1,0,0,0,0,0];
```

```
            temp=FUNC(te(end),[x0;reshape(eye(s.dim),dim2,1)],p);
            f=temp(1:s.dim);
            Px0=(eye(s.dim)-f*dh/(dh*f))*dphidx;
            x0=x0+1e-12*f;

        % local MIN postion (velocity goes (-) to (+)
        elseif ie(end)==4
            dh=[0,-1,0,0,0,0,0];
            temp=FUNC(te(end),[x0;reshape(eye(s.dim),dim2,1)],p);
            f=temp(1:s.dim);
            Px0=(eye(s.dim)-f*dh/(dh*f))*dphidx;
            x0=x0+1e-12*f;

        elseif ie(end)==5
            % phase=pi/2
            dh=[0,0,0,-1,0,0,0]; % jacobian of the event function
            % get vector field, post mapping
            temp=FUNC(te(end),[x0;reshape(eye(s.dim),dim2,1)],p);
            f=temp(1:s.dim); % isolate state vector field
            gx=eye(s.dim); % jacobian of of event map
            % project coord jacobian onto event surface
            Px0=gx*(eye(s.dim)-f*dh/(dh*f))*dphidx;
            % give a frendly bump to avoid false positive on restart
            x0=x0+1e-12*f;

        elseif ie(end)==6
            % phase=pi
            dh=[0,0,0,-1,0,0,0]; % jacobian of the event function
            % get vector field, post mapping
            temp=FUNC(te(end),[x0;reshape(eye(s.dim),dim2,1)],p);
            f=temp(1:s.dim); % isolate state vector field
            gx=eye(s.dim); % jacobian of of event map
            % project coord jacobian onto event surface
            Px0=gx*(eye(s.dim)-f*dh/(dh*f))*dphidx;
            % give a frendly bump to avoid false positive on restart
            x0=x0+1e-12*f;

        elseif ie(end)==7
            %phase=3*pi/4
            dh=[0,0,0,-1,0,0,0]; % jacobian of the event function
            % get vector field, post mapping
            temp=FUNC(te(end),[x0;reshape(eye(s.dim),dim2,1)],p);
            f=temp(1:s.dim); % isolate state vector field
            gx=eye(s.dim); % jacobian of of event map
            % project coord jacobian onto event surface
            Px0=gx*(eye(s.dim)-f*dh/(dh*f))*dphidx;
            % give a frendly bump to avoid false positive on restart
            x0=x0+1e-12*f;
        else
            error('shouldn''t be possible');
        end
    end
end
```

```
function [Trtn,Yrtn,TErtn,YErtn,IErtn,NT,x]=swpsim(x,maxT,maxshots,tol,p,s,d)

% Bryan Wilcox
% swpsim.m

% give this a starting pt, the max periodicity to look for, max number
% of input periods, maxshots, to simulate before giving up, convergence
% tolerance it either returns a periodic orbit indicating the
% periodicity, or it returns the last 100 periods of simulation
T=[];Y=[];TE=[];YE=[];IE=[];
```

```
11
12 % simulate with sim1per.m to get a starting point on the phase=0
13 % surface
14 % figure(1)
15 % clf
16 % hold on
17 [t,y,te,ye,ie,x0]=sim1per(x,p,s);
18 %% append new data to saved data arrays
19 % plot(t,y(:,2))
20 % drawnow
21 T=[T;t];
22 Y=[Y;y];
23 TE=[TE;te];
24 YE=[YE;ye];
25 IE=[IE;ie];
26
27 x=x0; % reset IC
28
29 shots=0;
30 while shots≤maxshots
31     shots=shots+1;
32     [t,y,te,ye,ie,x0]=sim1per(x,p,s);
33 %     plot(t,y(:,2))
34 %     drawnow
35     T=[T;t];
36     Y=[Y;y];
37     TE=[TE;te];
38     YE=[YE;ye];
39     IE=[IE;ie];
40     x=x0;
41     NT=0;
42     ind=find(IE==1);
43     len=length(ind);
44     % start at end of index of phase events and work backward until max
45     % periodicity is reached or run out of data to work with
46     while NT<maxT && NT<(len-1)
47         NT=NT+1;
48         convtest=norm(YE(ind(end),1:4)-YE(ind(end-NT),1:4));
49         if convtest<tol
50             % Orbit with periodicity NT found. Return to invoking function
51             % Send back trajectory information for NT periods.
52
53             indrtn=find(T==TE(ind(end-NT)),1)+1;
54             % find time stamp exactly equal to the time of the event.
55             % advance one index to obtain the point that has had the phase
56             % reset to zero and had the slight bump added to get it off the
57             % event surface
58             % safety check to make sure the phase is very close to zero
59             if Y(indrtn,4) > 1e-10
60                 error('phase should be zero and is not: periodic')
61             end
62
63 %             if length(indrtn)>1
64 %                 error('too many indices returned by find for rtn trajectory')
65 %             %indrtn=indtemp(2);
66 %             end
67             display('periodic')
68             Trtn=T(indrtn:end);
69             Yrtn=Y(indrtn:end,:);
70             TErtn=TE(ind(end-NT)+1:end);
71             YErtn=YE(ind(end-NT)+1:end,:);
72             IErtn=IE(ind(end-NT)+1:end);
73             return
74         end
75     end
76 end
77
```

```
%% Did not find a periodic orbit up to maxT within the specified number
%% of tries, return last 100 periods or the entire trajectory, whichever is
%% less
display('Not periodic')
NT=0; % set to zero to indicates no periodic orbit found
ind=find(IE==1);

if length(ind)>100
    indrtn=find(T==TE(ind(end-100)),1)+1;
    if Y(indrtn,4) > 1e-10
        error('phase should be zero and is not: not periodic')
    end
    Trtn=T(indrtn:end);
    Yrtn=Y(indrtn:end,:);
    TErtn=TE(ind(end-100):end);
    YErtn=YE(ind(end-100):end,:);
    IErtn=IE(ind(end-100):end);
else
    Trtn=T;
    Yrtn=Y;
    TErtn=TE;
    YErtn=YE;
    IErtn=IE;
end
```

```
%% Untitled.m
%% 04142010
%% General purpose script for messing around with simulations. Useful for
%% finding starting points for continuation runs.

%% Useful initial conditions
x0=[0   1e-10  0   0   in.V    in.freq     p.zeta]'; % Initial condition
x0=[-0.328205614790196  -0.008008223178345   0.522467536665541 ...
    0.454682523675993    in.V    in.freq     p.zeta]'; % pregrazing

sysid;            %load system parameters

numperiods=1;
% Inputs
in.Hz = 6.3; % Input frequency in Hz
in.freq = 2*pi*in.Hz/d.w0; % ND input circular frequency
in.volt = 4;      % Dimensional input voltage amplitude
%in.volt = 3.55;      % Dimensional input voltage amplitude
in.V = in.volt/(d.w0^2*sqrt(2*d.m*d.beta1*d.beta2)); % ND input voltage

%x0=[Y(end,1:s.coords),in.V,in.freq,p.zeta];
tic
[T,Y,TE,YE,IE]=simulate(x0,p,s,d);
%% Generate dimensional data to compare with experiment
num.time=T/d.w0;
num.pos=Y(:,1)*d.beta2;
num.vel=Y(:,2)*d.beta2*d.w0;
num.cur=Y(:,3)*sqrt((2*d.m*d.w0^2*d.beta2^3)/d.beta1);
figure(1)
clf
plot(num.time,num.pos,'r',[num.time(1) num.time(end)],[d.delta d.delta],'k')
ylabel('Position (m)')

figure(2)
clf
plot(num.vel(end-5000:end),num.cur(end-5000:end),'r')
xlabel('Velocity (m/s)')
ylabel('Current (A)')
toc
```

```
40
41 % Prep for continuation
42 getNper;
```

```
1  %% sysid.m
2  %% calculation of non-dim params based on dim values in paper
3  %% d-struct holds dimensional device parameters
4  %% p-struct holds nondim parameter values for use in simulation
5  %% s-struct holds simulation specific information
6
7  %% From system identification
8  LDSsens=0.0791868; % [in/V] LDS sensitivity
9  d.d=2.382*LDSsens*0.0254;   % [V]->[in]->[m]
10 d.delta=0.55*LDSsens*0.0254;% [in]->[m]
11 d.e=0.866;          % averaged from experiment, data from JCND paper
12 d.m=0.6462;         % [kg]
13 d.zeta=0.01626;     % [] From free response
14 d.w0=95.94;         % [rad/s]
15 d.k=d.w0^2*d.m;     % [N/m]
16 d.beta1=1.902e-5;   % [H m]
17 d.beta2=1.631e-3;   % [m]
18 d.L_l=10.55e-3;     % [H]
19 d.R=1.390;          % [Ohm]
20
21 %% Calculate nondim params
22 p.zeta=d.zeta;
23 p.alpha1=d.L_l*d.beta2/d.beta1;
24 p.alpha2=d.R*d.beta2/(d.beta1*d.w0);
25 p.d=d.d/d.beta2;
26 p.delta=d.delta/d.beta2;
27 p.e=d.e;
28
29 %% Set simulation params
30 % s.dim=6;
31 % s.coords=4;
32 % s.contvar=5;
33 % s.maxNRiter=5;
34 % s.maxper=6;
35 % s.NRtol=1e-8;
36 % s.NRmaxcondnum=1e20;
37
38 s.dim=7;        % dimension of the system of ode's, number of state variables
39 s.coords=4;     % number of state var's corresponding to physical coordinates
40 s.freq=6;       % index of frequency in the state array
41 s.contvar=7;    % index of continuation variable
42 s.maxNRiter=5;  % maximum Newton Raphson iterations
43 s.maxper=10;    % maximum periodicity to look for
44 s.NRtol=1e-8;   % convergence criteria for Newton Raphson iterations
45 s.NRmaxcondnum=1e20;    % Maximum condition number for Newton Raphson routine
```

```
1  function [T,Y,TE,YE,IE]=simulate(x,p,s,d)
2  %% simulate.m
3  %%%%%%%%%%%%%%%%%%%%%%%%%%%%%%%%%%%%%%%%%%%%%%%%%%%%%%%%%%%%%%%%%%%%%%%%%%%%
4  %% This stuff really shouldn't be here I don't think. It should be passed
5  %% as part of a problem definition structure.
6
7  FUNC=@diffeq; % declare the vector field function
8
9  tstart=0;
10 tfinal=5*d.w0;
11 x0=reshape(x,s.dim,1);
```

```
Px0=eye(s.dim);

options=odeset('RelTol',1e-8,'AbsTol',1e-8,'Events',@events);
%%%%%%%%%%%%%%%%%%%%%%%%%%%%%%%%%%%%%%%%%%%%%%%%%%%%%%%%%%%%%%%%%%%%%%%%%%%%%%%
% save calculations
dim2=s.dim^2;
jacbeg=s.dim+1;
jacend=s.dim+dim2;

T=[];
Y=[];
TE=[];
YE=[];
IE=[];

while tstart<tfinal
    [t,y,te,ye,ie]=ode45(FUNC,[tstart tfinal],...
                         [x0;reshape(Px0',dim2,1)],options,p);
    tstart=t(end);

    T=[T;t];
    Y=[Y;y];
    TE=[TE;te];
    YE=[YE;ye];
    IE=[IE;ie];

    x0=y(end,1:s.dim)';
    dphidx=reshape(y(end,jacbeg:jacend),s.dim,s.dim)';

    if ¬isempty(ie)

        if ie(end)==1
            % PHASE=0 event
            dh=[0,0,0,-1,0,0,0]; % jacobian of the event function
            x0(4)=x0(4)-2*pi; % mod. phase
            % get vector field, post mapping
            temp=FUNC(te(end),[x0;reshape(eye(s.dim),dim2,1)],p);
            f=temp(1:s.dim); % isolate state vector field
            gx=eye(s.dim); % jacobian of of event map
            % project coord jacobian onto event surface
            Px0=gx*(eye(s.dim)-f*dh/(dh*f))*dphidx;
            % give a frendly bump to avoid false positive on restart
            x0=x0+1e-12*f;

        elseif ie(end)==2
            % IMPACT event
            %display('contact')
            dh=[-1,0,0,0,0,0,0];
            x0(2)=-p.e*x0(2);
            temp=FUNC(te(end),[x0;reshape(eye(s.dim),dim2,1)],p);
            f=temp(1:s.dim);
            gx=[1,0,0,0,0,0,0;
                0,-p.e,0,0,0,0,0;
                0,0,1,0,0,0,0;
                0,0,0,1,0,0,0;
                0,0,0,0,1,0,0;
                0,0,0,0,0,1,0
                0,0,0,0,0,0,1];
            Px0=gx*(eye(s.dim)-f*dh/(dh*f))*dphidx;
            x0=x0+1e-12*f;

        elseif ie(end)==3
            % local MAX position (velocity goes (+) to (-)
            dh=[0,1,0,0,0,0,0];
            temp=FUNC(te(end),[x0;reshape(eye(s.dim),dim2,1)],p);
            f=temp(1:s.dim);
            Px0=(eye(s.dim)-f*dh/(dh*f))*dphidx;
```

```
            x0=x0+1e-12*f;

        elseif ie(end)==4
            % local MIN postion (velocity goes (-) to (+)
            dh=[0,-1,0,0,0,0,0];
            temp=FUNC(te(end),[x0;reshape(eye(s.dim),dim2,1)],p);
            f=temp(1:s.dim);
            Px0=(eye(s.dim)-f*dh/(dh*f))*dphidx;
            x0=x0+1e-12*f;

        elseif ie(end)==5
            % phase=pi/2
            dh=[0,0,0,-1,0,0,0]; % jacobian of the event function
            % get vector field, post mapping
            temp=FUNC(te(end),[x0;reshape(eye(s.dim),dim2,1)],p);
            f=temp(1:s.dim); % isolate state vector field
            gx=eye(s.dim); % jacobian of of event map
            % project coord jacobian onto event surface
            Px0=gx*(eye(s.dim)-f*dh/(dh*f))*dphidx;
            % give a frendly bump to avoid false positive on restart
            x0=x0+1e-12*f;

        elseif ie(end)==6
            % phase=pi
            dh=[0,0,0,-1,0,0,0]; % jacobian of the event function
            % get vector field, post mapping
            temp=FUNC(te(end),[x0;reshape(eye(s.dim),dim2,1)],p);
            f=temp(1:s.dim); % isolate state vector field
            gx=eye(s.dim); % jacobian of of event map
            % project coord jacobian onto event surface
            Px0=gx*(eye(s.dim)-f*dh/(dh*f))*dphidx;
            % give a frendly bump to avoid false positive on restart
            x0=x0+1e-12*f;

        elseif ie(end)==7
            %phase=3*pi/4
            dh=[0,0,0,-1,0,0,0]; % jacobian of the event function
            % get vector field, post mapping
            temp=FUNC(te(end),[x0;reshape(eye(s.dim),dim2,1)],p);
            f=temp(1:s.dim); % isolate state vector field
            gx=eye(s.dim); % jacobian of of event map
            % project coord jacobian onto event surface
            Px0=gx*(eye(s.dim)-f*dh/(dh*f))*dphidx;
            % give a frendly bump to avoid false positive on restart
            x0=x0+1e-12*f;

        else
            error('shouldn''t be possible');
        end
    end
end
```

```
function dydt = diffeq(t,y,p)
%% diffeq.m

x1=y(1); % position
x2=y(2); % velocity
x3=y(3); % current
x4=y(4); % input phase
x5=y(5); % input amplitude
x6=y(6); % input frequency
x7=y(7); % damping (zeta)

dim=7;
```

```
f=zeros(dim,1);

f(1)=x2;
f(2)=-x1-2*x7*x2+x3^2/(1+p.d-x1)^2;
f(3)=(x5*sin(x4)-(p.alpha2+x2/(1+p.d-x1)^2)*x3)/(p.alpha1+1/(1+p.d-x1));
f(4)=x6;

df=zeros(dim,dim);

df(1,2)=1;
df(2,1)=-1+2*x3^2/(1+p.d-x1)^3;
df(2,2)=-2*x7;
df(2,3)=2*x3/(1+p.d-x1)^2;
df(2,7)=-2*x2;
df(3,1)=((p.alpha2*(1+p.d-x1)^2-(1+2*p.alpha1*(1+p.d-x1))*x2)*x3-(1+...
    p.d-x1)^2*x5*sin(x4))/((1+p.alpha1*(1+p.d-x1))^2*(1+p.d-x1)^2);
df(3,2)=-(x3/((1+p.alpha1*(1+p.d-x1))*(1+p.d-x1)));
df(3,3)=-((p.alpha2+x2/(1+p.d-x1)^2)/(p.alpha1+1/(1+p.d-x1)));
df(3,4)=(x5*cos(x4))/(p.alpha1+1/(1+p.d-x1));
df(3,5)=sin(x4)/(p.alpha1+1/(1+p.d-x1));
df(4,6)=1;


dydt=zeros(dim+dim^2,1);

for i=1:dim
    dydt(i)=f(i);
end
for i=1:dim
    for j=1:dim
        sum=0;
        for k=1:dim
            sum=sum+df(i,k)*y(dim+(k-1)*dim+j);
        end
        dydt(dim+(i-1)*dim+j)=sum;
    end
end
```

```
function [value,isterminal,direction] = events(t,y,p)
%% events.m
x1=y(1); % position
x2=y(2); % velocity
x3=y(3); % current
x4=y(4); % input phase
x5=y(5); % input amplitude
x6=y(6); % input frequency
x7=y(7); % damping (zeta)


value = [2*pi-x4,(p.delta-x1),x2,-x2,pi/2-x4,pi-x4,3*pi/2-x4];
isterminal = [1,1,1,1,1,1,1];
direction = [-1,-1,-1,-1,-1,-1,-1];
```

```
%% getNper.m

x=Y(end,1:s.dim);

[TNper,YNper,TENper,YENper,IENper,x0]=simNper(x,numperiods,p,s);

clear Nper
% Nper struct in dimensional form
```

```
Nper.time=TNper/d.w0;
Nper.pos=YNper(:,1)*d.beta2;
Nper.vel=YNper(:,2)*d.beta2*d.w0;
Nper.cur=YNper(:,3)*sqrt((2*d.m*d.w0^2*d.beta2^3)/d.beta1);

Nper.time=TNper;
Nper.pos=YNper(:,1);
Nper.vel=YNper(:,2);
Nper.cur=YNper(:,3);

figure(20)
plot3(Nper.pos,Nper.vel,Nper.cur,'r',Nper.pos(1),Nper.vel(1), ...
      Nper.cur(1),'or',Nper.pos(end),Nper.vel(end),Nper.cur(end),'og')
xlabel('Position')
ylabel('Velocity')% (m/s)')
zlabel('Current')% (A)')
```

```
function [T,Y,TE,YE,IE,x0]=simNper(x,numperiods,p,s)
%% simNper.m
%% Returns the trajectory for the first full numperiod's of the
%% input starting from the first time the phase is modded after the initial
%% call to the function.
%%%%%%%%%%%%%%%%%%%%%%%%%%%%%%%%%%%%%%%%%%%%%%%%%%%%%%%%%%%%%%%%%%%%%%%%%%%
%% This stuff really shouldn't be here I don't think. It should be passed
%% as part of a problem definition structure.

FUNC=@diffeq; % declare the vector field function

tstart=0;
% make sure plenty of sim time to cover max. periodicity
tfinal=(s.maxper+1)*pi/x(s.freq);
x0=reshape(x,s.dim,1);
Px0=eye(s.dim);

options=odeset('RelTol',1e-8,'AbsTol',1e-8,'Events',@events);
%%%%%%%%%%%%%%%%%%%%%%%%%%%%%%%%%%%%%%%%%%%%%%%%%%%%%%%%%%%%%%%%%%%%%%%%%%%
% save calculations
dim2=s.dim^2;
jacbeg=s.dim+1;
jacend=s.dim+dim2;

T=[];
Y=[];
TE=[];
YE=[];
IE=[];

modind=0;
while tstart<tfinal
    [t,y,te,ye,ie]=ode45(FUNC,[tstart tfinal],[x0;reshape(Px0',dim2,1)],options,p);
    tstart=t(end);

    T=[T;t];
    Y=[Y;y];
    TE=[TE;te];
    YE=[YE;ye];
    IE=[IE;ie];

    x0=y(end,1:s.dim)';
    dphidx=reshape(y(end,jacbeg:jacend),s.dim,s.dim)';

    if ~isempty(ie)
        if ie(end)==1

```

```
48              dh=[0,0,0,-1,0,0,0]; % jacobian of the event function
49              x0(4)=x0(4)-2*pi; % mod. phase
50              % get vector field, post mapping
51              temp=FUNC(te(end),[x0;reshape(eye(s.dim),dim2,1)],p);
52              f=temp(1:s.dim); % isolate state vector field
53              gx=eye(s.dim); % jacobian of of event map
54              % project coord jacobian onto event surface
55              Px0=gx*(eye(s.dim)-f*dh/(dh*f))*dphidx;
56              % give a frendly bump to avoid false positive on restart
57              x0=x0+1e-12*f;
58
59              if modind == numperiods
60                  break
61              end
62              % Clean out saved trajectory info if first mod, only happens
63              % once
64              if modind == 0
65                  T=[];Y=[];TE=[];YE=[];IE=[];
66              end
67              modind=modind+1;
68
69          % IMPACT event
70          elseif ie(end)==2
71              %display('contact')
72              dh=[-1,0,0,0,0,0,0];
73              x0(2)=-p.e*x0(2);
74              temp=FUNC(te(end),[x0;reshape(eye(s.dim),dim2,1)],p);
75              f=temp(1:s.dim);
76              gx=[1,0,0,0,0,0,0;
77                  0,-p.e,0,0,0,0,0;
78                  0,0,1,0,0,0,0;
79                  0,0,0,1,0,0,0;
80                  0,0,0,0,1,0,0;
81                  0,0,0,0,0,1,0
82                  0,0,0,0,0,0,1];
83              Px0=gx*(eye(s.dim)-f*dh/(dh*f))*dphidx;
84              x0=x0+1e-12*f;
85
86          % local MAX position (velocity goes (+) to (-)
87          elseif ie(end)==3
88              dh=[0,1,0,0,0,0,0];
89              temp=FUNC(te(end),[x0;reshape(eye(s.dim),dim2,1)],p);
90              f=temp(1:s.dim);
91              Px0=(eye(s.dim)-f*dh/(dh*f))*dphidx;
92              x0=x0+1e-12*f;
93
94          % local MIN postion (velocity goes (-) to (+)
95          elseif ie(end)==4
96              dh=[0,-1,0,0,0,0,0];
97              temp=FUNC(te(end),[x0;reshape(eye(s.dim),dim2,1)],p);
98              f=temp(1:s.dim);
99              Px0=(eye(s.dim)-f*dh/(dh*f))*dphidx;
100             x0=x0+1e-12*f;
101
102         elseif ie(end)==5
103             % phase=pi/2
104             dh=[0,0,0,-1,0,0,0]; % jacobian of the event function
105             % get vector field, post mapping
106             temp=FUNC(te(end),[x0;reshape(eye(s.dim),dim2,1)],p);
107             f=temp(1:s.dim); % isolate state vector field
108             gx=eye(s.dim); % jacobian of of event map
109             % project coord jacobian onto event surface
110             Px0=gx*(eye(s.dim)-f*dh/(dh*f))*dphidx;
111             % give a frendly bump to avoid false positive on restart
112             x0=x0+1e-12*f;
113
114         elseif ie(end)==6
```

```
            % phase=pi
            dh=[0,0,0,-1,0,0,0]; % jacobian of the event function
            % get vector field, post mapping
            temp=FUNC(te(end),[x0;reshape(eye(s.dim),dim2,1)],p);
            f=temp(1:s.dim); % isolate state vector field
            gx=eye(s.dim); % jacobian of of event map
            % project coord jacobian onto event surface
            Px0=gx*(eye(s.dim)-f*dh/(dh*f))*dphidx;
            % give a frendly bump to avoid false positive on restart
            x0=x0+1e-12*f;

        elseif ie(end)==7
            %phase=3*pi/4
            dh=[0,0,0,-1,0,0,0]; % jacobian of the event function
            % get vector field, post mapping
            temp=FUNC(te(end),[x0;reshape(eye(s.dim),dim2,1)],p);
            f=temp(1:s.dim); % isolate state vector field
            gx=eye(s.dim); % jacobian of of event map
            % project coord jacobian onto event surface
            Px0=gx*(eye(s.dim)-f*dh/(dh*f))*dphidx;
            % give a frendly bump to avoid false positive on restart
            x0=x0+1e-12*f;
        else
            error('shouldn''t be possible');
        end
    end
end
```

```
%% run.m

sysid;            % load system parameters
numperiods=1;     % input periodicity of the targeted trajectory

% Project along all dimensions except those staying constant. 'C' will
% have s.dim rows corresponding to the length of the state vector and
% will have one more column than the number of states corresponding to
% varying coordinates (not padded parameters)

C= [1,0,0,0,0;
    0,1,0,0,0;
    0,0,1,0,0;
    0,0,0,1,0;
    0,0,0,0,0;
    0,0,0,0,0;
    0,0,0,0,1];

h=-0.0001;
hmax=0.005;

[dFdx,eigs]=shootjac(x0,numperiods,p,s);

X=x0';
EIGS=eigs';
nv=null(dFdx);

ind=0;
while abs(h)>1e-8 %&& x0(5)<10
    % project out to the new guess (predictor step)
    xs=x0+h*C*nv;
    % Pass to NewtonRaphson to do predictor-corrector
    % return exiting state and number of iterations
    [x,n]=NewtonRaphson(@shootfun,@shootjac,x0,xs,nv,C,numperiods,p,s);

    % if too many iterations, decrease stepsize
```

```
    if n>s.maxNRiter
        h=h/2
    else
        % NR succeeded, try to increase (decrease) stepsize towards max
        if h>0
            h=min(hmax,h*1.5)
        else
            h=max(-hmax,h*1.5)
        end

        [tempT,tempY,tempTE,tempYE,tempIE]=simNper(x,numperiods,p,s);
        % Simulate one full period (can probably be combined with one of
        % the shooting calls)
        ind3=find(tempIE==3);

        [tempYE(ind3(end),1)*d.beta2,x(s.contvar)]
        % print peak position and last succesful cont. var. value
        clear tempT tempY tempTE tempYE tempIE ind3
        x0=x; % reset initial condition
        X=[X;x0']; % append to saved lists of states

        % Get jacobian at new IC
        [dFdx,eigs]=shootjac(x0,numperiods,p,s);
        % append eigenvalues
        EIGS=[EIGS;eigs'];
        % find new nullspace for next predictor step
        nv=null(dFdx);

        % make sure to get the null vector corresponding to continuation in the
        % positive direction of the continuation (state) variable the
        % sign of h will determine direction for continuation
        if nv(end)<0 % last element corresponds to cont. var.
            nv=-nv;
        end
    end
end
```

```
function [dFdx,EIGS]=shootjac(x,numperiods,p,s)
% shootjac.m

% Heavily modified from some of Harry's original code to separate
% functionality between jacobian call and function call...maybe put back
% together at some point

%%%%%%%%%%%%%%%%%%%%%%%%%%%%%%%%%%%%%%%%%%%%%%%%%%%%%%%%%%%%%%%%%%%%%%%%%%%%%%%
%% This stuff really shouldn't be here I don't think. It should be passed
%% as part of a problem definition structure.

FUNC=@diffeq; % declare the vector field function

tstart=0;
% make sure plenty of sim time to cover max. periodicity
tfinal=(s.maxper+1)*pi/x(s.freq);
x0=reshape(x,s.dim,1);
Px0=eye(s.dim);

options=odeset('RelTol',1e-8,'AbsTol',1e-8,'Events',@events);
%%%%%%%%%%%%%%%%%%%%%%%%%%%%%%%%%%%%%%%%%%%%%%%%%%%%%%%%%%%%%%%%%%%%%%%%%%%%%%%
% save calculations
dim2=s.dim^2;
jacbeg=s.dim+1;
jacend=s.dim+dim2;

numperind=0;
```

```
28
29 while tstart<tfinal
30     [t,y,te,ye,ie]=ode45(FUNC,[tstart tfinal],[x0;reshape(Px0',dim2,1)],options,p);
31     tstart=t(end);
32
33     x0=y(end,1:s.dim)';
34     dphidx=reshape(y(end,jacbeg:jacend),s.dim,s.dim)';
35     if ¬isempty(ie)
36         % PHASE event
37         if ie(end)==1
38
39             numperind=numperind+1;
40
41             dh=[0,0,0,-1,0,0,0]; % jacobian of the event function
42             x0(4)=x0(4)-2*pi; % mod. phase
43             % get vector field, post mapping
44             temp=FUNC(te(end),[x0;reshape(eye(s.dim),dim2,1)],p);
45             f=temp(1:s.dim); % isolate state vector field
46             gx=eye(s.dim); % jacobian of of event map
47             % project coord jacobian onto event surface
48             Px0=gx*(eye(s.dim)-f*dh/(dh*f))*dphidx;
49             % give a frendly bump to avoid false positive on restart
50             x0=x0+1e-12*f;
51
52             % Check for numperiods to shoot
53             if numperind==numperiods
54                 break
55             end
56
57         % IMPACT event
58         elseif ie(end)==2
59             display('contact')
60             dh=[-1,0,0,0,0,0,0];
61             x0(2)=-p.e*x0(2);
62             temp=FUNC(te(end),[x0;reshape(eye(s.dim),dim2,1)],p);
63             f=temp(1:s.dim);
64             gx=[1,0,0,0,0,0,0;
65                 0,-p.e,0,0,0,0,0;
66                 0,0,1,0,0,0,0;
67                 0,0,0,1,0,0,0;
68                 0,0,0,0,1,0,0;
69                 0,0,0,0,0,1,0
70                 0,0,0,0,0,0,1];
71             Px0=gx*(eye(s.dim)-f*dh/(dh*f))*dphidx;
72             x0=x0+1e-12*f;
73
74         % local MAX position (velocity goes (+) to (-)
75         elseif ie(end)==3
76             dh=[0,1,0,0,0,0,0];
77             temp=FUNC(te(end),[x0;reshape(eye(s.dim),dim2,1)],p);
78             f=temp(1:s.dim);
79             Px0=(eye(s.dim)-f*dh/(dh*f))*dphidx;
80             x0=x0+1e-12*f;
81
82         % local MIN postion (velocity goes (-) to (+)
83         elseif ie(end)==4
84             dh=[0,-1,0,0,0,0,0];
85             temp=FUNC(te(end),[x0;reshape(eye(s.dim),dim2,1)],p);
86             f=temp(1:s.dim);
87             Px0=(eye(s.dim)-f*dh/(dh*f))*dphidx;
88             x0=x0+1e-12*f;
89         else
90             error('shouldn''t be possible');
91         end
92     end
93 end
94
```

```
temp=Px0-eye(s.dim);
dFdx=[temp(1:s.coords,1:s.coords),temp(1:s.coords,s.contvar)];
EIGS=eig(Px0);
```

```
function DIFF=shootfun(x,numperiods,p,s)
% shootfun.m

% Heavily modified from some of Harry's original code to separate
% functionality between jacobian call and function call...maybe put back
% together at some point

%%%%%%%%%%%%%%%%%%%%%%%%%%%%%%%%%%%%%%%%%%%%%%%%%%%%%%%%%%%%%%%%%%%%%%%%%%%
%% This stuff really shouldn't be here I don't think. It should be passed
%% as part of a problem definition structure.

FUNC=@diffeq; % declare the vector field function

tstart=0;
% make sure plenty of sim time to cover max. periodicity
tfinal=(s.maxper+1)*pi/x(s.freq);
x0=reshape(x,s.dim,1);
Px0=eye(s.dim);

options=odeset('RelTol',1e-8,'AbsTol',1e-8,'Events',@events);
%%%%%%%%%%%%%%%%%%%%%%%%%%%%%%%%%%%%%%%%%%%%%%%%%%%%%%%%%%%%%%%%%%%%%%%%%%%
% save calculations
dim2=s.dim^2;
jacbeg=s.dim+1;
jacend=s.dim+dim2;

numperind=0;

while tstart<tfinal
    [t,y,te,ye,ie]=ode45(FUNC,[tstart tfinal],[x0;reshape(Px0',dim2,1)],options,p);
    tstart=t(end);

    x0=y(end,1:s.dim)';
    dphidx=reshape(y(end,jacbeg:jacend),s.dim,s.dim)';
    if ¬isempty(ie)
        % PHASE event
        if ie(end)==1

            numperind=numperind+1;

            dh=[0,0,0,-1,0,0,0]; % jacobian of the event function
            x0(4)=x0(4)-2*pi; % mod. phase
            % get vector field, post mapping
            temp=FUNC(te(end),[x0;reshape(eye(s.dim),dim2,1)],p);
            f=temp(1:s.dim); % isolate state vector field
            gx=eye(s.dim); % jacobian of of event map
            % project coord jacobian onto event surface
            Px0=gx*(eye(s.dim)-f*dh/(dh*f))*dphidx;
            % give a frendly bump to avoid false positive on restart
            x0=x0+1e-12*f;

            % Check for numperiods to shoot
            if numperind==numperiods
                break
            end

        % IMPACT event
        elseif ie(end)==2
            display('contact')
            dh=[-1,0,0,0,0,0,0];
```

```
            x0(2)=-p.e*x0(2);
            temp=FUNC(te(end),[x0;reshape(eye(s.dim),dim2,1)],p);
            f=temp(1:s.dim);
            gx=[1,0,0,0,0,0,0;
                0,-p.e,0,0,0,0,0;
                0,0,1,0,0,0,0;
                0,0,0,1,0,0,0;
                0,0,0,0,1,0,0;
                0,0,0,0,0,1,0
                0,0,0,0,0,0,1];
            Px0=gx*(eye(s.dim)-f*dh/(dh*f))*dphidx;
            x0=x0+1e-12*f;

        % local MAX position (velocity goes (+) to (-)
        elseif ie(end)==3
            dh=[0,1,0,0,0,0,0];
            temp=FUNC(te(end),[x0;reshape(eye(s.dim),dim2,1)],p);
            f=temp(1:s.dim);
            Px0=(eye(s.dim)-f*dh/(dh*f))*dphidx;
            x0=x0+1e-12*f;

        % local MIN postion (velocity goes (-) to (+)
        elseif ie(end)==4
            dh=[0,-1,0,0,0,0,0];
            temp=FUNC(te(end),[x0;reshape(eye(s.dim),dim2,1)],p);
            f=temp(1:s.dim);
            Px0=(eye(s.dim)-f*dh/(dh*f))*dphidx;
            x0=x0+1e-12*f;
        else
            error('shouldn''t be possible');
        end
    end
end

temp=x0-x;
DIFF=temp(1:s.coords);
```

```
function [x,n]=NewtonRaphson(shootfun,shootjac,x0,xs,nv,C,numperiods, p,s)
% NewtonRaphson.m

% shootfun and shootjac are function handles to the respective shooting
% routines

x=x0;
F=[shootfun(x,numperiods,p,s);nv'*C'*(x-xs)];
n=0;
res=norm(F);
while res>s.NRtol && n≤s.maxNRiter

    dFdx=[shootjac(x,numperiods,p,s);nv'];
    if cond(dFdx)<s.NRmaxcondnum
        x=x-C*inv(dFdx)*F;
    else
        warning('condition number of dFdx too large')
        n=s.maxNRiter+1; % return one larger iteration to tell invoking
                         % function that NR did not converge
        return
    end
    F=[shootfun(x,numperiods,p,s);nv'*C'*(x-xs)];
    n=n+1;
    res=norm(F);

end
```

Appendix D

Fabrication recipe for MEMS devices in Chapter 6

D.1 Materials list:

- SPR220 photoresist
- AP8000 adhesion promotor
- Δ77 SU-8 thermal cure epoxy (custom mix from Bruce Flachsbart)
- Double-sided polished 300 micron thick Si wafer <100> P/Boron, 100 mm dia, 1-5 Ohm-cm (wafer 1)
- Single-sided polished 500 micron thick Si wafer (wafer 2)
- Two chrome on soda-lime glass photolithography masks as shown below

D.2 Process:

D.2.1 Wafer 1 prep for bond

1. Degrease wafer (Acetone, IPA, DI water, IPA, N_2 dry)
2. Dehydration bake at 120°C for 2 min
3. Spincoat backside with AP8000
4. Bakeout 110°C, 1 min
5. Spincoat backside with SPR220 (recipe #3, 3000 rpm, 30 sec)
6. Softbake 110°C, 1min
7. Expose backside with mask 1, 20 sec
8. Develop using straight 327 developer, approx. 1 min

9. DI quench then N_2 blow dry
10. Inspect
11. Bake at 110°C for 2 min with heat shield
12. Etch in STS for 6 min. using recipe MANTRA2 (about 50 μm etch depth)
13. Strip PR in 1165 preheated to 120°C, approx. 15min, ultrasound for 5min
14. Degrease wafer
15. Spincoat topside with SPR220 (recipe #3, 3000 rpm, 30 sec)
16. Softbake 110°C, 1 min
17. Bottom side alignment with mask 2, expose 20 sec
18. Develop using straight 327
19. DI quench at least 1 min, then N_2 blow dry
20. Inspect and check features
21. Hardbake at 110°C for 2 min with heat shield
22. Sputter Al, 2 min 300W
23. Strip PR (liftoff) in 1165 in ultrasound

D.2.2 Wafer 2 preparation and assembly bond

1. Spin coat bottom SSP wafer with 3 micron SU-8
2. Vacuum anneal at 60°C for 2 hours
3. Place bottom wafer in bonder and stack top wafer making sure to align the flats perfectly the first time. Bond is almost instant.
4. Place coverglass on stack, close bonder and run bonding program NOTETK put bonding program parameters in here

D.2.3 Final photolithography and thru-etch

1. Spincoat topside with AP8000
2. Bakeout 110°C, 1 min
3. Spincoat topside with SPR220 (recipe #3, 3000 rpm, 30 sec)
4. Softbake 110°C, 1 min
5. Top side alignment with mask 2, expose 20 sec
6. Develop using straight 327
7. DI quench at least 1 min, then N_2 blow dry
8. Inspect and check features
9. Hardbake at 110°C for 2 min with heat shield
10. Thru etch wafer 1 using recipe MANTRA2 in STS, 38 min
11. Strip PR in 1165 preheated to 120°C, approx. 15 min, ultrasound for 5 min
12. Transfer to acetone bath and rock to remove air bubbles
13. Transfer to methanol bath and rock to remove air bubbles
14. Remove from methanol and air dry
15. Conformal sputter aluminum, (20 min, 300 watts)

D.3 Mask drawings

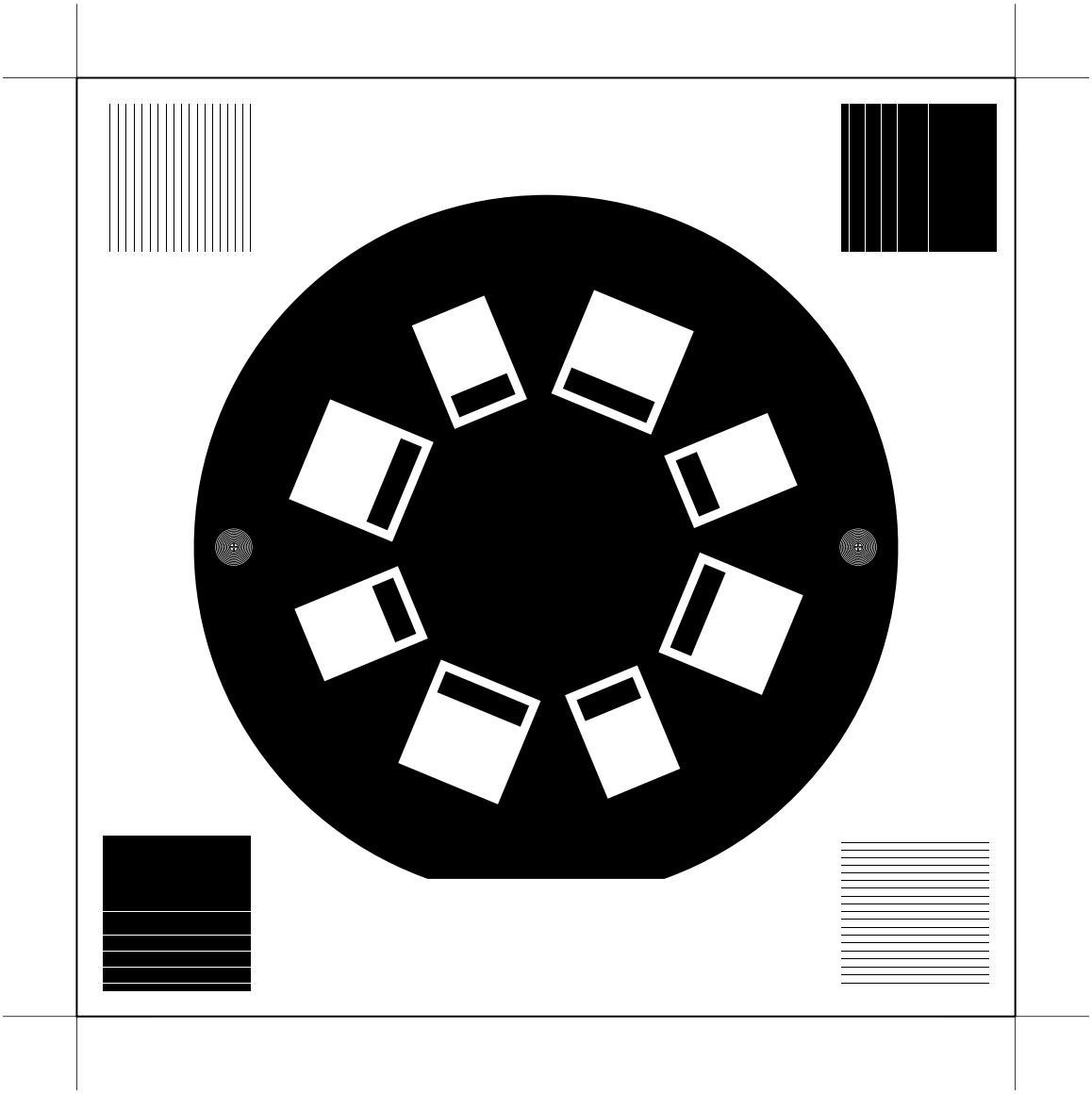

Figure D.1: Drawing of mask 1. See text in Chapter 6 for a detailed description of the devices.

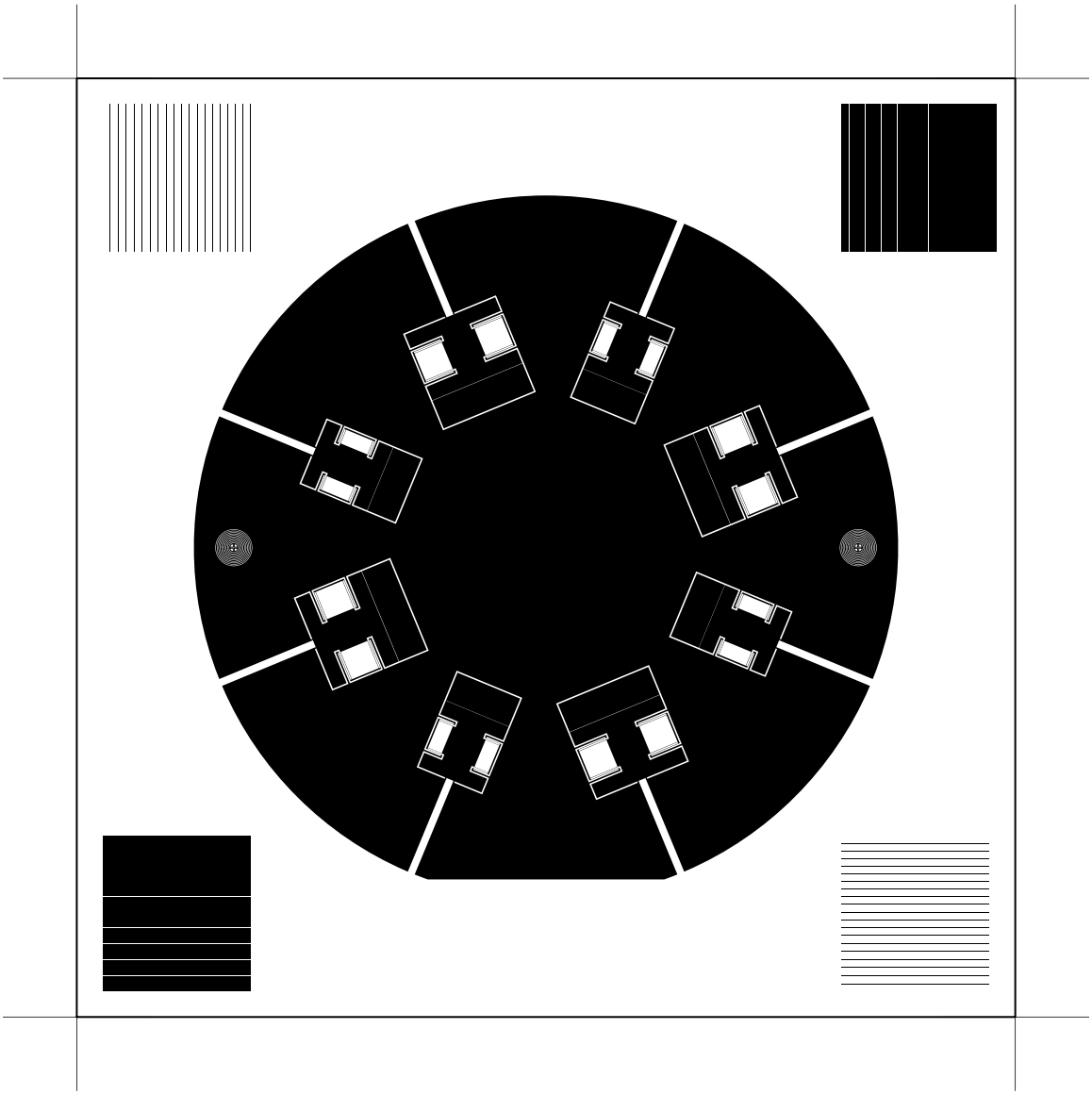

Figure D.2: Drawing of mask 2. See text in Chapter 6 for a detailed description of the devices.

References

[1] E.M. Abdel-Rahman and A.H. Nayfeh. Secondary resonances of electrically actuated resonant microsensors. *Journal of Micromechanics and Microengineering*, 13:491, 2003.

[2] M.S. Allen, J.E. Massad, R.V. Field Jr., and C.W. Dyck. Input and design optimization under uncertainty to minimize the impact velocity of an electrostatically actuated mems switch. *Journal of Vibration and Acoustics*, 130:021009, 2008.

[3] F. Angulo, M. Di Bernardo, E. Fossas, and G. Olivar. Feedback control of limit cycles: a switching control strategy based on nonsmooth bifurcation theory. *IEEE Transactions on Circuits and Systems-I: Regular Papers*, 52(2), 2005.

[4] R.C. Batra, M. Porfiri, and D. Spinello. Capacitance estimate for electrostatically actuated narrow microbeams. *Micro & Nano Letters, IET*, 1(2):71–73, 2006.

[5] R.C. Batra, M. Porfiri, and D. Spinello. Electromechanical model of electrically actuated narrow microbeams. *Microelectromechanical Systems, Journal of*, 15(5):1175–1189, 2006.

[6] R.C. Batra, M. Porfiri, and D. Spinello. Vibrations of narrow microbeams predeformed by an electric field. *Journal of Sound and Vibration*, 309(3-5):600–612, 2008.

[7] S.R. Bishop, M.G. Thompson, and S. Foale. Prediction of period-1 impacts in a driven beam. *Proceedings: Mathematical, Physical and Engineering Sciences*, 452(1954):2579–2592, 1996.

[8] D.M. Cannon Jr, B.R. Flachsbart, M.A. Shannon, J.V. Sweedler, and P.W. Bohn. Fabrication of single nanofluidic channels in poly (methylmethacrylate) films via focused-ion beam milling for use as molecular gates. *Applied Physics Letters*, 85:1241, 2004.

[9] F.M. Castro. Mechanical switches snap back. *Machine Design*, 63(19):56 – 58, 60–66, 1991.

[10] P.C.P. Chao, C.W. Chiu, and C.Y. Tsai. A novel method to predict the pull-in voltage in a closed form for micro-plates actuated by a distributed electrostatic force. *Journal of Micromechanics and Microengineering*, 16:986, 2006.

[11] S. Chatzandroulis, S. Koliopoulou, D. Goustouridis, and D. Tsoukalas. Capacitive pressure sensors and switches fabricated using strain compensated SiGeB. *Microelectronic Engineering*, 83(4-9):1209–1211, 2006.

[12] W. Chin, E. Ott, H.E. Nusse, and C. Grebogi. Grazing bifurcations in impact oscillators. *Physical Review E*, 50(6):4427–4444, 1994.

[13] H. Dankowicz and J. Jerrelind. Control of near-grazing dynamics in impact oscillators. *Proceedings of the Royal Society A: Mathematical, Physical and Engineering Science*, 461(2063):3365, 2005.

[14] H. Dankowicz and F. Svahn. On the stabilizability of near-grazing dynamics in impact oscillators. *International Journal of Robust and Nonlinear Control*, 17(15):1405–1429, 2007.

[15] H. Dankowicz and X. Zhao. Local analysis of co-dimension-one and co-dimension-two grazing bifurcations in impact microactuators. *Physica D: Nonlinear Phenomena*, 202(3-4):238–257, 2005.

[16] H. Dankowicz, X. Zhao, and S. Misra. Near-grazing dynamics in tapping-mode atomic-force microscopy. *International Journal of Non-Linear Mechanics*, 42(4):697–709, 2007.

[17] E.J. Doedel, H.B. Keller, and J.P. Kernévez. Numerical analysis and control of bifurcation problems:(II) Bifurcation in infinite dimensions. *International Journal of Bifurcation and Chaos*, 1(4):745–772, 1991.

[18] J. Eriksson. Experimental and numerical studies of nonsmooth mechanical systems: applications of dimension estimation. Master's thesis, Royal Institute of Technology, Stockholm, Sweden, 2005. TRITA-MEK 2005:08, ISSN 0348-467X.

[19] W. Fang and J.A. Wickert. Response of a periodically driven impact oscillator. *Journal of Sound and Vibration*, 170(3):397–410, 1994.

[20] B.R. Flachsbart, K. Wong, J.M. Iannacone, E.N. Abante, R.L. Vlach, P.A. Rauchfuss, P.W. Bohn, J.V. Sweedler, and M.A. Shannon. Design and fabrication of a multilayered polymer microfluidic chip with nanofluidic interconnects via adhesive contact printing. *Lab on a Chip*, 6(5):667–674, 2006.

[21] S. Foale and S.R. Bishop. Bifurcations in impact oscillations. *Nonlinear dynamics*, 6(3):285–299, 1994.

[22] J. Fraden. *Handbook of modern sensors: physics, designs, and applications*. springer Verlag, 2004.

[23] M.H. Fredriksson, D. Borglund, and A.B. Nordmark. Experiments on the onset of impacting motion using a pipe conveying fluid. *Nonlinear Dynamics*, 19(3):261–271, 1999.

[24] M.H. Fredriksson and A.B. Nordmark. Bifurcations caused by grazing incidence in many degrees of freedom impact oscillators. *Proceedings: Mathematical, Physical and Engineering Sciences*, 453(1961):1261–1276, 1997.

[25] H. Fujita, D. Kobayashi, M. Mita, and S. Tensaka. Micro-actuator and method making the same. Patent, 08 2006. US 7090781.

[26] I. Garshelis, M. Devices, and I. Pittsfield. A current threshold sensor. *IEEE Transactions on Magnetics*, 15(6):1809–1811, 1979.

[27] J. Grohs, M. Müller, A. Schmidt, A. Uhrig, C. Klingshirn, and H. Bartelt. On the possible use of photo thermal optical bistability as a temperature sensor. *Optics Communications*, 78(1):77–80, 1990.

[28] P. Horowitz and W. Hill. *The art of electronics*. University Press, 1989.

[29] J.D. Jansen. Non-linear rotor dynamics as applied to oilwell drillstring vibrations. *Journal of Sound and Vibration*, 147(1):115–135, 1991.

[30] W. Kang, P. Thota, B. Wilcox, and H. Dankowicz. Bifurcation analysis of a microactuator using a new toolbox for continuation of hybrid system trajectories. *Journal of Computational and Nonlinear Dynamics*, 4:011009, 2009.

[31] K. Karagiannis and F. Pfeiffer. Theoretical and experimental investigations of gear-rattling. *Nonlinear Dynamics*, 2(5):367–387, 1991.

[32] R.R. Katta, A.A. Polycarpou, J.V. Hanchi, and R.M. Crone. High Velocity Oblique Impact and Coefficient of Restitution for Head Disk Interface Operational Shock. *Journal of Tribology*, 131:021903, 2009.

[33] G. Kerschen, Y.S. Lee, A.F. Vakakis, D.M. McFarland, and L.A. Bergman. Irreversible passive energy transfer in coupled oscillators with essential nonlinearity. *SIAM Journal on Applied Mathematics*, 66(2):648–679, 2006.

[34] P.C. Krause and O. Wasynczuk. *Electromechanical motion devices*. McGraw-Hill, 1989.

[35] S. Krylov, B.R. Ilic, D. Schreiber, S. Seretensky, and H. Craighead. The pull-in behavior of electrostatically actuated bistable microstructures. *Journal of Micromechanics and Microengineering*, 18:055026, 2008.

[36] S. Krylov and R. Maimon. Pull-in dynamics of an elastic beam actuated by continuously distributed electrostatic force. *Journal of vibration and acoustics*, 126:332, 2004.

[37] Y. A. Kuznetsov. *Elements of applied bifurcation theory*. Springer New York, 1998.

[38] W. Lacarbonara and H. Yabuno. Refined models of elastic beams undergoing large in-plane motions: Theory and experiment. *International Journal of Solids and Structures*, 43(17):5066–5084, 2006.

[39] R.I. Leine, D.H. Van Campen, and W.J.G. Keultjes. Stick-slip whirl interaction in drillstring dynamics. *Journal of Vibration and Acoustics*, 124:209, 2002.

[40] Y. Li and N. Wu. A Low-Cost CMOS Programmable Temperature Switch. *Sensors*, 8(5):3150–3164, 2008.

[41] Y. Lin, W.C. Li, Z. Ren, and C.T.C. Nguyen. The micromechanical resonant switch. In *Resoswitch), Tech. Digest, 2008 Solid-State Sensor, Actuator, and Microsystems Workshop, Hilton Head, South Carolina*, 2008.

[42] C. Liu. *Foundations of MEMS*. Pearson/Prentice Hall, 2006.

[43] X.H. Long, G. Lin, and B. Balachandran. Grazing bifurcations in an elastic structure excited by harmonic impactor motions. *Physica D: Nonlinear Phenomena*, 237(8):1129–1138, 2008.

[44] A.C.J. Luo and B.C. Gegg. On the mechanism of stick and nonstick, periodic motions in a periodically forced, linear oscillator with dry friction. *Journal of Vibration and Acoustics*, 128:97, 2006.

[45] M.J. Madou. *Fundamentals of microfabrication: the science of miniaturization*. CRC, 2002.

[46] B. Mi, D.A. Smith, H. Kahn, F.L. Merat, A.H. Heuer, and S.M. Phillips. Static and electrically actuated shaped MEMS mirrors. *Journal of Microelectromechanical Systems*, 14(1):29–36, 2005.

[47] S. Misra, H. Dankowicz, and M.R. Paul. Degenerate discontinuity-induced bifurcations in tapping-mode atomic-force microscopy. *Physica D: Nonlinear Phenomena*, 239(1-2):33–43, 2010.

[48] M. Mita, M. Arai, S. Tensaka, D. Kobayashi, and H. Fujita. A micromachined impact microactuator driven by electrostatic force. *Microelectromechanical Systems, Journal of*, 12(1):37–41, 2003.

[49] T. Mohr and F.H. Uhlmann. Detecting thresholds by means of jump-phenomena. In *The 7th IEEE International Conference on Electronics, Circuits and Systems, 2000. ICECS 2000*, pages 772–775, 2000.

[50] J. Molenaar, J.G. de Weger, and W. Van de Water. Mappings of grazing-impact oscillators. *Nonlinearity*, 14:301–321, 2001.

[51] R. Movshovich, B. Yurke, A.D. Smith, and A.H. Silver. Subharmonic pumping of a Josephson-parametric amplifier and the pitchfork instability. *Physical review letters*, 67(11):1411–1414, 1991.

[52] A.B. Nordmark. Non-periodic motion caused by grazing incidence in an impact oscillator. *Journal of Sound and Vibration*, 145(2):279–297, 1991.

[53] A.B. Nordmark. Effects due to low velocity impact in mechanical oscillators. *International Journal of Bifurcation and Chaos*, 2(3):597–605, 1992.

[54] A.B. Nordmark. Universal limit mapping in grazing bifurcations. *Physical review E*, 55(1):266–270, 1997.

[55] A.B. Nordmark. Existence of periodic orbits in grazing bifurcations of impacting mechanical oscillators. *Nonlinearity*, 14:1517, 2001.

[56] J.J. Paques. Limit switches: Selection for safety. *ISA Transactions*, 33(1):99–103, 1994.

[57] P.T. Piiroinen, L.N. Virgin, and A.R. Champneys. Chaos and period-adding; experimental and numerical verification of the grazing bifurcation. *Journal of Nonlinear Science*, 14(4):383–404, 2004.

[58] J. Qiu and Z.C. Feng. Parameter dependence of the impact dynamics of thin plates. *Computers & Structures*, 75(5):491–506, 2000.

[59] S.W. Shaw. Forced vibrations of a beam with one-sided amplitude constraint: theory and experiment. *Journal of Sound and Vibration*, 99(2):199–212, 1985.

[60] I. Siddiqi, R. Vijay, F. Pierre, C.M. Wilson, M. Metcalfe, C. Rigetti, L. Frunzio, and M.H. Devoret. RF-driven Josephson bifurcation amplifier for quantum measurement. *Physical review letters*, 93(20):207002, 2004.

[61] A. Stensson and A.B. Nordmark. Experimental investigation of some consequences of low velocity impacts in the chaotic dynamics of a mechanical system. *Philosophical Transactions: Physical Sciences and Engineering*, 347(1683):439–448, 1994.

[62] W. J. Strong. *Impact Mechanics*. Cambridge University Press, 2000.

[63] P. Thota. *Analytical and Computational Tools for the Study of Grazing Bifurcations of Periodic Orbits and Invariant Tori*. PhD thesis, Virginia Polytechnic Institute and State University, Blacksburg, VA, 2007.

[64] P. Thota and H. Dankowicz. Continuous and discontinuous grazing bifurcations in impacting oscillators. *Physica D: Nonlinear Phenomena*, 214(2):187–197, 2006.

[65] P. Thota and H. Dankowicz. TC-HAT ($\widehat{\text{TC}}$): A Novel Toolbox for the Continuation of Periodic Trajectories in Hybrid Dynamical Systems. *SIAM Journal on Applied Dynamical Systems*, 7:1283, 2008.

[66] P. Thota, X. Zhao, and H. Dankowicz. Co-dimension-two grazing bifurcations in single-degree-of-freedom impact oscillators. *Journal of Computational and Nonlinear Dynamics*, 1:328, 2006.

[67] K.L. Turner, R. Baskaran, and W. Zhang. Using nonlinear dynamics for performance enhancement in resonant micro and nano-scale devices. In *42nd IEEE Conference on Decision and Control, 2003. Proceedings*, volume 3, 2003.

[68] E.L.B. Van De Vorst, M.F. Heertjes, D.H. Van Campen, A. De Kraker, and R.H.B. Fey. Experimental and numerical analysis of the steady state behaviour of a beam system with impact. *Journal of Sound and Vibration*, 212(2):321–336, 1998.

[69] E.L.B. Van de Vorst, D.H. Van Campen, A. De Kraker, and R.H.B. Fey. Periodic solutions of a multi-DOF beam system with impact. *Journal of Sound and Vibration*, 192(5):913–925, 1996.

[70] K. Wiesenfeld and B. McNamara. Period-doubling systems as small-signal amplifiers. *Physical review letters*, 55(1):13–16, 1985.

[71] K. Wiesenfeld and B. McNamara. Small-signal amplification in bifurcating dynamical systems. *Physical Review A*, 33(1):629–642, 1986.

[72] B. Wilcox and H. Dankowicz. Design of Limit-Switch Sensors Based on Discontinuity-Induced Nonlinearities. In *Proc. of the ASME 2009 Int. Des. and Eng. Tech. Conf., San Diego, California, USA*. ASME, 2009.

[73] B. Wilcox and H. Dankowicz. Limit-switch sensor functionality based on discontinuity-induced nonlinearities. *Journal of Computational and Nonlinear Dynamics*, 6:031004, 2011.

[74] B. Wilcox and H. Dankowicz. An experimental testbed for investigating nonsmooth bifurcations in an electromechanical system. *Journal of Vibration and Control*, in press.

[75] B. Wilcox, H. Dankowicz, and W. Lacarbonara. Response of Electrostatically Actuated Flexible MEMS Structures to the Onset of Low-velocity Contact. In *Proc. of the ASME 2009 Int. Des. and Eng. Tech. Conf., San Diego, California, USA*. ASME, 2009.

[76] B. Wilcox, F. Svahn, H. Dankowicz, and J. Jerrelind. Transient growth rates of near-grazing impact velocities: Theory and experiments. *Journal of Sound and Vibration*, 325(4-5):950–958, 2009.

[77] M.I. Younis, F. Alsaleem, and D. Jordy. The response of clamped-clamped microbeams under mechanical shock. *International Journal of Non-Linear Mechanics*, 42(4):643–657, 2007.

[78] W. Zhang, R. Baskaran, and K.L. Turner. Effect of cubic nonlinearity on auto-parametrically amplified resonant MEMS mass sensor. *Sensors and Actuators A: Physical*, 102(1-2):139–150, 2002.

[79] W. Zhang and K.L. Turner. Application of parametric resonance amplification in a single-crystal silicon micro-oscillator based mass sensor. *Sensors and Actuators A: Physical*, 122(1):23–30, 2005.

[80] X. Zhao and H. Dankowicz. Characterization of intermittent contact in tapping-mode atomic force microscopy. *Journal of Computational and Nonlinear Dynamics*, 1:109, 2006.

[81] X. Zhao and H. Dankowicz. Unfolding degenerate grazing dynamics in impact actuators. *Nonlinearity*, 19:399, 2006.

[82] X. Zhao, H. Dankowicz, C.K. Reddy, and A.H. Nayfeh. Modeling and simulation methodology for impact microactuators. *Journal of Micromechanics and Microengineering*, 14:775, 2004.

[83] X. Zhao, CK Reddy, and AH Nayfeh. Nonlinear dynamics of an electrically driven impact microactuator. *Nonlinear Dynamics*, 40(3):227–239, 2005.